SCANNING PROBE INVESTIGATIONS ON GRAPHENE

A DISSERTATION SUBMITTED TO THE UNIVERSITY OF MANCHESTER
FOR THE DEGREE OF DOCTOR OF PHILOSOPHY
IN THE FACULTY OF ENGINEERING AND PHYSICAL SCIENCES

2010

By
Soeren Neubeck
School of Physics and Astronomy

Contents

List of Figures

Abstract

In this thesis, scanning probe microscopy experiments on graphene and chemically modified graphene crystals are discussed. Since its discovery in 2004, graphene has not only impressed researchers and industry because it is a crystal that is only one atom thick, but also because of its electronic transport properties. However, a major challenge remaining is the task to introduce an energy gap in graphene. One way to open an energy gap in pristine graphene is its confinement to nanometre sizes. To this end, methods were developed to fabricate such nanostructures out of graphene. Here, the atomic force microscope (AFM) based technique of local anodic oxidation was applied to selectively oxidise graphene. Using this technique, graphene nanostructures as small as 20 nm have been fabricated. A graphene quantum dot (QD) created with this technique was measured at low temperatures. It showed quantum Coulomb blockade behaviour, with an energy gap of $\approx$10 meV. Furthermore, the transport behaviour of these nanostructures was also investigated under ambient conditions. Scanning gate microscopy measurements carried out on a graphene quantum point contact (QPC) demonstrated the possibility to locally influence the charge carrier concentration in the QPC, and thus alter the resistance of the device. These experiments additionally prove the usefulness of local anodic oxidation to create graphene nanostructures. Equally tempting as opening a gap in graphene and studying the resulting transport properties is the prospect of studying the influence of the edges terminating a graphene crystal on its transport properties. To that end, reliable methods for obtaining the crystallographic orientation of a given edge are needed. While most techniques require either elaborated sample fabrication or modelling, it is shown here how atomically resolved scanning tunnelling microscopy (STM) imaging together with Raman spectroscopy can be used to determine the crystallographic direction of graphene edges without doubt. An alternative way of creating an energy gap in graphene is its modification with atomic hydrogen. Atomic force

microscopy was first used to measure the topography of hydrogenated graphene crystals. It is further shown, how the amount of adsorbed hydrogen could be decreased using AFM. The changes induced in the hydrogenated graphene samples in this way have been further corroborated by Raman spectroscopy and low temperature transport experiments, establishing AFM as a method to engineer the resistance of hydrogenated graphene.

Declaration

No portion of the work referred to in this dissertation has been submitted in support of an application for another degree or qualification of this or any other university or other institute of learning.

Copyright

Acknowledgements

First of all I wish to thank my supervisor, Prof.Andre Geim, for giving me the opportunity to carry out my PhD-research in his research group. His guidance, constant motivation and physical insight were an essential part stimulating my work.

My advisor, Dr.Irina Grigorieva, I would like to thank for her encouragement and her openness concerning discussions related to my work.

I want to express my gratitude towards Dr.Kostya Novoselov. His constant guidance and help in the lab and his cooperativeness made working with him an enjoyable experience.

I would like to thank all members, past and present, of our research group for the nice working atmosphere and their help and suggestions. I want to thank especially Dr.Rui Yang, Dr.Svetlana Anisimova and Ibtsam Riaz for supplying me with most of the graphene flakes studied in this work.

My sincere thanks go to Mr.Mark Sellers and Mr.Stan Gillot for expert technical work. I would like to thank the members of the Electronics workshop at the Schuster Laboratory, and the members of the central mechanical workshop for fabricating the cage used for suspending our scanning probe microscope.

For performing the low temperature transport measurements presented in Chapter 4, I would like to thank Dr.Leonid Ponomarenko. I am indebted to Dr.You Yumeng for carrying out the Raman measurements presented in Chapter 6. I would like to thank Dr.Sasha Mayorov for measuring the low temperature transport properties of scratched hydrogenated graphene, as presented in Chapter 7.

Rebecca Shaw and Katy Denniff from the postgraduate office I would like to thank for their help with all formal issues related to my PhD studies.

Further, I want to thank Dr.Roman Gorbachev, Dr.Sasha Mayorov, Dr.Leonid

Chapter 1

Introduction

The isolation of graphene [1,2] was the first-ever observation of a two-dimensional crystal by mankind. Graphene is a macroscopically sized, but only one atom thick layer of carbon atoms periodically arranged in a honeycomb lattice. At a first glance, this discovery seemed to contradict established physical laws, which says that two-dimensional materials should not exist [3]. This contradiction could be solved by regarding the fact that only the *growth* of free-standing two-dimensional materials is forbidden. In their seminal discovery, Geim and Novoselov extracted graphene by micromechanically cleaving a graphite crystal, which consists of millions of graphene layers stacked upon each other, down to a single layer and placing it on top of an oxidized silicon wafer.

In their first investigations of this material, they studied the behaviour of its charge carriers. They found an intriguing property, namely that both electrons and holes in graphene follow a linear energy dispersion [4] with a band gap of zero. Consequently, in terms of electronic transport properties, graphene's charge carriers constitute a two-dimensional gas of so called massless Dirac fermions. This finding connected the physics of relativistic particles with solid state structures. Subsequently, further details about charge carrier transport in graphene were elucidated [3]. Not only ballistic transport [5] of the charge carriers in graphene was found, but also a mobility (reaching up to millions by August 2010) of both electrons and holes that was practically independent of temperature and charge carrier concentration. The latter facts elevate graphene into a position as a most promising contender for future microelectronics applications. However, the fact remains that pristine graphene is found to be always conductive, even in the limit

of virtually zero charge carrier concentration, whereas transistor applications require the presence of a non-conducting state.

But the significance and challenges of graphene are not only limited towards its electronic properties. Its mechanical and optical properties are at least equally remarkable. Graphene exhibits a breaking strength of $\sim$40 N/m [6], shows record values for room temperature thermal conductivity [7] and Young's modulus [6] and can sustain strain of up to 20% [6] [8]. The fact that graphene is only one atom thick makes it the ultimate support for transmission electron microscopy (TEM) studies [5]. Also in the field of optoelectronics, graphene could have major impact as e.g. a photodetector [9] or as a transparent conductor [10].

Looking from a materials point of view, graphene proves to be unique, too. Being a strictly two-dimensional material, it is an ultimate incarnation of the surface [5]. It can be considered as an atomic scaffold, which can serve as a starting point in synthesizing new two-dimensional crystals. These stoichiometric graphene derivatives are believed to show new electrical, optical and chemical properties. They might also offer a way to control the electronic structure of the pristine graphene crystal, which might have its application in electronics. A first proof was already presented [11], showing how the bonding of atomic hydrogen to the graphene lattice leads to reversibly transforming the zero-gap semiconductor graphene into a two-dimensional hydrocarbon, exhibiting a metal-to-insulator transition.

Still, despite the achievements just mentioned, plenty of open questions remain. What is the experimentally achievable upper limit for the mobility of graphene's charge carriers? What happens at the Dirac-point, i.e. the energy where electron dispersion and hole dispersion touch? Can one efficiently control the electronic structure of graphene? While in the beginning of graphene research the investigations of global properties were dominating, soon thereafter the need for complementing local investigations, ideally down to the single atom level, became apparent. Local investigations of graphene's properties would allow allow for a deeper understanding of the physics and chemistry governing graphene. To be more precise, one question where the local nature of graphene becomes important is what happens when graphene becomes confined to nanometre sizes?

Moreover, could one confine graphene to these sizes while still maintaining control of the termination of the resulting nanostructure? Another important task would be the atomically resolved determination of the crystallographic orientation of the edges terminating graphene. These edges are predicted to strongly influence both the chemical and physical behavior of the graphene crystals, and thus identifying their nature is of general importance. Last but not least, starting from an already macroscopically chemically modified graphene crystal, the question arises what its topographic surface structure looks like when compared to pristine graphene.

Experimental tools ideally suited for real-space investigations with a resolution down to a single atom are scanning probe microscopes (SPM). Scanning probe microscopy allows three-dimensional real-space images of the electronic and topographic properties of the sample surface to be obtained. This research field was started in 1982, with the invention of scanning tunnelling microscopy (STM) by Binnig and Rohrer [12]. STM is limited to the investigations of conductive sample surfaces alone. To overcome this limitation, Binnig invented the atomic force microscope (AFM) in 1986 [13]. Since its first demonstration, scanning probe microscopy has become an essential tool for experiments on the nano- and atomic scale, including atomically precise determination of the surface topography and chemical modification of the sample surface down to the single atom level [14].

In this thesis, AFM- and STM-experiments are presented, which were aimed at answering some of the questions outlined above. The thesis is organized as follows: in Chapter 2, I will present the fundamentals of graphene's bandstructure, AFM and STM. Furthermore, I will discuss AFM images and Raman spectroscopy data that serve as a reference for graphene. The main conclusions from these two experiments are used throughout the thesis. In Chapter 3, the SPM-based technique of local anodic oxidation and its application to fabricate graphene nanostructures are discussed. Chapter 4 starts with an introduction to the basics of charge carrier transport through quantum dots and finally presents and discusses the experimental results obtained for graphene quantum dots created by local anodic oxidation. In Chapter 5, scanning gate microscopy (SGM) data are discussed, which further demonstrate the success of SPM-based local anodic

oxidation to confine graphene to nanometre-sizes, as well as showing how to locally modify the conductance in graphene nanostructures. In Chapter 6, STM and Raman spectroscopy experiments are presented, which ultimately allow us to determine the crystallographic orientation of edges terminating a graphene crystal. Chapter 7 finally presents experiments on engineering the resistance in hydrogenated graphene. It is shown, how AFM can be used to transform hydrogenated graphene back towards pristine graphene. In the last chapter of this thesis, I will give a summary of what has been achieved in this thesis and what still needs to be understood. I will also outline directions of future research based on the findings presented in this thesis.

Chapter 2

Fundamentals

2.1   Introduction to Graphene

Graphene is the name given to a single layer consisting of three-fold coordinated carbon atoms. Graphene can be regarded as the fundamental building-block of hexagonal α-graphite. The crystal structure of hexagonal α-graphite is shown in Fig. 2.1. Within each graphene layer, every carbon atom forms three strongly localized σ-bonds with its neighbouring atoms. This leads to a honeycomb-lattice, as shown in Fig. 2.1. By definition, a single isolated graphene layer would constitute a two-dimensional crystal, since it would be only one-atom thick but extended laterally. In the pioneering work of K.S.Novoselov et al. [1, 2], it was demonstrated for the first time, that graphene and other two-dimensional crystals can be isolated and investigated. Since then, strong efforts of both experimental and theoretical physical research focussed on graphene, due to its fascinating inherent physical properties [3].

Probably one of the most interesting properties of graphene are its electrical transport properties. Graphene is a zero-gap semiconductor [3]. Novoselov et al. have shown, that it is possible to tune the charge carrier concentration n in graphene of both electrons and holes up to $n\sim10^{13}$ cm^{-2} by applying an external electric field [1]. Additionally, even at such high carrier concentrations, the mobilities μ of the charge carriers have been found to be extremely high, on the order of $\mu = 15,000$cm^2 V^{-1}s^{-1}. This value was found to be almost independent of temperature [4], being limited only by scattering on fixed impurities. Because of this, graphene might offer the possibility of fabricating submicron-size electronic devices showing ballistic transport at room temperature [3].
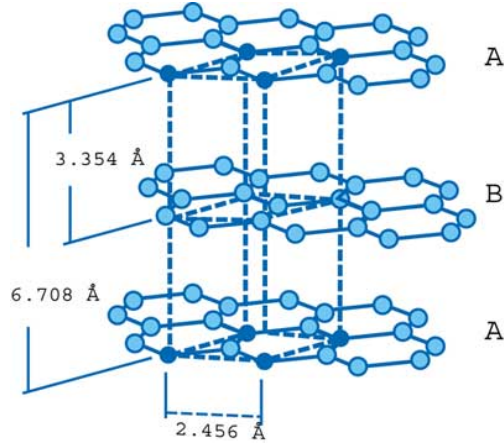
Figure 2.1: Crystal structure of hexagonal α-graphite. The lattice constant within each layer is 2.46 Å. The lattice constant perpendicular to the layers is 6.70 Å. Each layer represents a single layer graphene sheet. (*Image taken from http://www.electronics-cooling.com.*)

2.1.1 Graphene band structure

In order to obtain a detailed understanding of graphene's intriguing transport properties, we have to calculate its bandstructure. The following discussion of the graphene band structure calculation follows closely Ref. [15]. A more detailed derivation, but which contains exactly the same steps as in [15], can be found in [16]. The honeycomb crystal structure of a single graphene sheet is shown on the left in Fig. 2.2 In the honeycomb arrangment shown in (a), each Carbon atom contributes three of its four valence electrons to occupy planar sp^2-hybridized orbitals, leading to the formation of in-plane σ-bonds with its three nearest neighbour atoms. The honeycomb atomic lattice formed is not a Bravais lattice, but consists of two interpenetrating triangular Bravais sublattices, as indicated by dashed red and black triangles in (c). The unit cell of the honeycomb lattice hence contains two inequivalent sublattices containing either the carbon atoms labelled A (open circles) or B (solid dots) in Fig. 2.2(a) and (c). The unit cell of the honeycomb lattice is a rhomboid with the unit vectors:

$$\mathbf{a_1} = \sqrt{3}a\mathbf{e_x} \qquad and \qquad \mathbf{a_2} = \frac{\sqrt{3}}{2}a\mathbf{e_x} + \frac{3}{2}a\mathbf{e_y} \qquad (2.1)$$
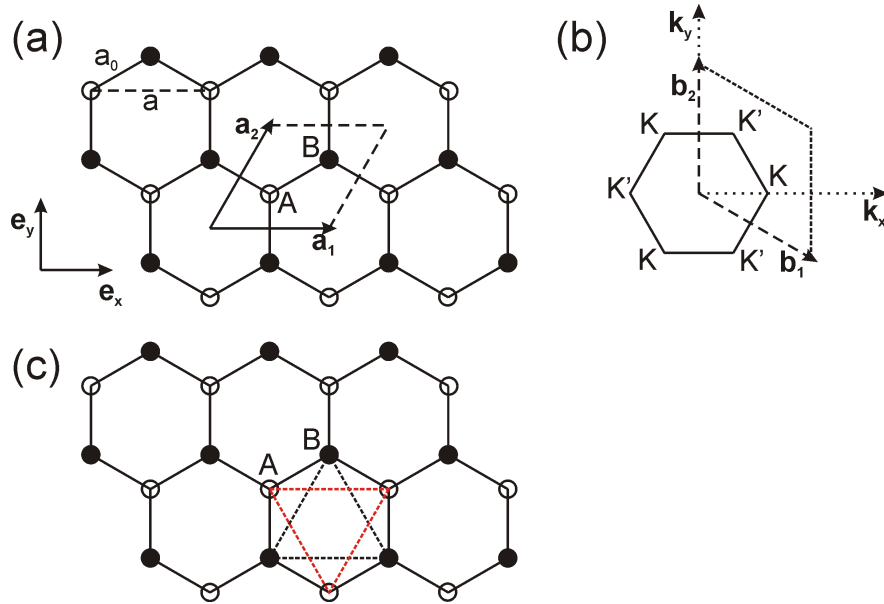
Figure 2.2: (a): Honeycomb atomic lattice structure of graphene, consisting of two interpenetrating triangular lattices, formed by the two lattices A and B, with lattice unit vectors $\mathbf{a}_1$ and $\mathbf{a}_2$. (b): The corresponding first Brillouin zone, which is a hexagon. The unit vectors in reciprocal space are $\mathbf{b}_1$ and $\mathbf{b}_2$. The points K and K$'$ denote the corners of the first Brillouin zone. (c) Illustration of the two inequivalent, interpenetrating triangular lattices (dashed lines), where the sublattice formed from atoms on A positions of the honeycomb lattice is red and the one formed by atoms sitting on B positions is black.

where a=1.42 Å is the interatomic distance. The interatomic distance is related to the lattice constant a_0 through $a_0 = \sqrt{3}a$.

The reciprocal lattice is again a triangular lattice, spanned by the reciprocal lattice vectors $\mathbf{b}_1$ and $\mathbf{b}_2$, as shown in Fig. 2.2(b):

$$\mathbf{b_1} = \frac{2\pi}{\sqrt{3}a}\left(\mathbf{e_x} - \frac{1}{\sqrt{3}}\mathbf{e_y}\right) \qquad and \qquad \mathbf{b_2} = \frac{4\pi}{3a}\mathbf{e_y}. \qquad (2.2)$$

The first Brillouin zone is a hexagon. Only two of the six corners of the Brillouin zone are inequivalent, since the others can be obtained from a primitive translation of the form $n\mathbf{b_1} + m\mathbf{b_2}$, where m, n are integers. The two inequivalent corners are labelled K and K$'$.

To calculate the energy band diagram, one commonly solves the time independent Schrödinger equation for one electron of the crystal lattice in the effective periodic potential of all the other electrons and the cores of the lattice. Because of the translational symmetry of the lattice, any of the possible wavefunctions for

the electron of the lattice should satisfy Bloch's theorem

$$T_{\mathbf{a_i}}\Psi = e^{i\mathbf{k}\mathbf{a_i}}\Psi, \qquad (i = 1, 2), \tag{2.3}$$

where $T_{\mathbf{a_i}}$ is a translational operation along the lattice vector $\mathbf{a_i}$, and $\mathbf{k}$ is the wavevector [16].

The corresponding wavefunctions satisfying Bloch's theorem (Eq. 2.3) are called Bloch functions. Such a Bloch function can be constructed to be based on an atomic orbital in the unit cell (or atom) [16]. Because the honeycomb lattice of graphene consists of two inequivalent triangular lattices, one has to consider two wavefunctions. One for an electron on the sublattice formed by atoms labelled A, and one for an electron on the sublattice formed by atoms labelled B. The Bloch functions for the two inequivalent atomic sites A and B can be expressed as:

$$\Phi_A(\vec{k}, \vec{r}) = \frac{1}{\sqrt{N}}\sum_{\vec{R_A}}^{N} exp(i\vec{k}\vec{R_A})\phi_A(\vec{r} - \vec{R_A}) \tag{2.4}$$

and

$$\Phi_B(\vec{k}, \vec{r}) = \frac{1}{\sqrt{N}}\sum_{\vec{R_B}}^{N} exp(i\vec{k}\vec{R_B})\phi_B(\vec{r} - \vec{R_B}). \tag{2.5}$$

The summation runs over all respective atomic lattice sites, A or B, for all unit cells N present. The term $\phi_i(\vec{r} - \vec{R_i})$, with $i = A, B$, constitutes the atomic wavefunctions (Wannier functions) for the respective atom sites, in the following assumed to be the p_z-orbital occupied by the fourth valence electron (I will not consider the bandstructure of the sp^2-orbitals).

The eigenfunction of the solid is then given as a linear combination of the Bloch functions of the two different atomic sites. It reads:

$$\Psi_{\vec{k}}(\vec{r}) = c_A\Phi_A + c_B\Phi_B. \tag{2.6}$$

We now have to solve the time-independent Schrödinger equation with a Hamiltonian for a single electron in the atomic potential given by all the carbon atoms. After substituting Eq. 2.6 into the Schrödinger equation, multiplying it with the complex conjugate of Eq. 2.6 and integrating over the whole space,

we obtain in matrix form (details of the derivation can be found in [15]):

$$H\Psi = ES\Psi. \tag{2.7}$$

In the tight-binding approximation, electrons can only hop between neighboring atoms. Furthermore, the overlap of the Wannier functions between neighboring atoms is neglected. This yields the following form of the operators H and S:

$$H = \begin{pmatrix} E_0 & -tf(\mathbf{k}) \\ -tf^*(\mathbf{k}) & E_0 \end{pmatrix} \quad and \quad S = \begin{pmatrix} 1 & 0 \\ 0 & 1 \end{pmatrix}, \tag{2.8}$$

where we have defined a geometrical factor

$$f(\mathbf{k}) = \sum_{\mathbf{m_l}} e^{-i\mathbf{k}\mathbf{m_l}}. \tag{2.9}$$

The $\mathbf{m_l}$ are the vectors pointing to the nearest neighbor atoms of an atom of the B sublattice. In the configuration shown in Fig. 2.2 they are given by (putting the origin on an atom of the B sublattice):

$$\mathbf{m_1} = a\mathbf{e_y}, \qquad \mathbf{m_2} = \frac{\sqrt{3}a}{2}(\mathbf{e_x} - \frac{1}{\sqrt{3}}\mathbf{e_y}), \qquad \mathbf{m_3} = \frac{\sqrt{3}a}{2}(-\mathbf{e_x} - \frac{1}{\sqrt{3}}\mathbf{e_y}) \tag{2.10}$$

Inserting into the exponential form, Eq. 2.9 finally yields:

$$f(\mathbf{k}) = \sqrt{1 + 4cos(\frac{\sqrt{3}k_x a}{2})cos(\frac{k_y 3a}{2}) + 4cos^2(\frac{k_x\sqrt{3}a}{2})}. \tag{2.11}$$

The eigenvalues of Eq. 2.7 are found by solving

$$det(H - ES) = 0, \tag{2.12}$$

giving the following dispersion relation for the p_z-electrons in graphene:

$$E_{graphene}(\mathbf{k}) = E_0 \pm t \cdot |f(\mathbf{k})|. \tag{2.13}$$

E_0 corresponds to the Fermi energy and can be set to zero. t is the hopping element, with a value of t=2.66 eV (used below), as follows from a DFT calculation [15]. The band structure for graphene is shown in Fig. 2.3. Because of
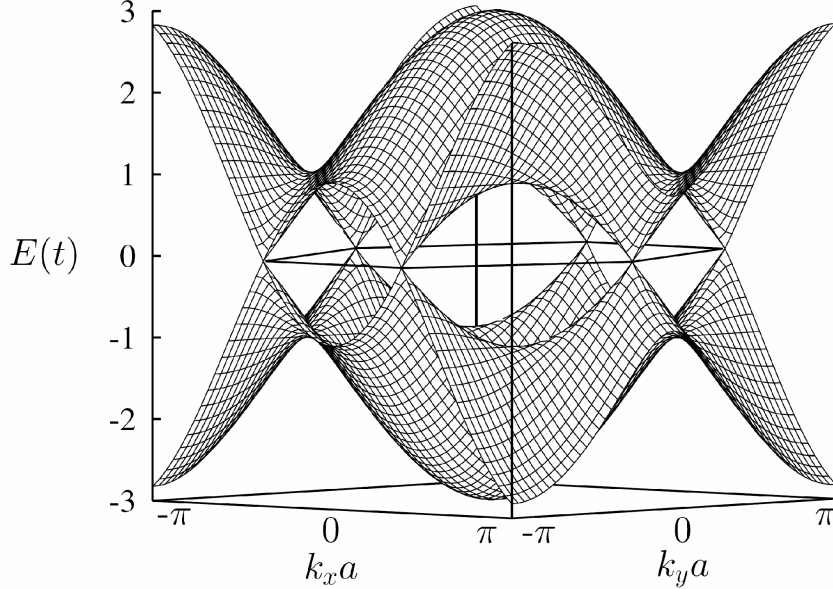
Figure 2.3: The band structure of a single graphene layer with $E_0 = 0$. The energy is given in units of the hopping element t. Valence and conduction band touch at the six corners of the Brillouin zone, which are denoted K and K'. A hexagon representing the first Brillouin zone is drawn in the image. Figure taken from [15].

the two atoms per unit cell, the dispersion relation consists of two bands, valence band ($E<0$) and conduction band (E>0). The two bands touch at the six corners of the first Brillouin zone, which are called K and K' points. Because valence and conduction band touch at these six points, graphene has a gap equal to zero. Furthermore, close to the K and K'-points, the energy varies approximately linearly with k. The remarkable property of a linear energy dispersion will be examined now in more detail, following again closely [15].

To carry out a low-energy expansion of the band dispersion for graphene, we decompose the vector $\mathbf{k}$ into a vector $\mathbf{K}$ ($\mathbf{K}'$), pointing at the point K (K'), and a small vector $\mathbf{q}$

$$\mathbf{k} = \mathbf{K} + \mathbf{q} \qquad or \qquad \mathbf{k} = \mathbf{K}' + \mathbf{q}. \tag{2.14}$$

The vectors $\mathbf{K}$ and $\mathbf{K}'$ are for example $\pm \frac{4\pi}{3\sqrt{3}a}\mathbf{e_x}$, according to Fig.2.2(b). We now insert this into the geometrical factor and carry out a Taylor expansion up to first order in $\mathbf{q}$. It follows for the $\mathbf{K}$-point

$$f(\mathbf{k}) \approx -\frac{3a}{2}(-q_x + iq_y), \tag{2.15}$$

24

while for the **K'**-point it reads

$$f(\mathbf{k}) \approx -\frac{3a}{2}(q_x + iq_y).$$

(2.16)

Because both results differ only by one sign, one can introduce a valley index α, which is -1 for the K-valley and +1 for the K'-valley. With this, the Hamiltonian for graphene in the low energy limit is then given as:

$$H_{eff}^{\alpha} = -t\frac{3a}{2}\begin{pmatrix} 0 & \alpha q_x + iq_y \\ \alpha q_x - iq_y & 0 \end{pmatrix}, \qquad with \qquad \alpha = -1, +1.$$

(2.17)

The energy dispersion resulting from this Hamiltonian reads:

$$E_{\alpha}^{\pm} = \pm\hbar v_{\mathrm{F}}|\mathbf{q}|, \qquad v_{\mathrm{F}} = \frac{t3a}{2\hbar} = 8.7 \cdot 10^5 m/s.$$

(2.18)

Hence, close to the K and K'-points the energy of the charge carriers in graphene varies linearly with $\mathbf{q}$ and is determined by a single parameter, the Fermi velocity v_{F}. This linear energy dispersion is the key to many novel properties, which have never been studied in solid-state systems before the discovery of graphene [3]. The linear dispersion can also be employed to link the physics of the charge carriers in graphene to that of relativistic particles. The energy dispersion of relativistic particles is found from the Dirac equation and is given by:

$$E = \pm\sqrt{c^2\hbar^2\mathbf{k}^2 + m^2c^4}$$

(2.19)

If we set the mass to zero, we arrive at:

$$E = \pm c\hbar|\mathbf{k}|$$

(2.20)

The last equation looks similar to the energy dispersion obtained in the low energy expansion for graphene. In the case of graphene, the Fermi velocity v_{F} plays the role of the velocity of light, c. For this reason, one can say that the electrons (and holes) in graphene, close to the K (K')-point behave as massless Dirac fermions. Accordingly, the linear energy dispersion around the K and K'-points, which in three dimensions forms cones, is referred to as Dirac cones. The effective Hamiltonian in the low-energy expansion, Equation 2.17, is called the Dirac Hamiltonian. This analogy between the physics of the charge carriers in

graphene and that of massless relativistic particles looks appealing in the sense of studying relativistic physics in a solid state system [3].

Apart from that, the linear dispersion for graphene also implies a density of states (DOS) different to that found in conventional two-dimensional electron gases (2DEGs). Starting from the linear dispersion around the K and K′-points and taking into account the four-fold degeneracy (factor 2 for spin, factor 2 for inequivalent K and K′ valleys) of the charge carriers in graphene, one can derive that the density of states for graphene takes the following form:

$$DOS(E) = \frac{2|E|}{\pi\hbar^2 v_{\mathrm{F}}^2}. \tag{2.21}$$

Two important consequences arise. First, the density of states is linear with energy E. Secondly, the DOS vanishes for $E = 0$, i.e. at the touching of the cone-shaped valence and conduction bands at the K and K′-points, the so-called Dirac points. The latter property allows to classify graphene as a zero-gap (because valence and conduction bands touch, without a gap) semiconductor (because the DOS vanishes for $E = 0$).

2.2 Introduction to Atomic Force Microscopy

The invention of the scanning tunnelling microscope (STM) [12] by Binnig et al. started the field of scanning probe microscopy (SPM). Shortly afterwards, Binnig et al. proposed the atomic force microscope (AFM) [13] in 1986. Scanning probe microscopy provides the opportunity to investigate various properties of sample surfaces in real-space. The resolution achievable with these techniques is about 100 pm parallel to the sample surface and about 10 pm perpendicular to the sample surface. In SPM, a very sharp tip is raster scanned over a sample surface, being either in contact with the sample surface, or in close vertical proximity. The movement of the tip is realized with a piezoelectric element, thus allowing a movement of the tip relative to the sample in the sub-nm range. A feedback-loop circuit is employed to control the distance between tip and sample. If the distance between tip and sample is kept constant, one is obtaining an image of constant interaction between tip and sample. This interaction is monitored by displaying the control signal used to keep the tip-sample distance constant on a PC.

In STM, a tunnelling current flows between an atomically sharp conductive tip

and the surface of a conductive sample, when the tip is in close proximity to the sample. This tunnelling current depends exponentially on the distance between tip and sample [14]. Because for insulating substrates no tunnelling current is expected to flow between its surface and a conductive tip in close vicinity, STM investigations are limited to the studies of conductive samples.

The principle underlying atomic force microscopy is to detect forces, rather than a current, acting between a given sample surface and a sharp tip, raster scanned over this surface. To detect the forces acting between tip and sample, the tip is mounted on a cantilever. The cantilever can be regarded as a leaf spring, clamped on one side. Under a given force acting on the cantilever, the cantilever responds like a spring. So the force acting on the tip is translated into the deflection of the cantilever, which can be measured. A very common method to measure the cantilever deflection is the use of an optical measurement [14]. A laser beam incident on the cantilever is reflected onto a position-sensitive photodiode (PSD, usually a four-segment photodiode). In the PSD, the optical signal is converted into a voltage, that serves as control parameter for the feedback-loop circuit.

Since AFM relies on a force-based interaction between tip and sample surface, it allows to investigate the surface properties of insulators as well as those of conductors. The principle of an atomic force microscope is shown in Fig. 2.4. In the image, a part (Δx long) of one single scan line of the AFM tip across the sample surface is shown. Once the AFM tip hits the shown step, the cantilever bends upwards. The laser reflected off the back of the cantilever now points to a more positive voltage at the four segment photodiode (consisting of four segments labelled A, B, C, D) compared to the user-defined setpoint deflection (which we assume to be zero, corresponding to the middle of all four segments). This deflection voltage is recorded by the feedback-loop, where it is compared with the setpoint deflection.

Because the measured vertical deflection in the left part is larger than the setpoint deflection, an error signal is calculated inside the feedback electronics. This error signal is then converted into a voltage, which is applied to the z-piezo element through the control electronics. This z-signal serves to adjust the vertical tip-sample distance such that the error signal at the feedback loop is zero, or close to zero. In the case shown, the generated z-signal is applied to the scanning piezo such that the scan piezo contracts (right part of the image), and hence lowers the
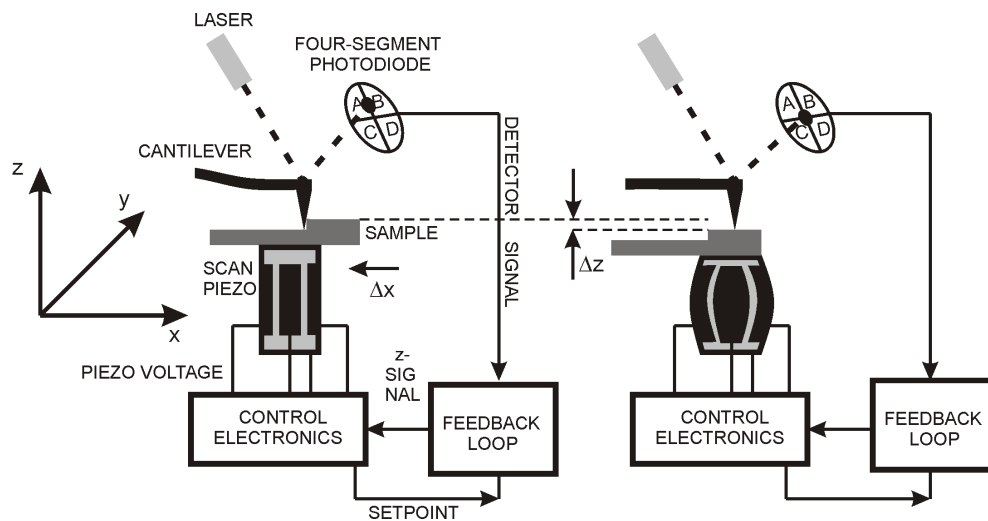
Figure 2.4: Schematics of an atomic force microscope. A sharp probe tip mounted to a cantilever is raster scanned over the surface of a sample. The interactions between the probing tip and the sample surface cause the cantilever to bend. A laser beam which is reflected from the cantilever onto a photodiode changes its position on the photodiode relative to the bending of the cantilever. A feedback-loop circuit acts as to keep the bending of the cantilever constant. This provides an image of constant interaction between tip and sample.

sample with respect to the tip. The amount Δz by which the sample is moved down is as large as it needs to be for the cantilever to bend down again, and thus maintain the setpoint deflection (zero in the case shown). The height difference Δz can be recorded as a function of the lateral tip coordinates (x,y). Displaying these data on a PC gives a real-space image of constant interaction between tip and sample. Usually, as in the case shown in Fig. 2.4, this can be interpreted as the sample topography. But one should take into account that different chemical or frictional interactions between the AFM tip and the sample can also exert a force on the cantilever, and hence require adjustment of the vertical tip sample distance.

The AFM investigations presented in this work were taken with a Digital Instruments Multimode SPM with a Nanoscope IIIa controller. This combination allows contact mode AFM, TappingMode AFM and scanning tunnelling microscopy among several other types of scanning probe investigations. The Multimode SPM keeps the cantilever at a fixed position. In order to raster scan the sample surface, the sample is moved by means of a piezo-element relative to the tip.

2.2.1 Contact mode atomic force microscopy

Relating to the schematics of contact mode AFM operation as depicted in Fig. 2.4, two different types of information about the sample surface being investigated can be obtained. As described above, one can use AFM to measure the sample topography by measuring the vertical deflection at the four quadrant photodiode. To facilitate this type of measurements, one monitors the vertical deflection given by $(A + B) - (C + D)$, where A, B, C, D stand for the voltage at the respective segment of the photodiode.

Force-distance curves

The force a cantilever exerts on the sample surface while scanning can be measured by recording a force-distance curve. An example of such a curve, recorded in contact mode AFM on a hydrogenated graphene crystal, is presented in Fig. 2.5. The vertical deflection of the cantilever, which corresponds to the photodiode voltage $(A + B) - (C + D)$, is recorded as the sample is moved towards the AFM tip (red curve) and then away (blue curve). A calibration is made to determine the sensitivity of the cantilever in normal direction, S_{normal}, which gives the voltage measured at the photodiode caused by a certain cantilever deflection. The voltage at the photodiode, generated by the laser beam reflected off the cantilever, is divided by S_{normal} to obtain a cantilever deflection in nm as a function of z-piezo movement. For each force-distance curve, the cantilever deflection of 0 nm is defined by the setpoint photodiode voltage set by the user.

At point (1), the sample is far away from the AFM tip, and hence the cantilever doesn't deflect. As the sample approaches the AFM tip, at point (2) the tip comes in contact with the sample. This situation, where the cantilever suddenly deflects downwards, is usually referred to as jump-to-contact. It occurs when the attractive forces between tip and sample overcome the restoring force of the cantilever. Moving the sample even further now leads to a positive deflection of the cantilever. For the case shown, a hydrogenated graphene flake on top of a silicon oxide surface was used as a sample, which can be considered to be infinitely hard (there shouldn't be any elastic indentation of the flake and the silicon oxide substrate). The contact stiffness is thus much higher than the spring constant of the cantilever. Therefore the measured cantilever deflection is a linear function of the movement of the sample. The measured linear dependence reflects Hooke's law. The sample is moved further in z-direction until a pre-defined limit

29
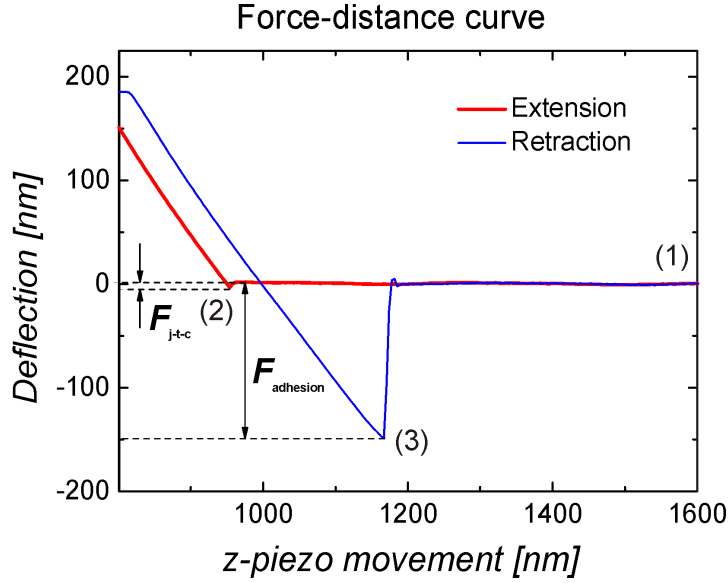
Figure 2.5: Force-distance curve measured in contact Mode AFM on a hydrogenated graphene flake. The red curve corresponds to moving the sample towards the AFM tip. At point (1), no deflection of the cantilever is observed. While the sample is moved further towards the tip, at point (2) the tip snaps into contact with the sample. At this point, the attractive forces between tip and sample overcome the restoring force of the cantilever. Further movement of the sample causes a linear deflection of the cantilever, until a user-defined limit is reached for the sample movement. During the following retraction of the sample, the cantilever deflection decreases linearly. Adhesion between tip and sample causes the cantilever to even bend downwards, until the restoring force of the cantilever overcomes adhesion at point (3). After that, the cantilever is no longer in contact with the sample.

is reached. Then, the sample will be moved away from the AFM tip, while the deflection at the photodiode is monitored. The retraction movement is displayed by the blue curve in Fig. 2.5. If adhesion is present between the sample surface and the AFM tip, the tip will remain in contact past the jump-to-contact point and is bent downward (negative deflection) until the restoring force of the cantilever becomes greater than the adhesion, which happens at point (3), and the tip snaps out of contact and returns to its initial state. After that point, the tip is no longer in contact with the sample and upon further retraction of the sample no cantilever deflection is measured.

The force the cantilever exerts on the sample surface, the spring force F_{spring}, can be obtained by multiplying the measured cantilever deflection at the point where the tip scans the sample with the normal spring constant of the cantilever.

The point where the tip scans the sample is given by the intersection of the extension cycle (red curve) with the user-defined setpoint, which defines a deflection of 0 nm. The graph shown was taken with a Nanosensors PPP-CONTR highly doped silicon cantilever, with a normal spring constant of k_{normal}=0.29 N/m. A positive spring force means that the tip is exerting a force onto the sample perpendicular to its surface. The force-distance curve shown was taken in the so-called zero force mode, where the cantilever has only a very small positive deflection while scanning the sample. Hence, for the case shown the spring force is $F_{\text{spring}}{\approx}0\ nN$. The adhesion force, F_{adh}, is defined by the difference in deflection between zero deflection (upper dashed line at point (2), far from the sample) and the deflection at the point where the cantilever snaps out of contact in the retraction cycle (dashed line at point (3))). In our case, we have $F_{\text{adh}} = 149nm{\times}0.29nN/nm = 43.2nN$. The loading force is defined as the total force with which the tip is scanning the sample, given by $F_{\text{load}} = F_{\text{adh}}+F_{\text{spring}}$.

Lateral force microscopy

A second type of measurement employs scanning the cantilever at 90° relative to the long axis of the cantilever, and measuring the lateral deflection of the cantilever according to $(A+C)-(B+D)$, while still keeping the vertical deflection of the cantilever constant.

The lateral deflection is measured at the photodiode as a voltage, U_{lateral}. Schwarz et al. [17] have shown how this lateral deflection can be converted to a lateral force acting on the AFM tip:

$$F_{lateral} = \frac{3}{4}{\cdot}k_{torsion}{\cdot}\frac{h}{l}\frac{1}{m{\cdot}S_{normal}}{\cdot}U_{lateral}. \qquad (2.22)$$

Here, h is the height of the tip on the cantilever and l is the length of the cantilever. m is defined as $m = m_{normal}/m_{lateral}$. m_{normal} is the slope of the voltage at the photodiode in vertical direction, $(A + B) - (C + D)$, versus the vertical displacement of the laser beam on the photodiode. Accordingly, $m_{lateral}$ is the slope of the photodiode voltage in lateral direction, $(A + C) - (B + D)$, versus the lateral displacement of the laser beam on the photodiode [17]. For our system, m_{normal} and $m_{lateral}$ are equal, and hence $m = 1$. S_{normal} is the sensitivity of the cantilever in vertical direction. Its unit is V/nm, and it tells,

how much Volts of vertical deflection signal at the photodiode equals a given vertical bending of the cantilever in nm. $k_{torsion}$ is the torsional spring constant of the cantilever used. It can be calculated from the geometrical dimensions of the cantilever and the torsional modulus , G, a constant specific for the cantilever material, according to [18]:

$$k_{torsion} = \frac{G{\cdot}t^3{\cdot}b}{3{\cdot}l}{\cdot}\frac{1}{h^2}. \qquad (2.23)$$

t is the thickness and b is the width of the cantilever used. h and l are defined as before (length of the cantilever and height of the tip on the cantilever, respectively).

Lateral force microscopy allows areas exhibiting different friction to be distinguished. The reason is that a different elastic modulus of the surface leads to a different contact shear strength of the surface in contact with the AFM tip. This difference leads to a different lateral deflection of the cantilever. But also the influence of changes in the topography can lead to a contrast in the lateral deflection signal. This is shown in Fig. 2.6. In the top part, the cantilever is
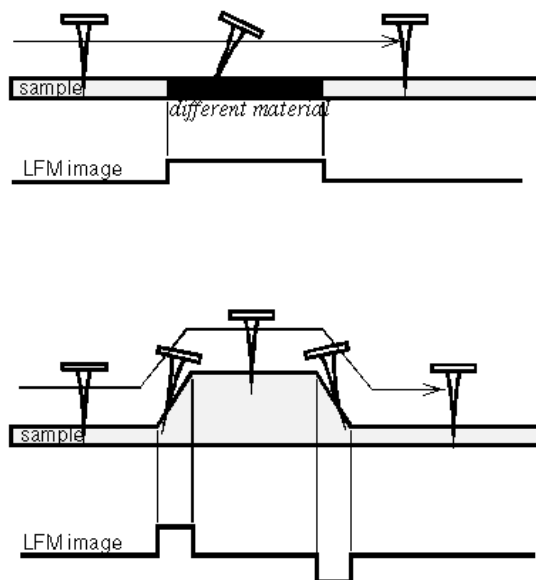
Figure 2.6: Lateral force microscopy. Scanning the cantilever perpendicular to its long axis and measuring the lateral deflection on the photodiode can be used to distinguish sample areas of different composition (top). On the other hand, topographic differences of a sample consisting of the same material will only result in small peaks in the lateral deflection signal (bottom). (*Image taken from http://www.mechmat.caltech.edu.*)

scanned across an area consisting of two different materials, but with no topographic contrast. Once the cantilever is scanned across the middle section of the sample, containing the second material, the cantilever deflects laterally as long as this material is scanned. After getting to a position where the first material is present again, the lateral deflection becomes zero again. The corresponding lateral deflection signal measured is shown below the sample topography. The non-zero lateral deflection of the cantilever in the middle part of the sample leads to a non-zero plateau in the measured lateral deflection signal, with the length of the plateau being approximately equal to the size of the area consisting of the different material. Scanning the same line across the sample backwards will lead to a plateau in the lateral deflection signal of the same length, but with the value of the plateau now taking the negative value compared to the forward scan.

On the other hand, in the bottom part of Fig. 2.6, the influence of changes in the sample topography of the same material on the lateral force signal is shown. Once the cantilever is starting to scan across the hillock, it will bend, and thus give rise to non-zero lateral deflection until the tip is on top of the hillock. On top of the hillock the lateral deflection becomes zero again. Scanning down the hillock the lateral deflection becomes non-zero again, but this time reverses its sign, because the cantilever gets bend in the opposite direction.

2.2.2   TappingMode atomic force microscopy

In TappingMode AFM, the cantilever is forced to oscillate permanently at, or close to its resonance frequency. This oscillation can be characterized by its oscillation amplitude, its oscillation frequency and its oscillation phase. This is shown in Fig.2.7. As soon as the oscillating cantilever is brought close to the surface, the force gradient $\delta F/\delta z$, present due to the interaction between tip and sample, will shift the resonance frequency of the oscillating cantilever. If $\delta F/\delta z$ is assumed to be constant over the cantilever oscillation, one can calculate the resulting cantilever frequency f_r, with effective spring constant $k_{eff} = k + \delta F/\delta z$ according to [19]:

$$f_r = \frac{1}{2\pi}\sqrt{\frac{k + \delta F/\delta z}{m_{eff}}}.$$

(2.24)
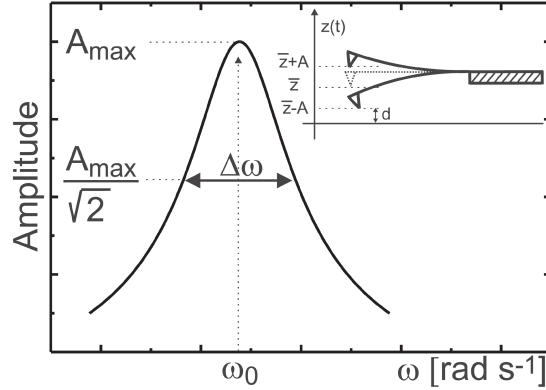
Figure 2.7: Parameters of the forced oscillation of the cantilever in TappingMode AFM. The amplitude of the oscillating cantilever reaches its maximum A_{max} when the cantilever is forced to oscillate at or close to its resonance frequency ω_0. The bandwidth is the width of the resonance curve for an amplitude $A_{max}/\sqrt{2}$. Inset: The cantilever oscillates periodically around a mean value $\bar{z}$ with an amplitude A. d is the smallest distance between tip and sample. Taken from Ref. [19].

This implies that for repulsive forces the resonance will shift to higher frequencies, as shown in Fig. 2.8. In amplitude modulation TappingMode AFM, the cantilever oscillation is driven at a constant frequency ω_d, close to its natural resonance frequency, ω_0, with a fixed amplitude. If the natural resonance frequency of the cantilever oscillation is shifted to ω_r due to interactions between tip and sample, the oscillation amplitude measured at ω_d changes [19]. To measure and display the interaction between tip and sample, the tip-sample distance is adjusted in a way to keep the oscillation amplitude constant. A feedback-loop circuit compares the measured amplitude with a user-defined set-point amplitude and calculates an error signal. This error signal is then converted into a control signal that is applied to the z-piezo, in order to move the sample relative to the tip such that the user-defined set-point amplitude is maintained. The control signal applied to the z-piezo is displayed on a PC. Similar to contact mode AFM, a topography corresponding to constant force between tip and sample is obtained.

2.3 Introduction to scanning tunnelling microscopy

The scanning tunnelling microscope (STM) was invented and applied for the first time by Gerd Binnig and Heinrich Rohrer in 1982 [12] [20]. The name derived
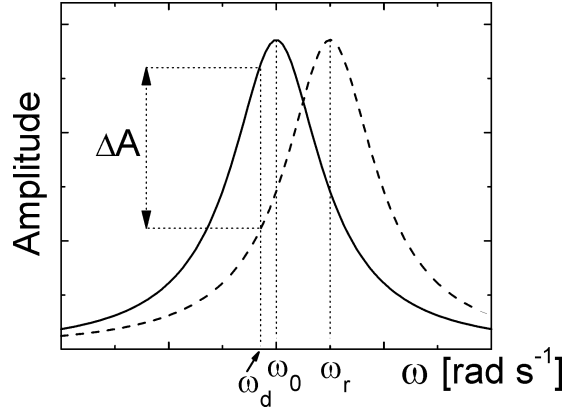
Figure 2.8: In TappingMode AFM, repulsive forces between tip and sample shift the free resonance curve (solid line, far away from the surface) towards higher frequencies (dashed curve) by an amount equal to $\Delta\omega$. In amplitude modulation TappingMode AFM, the driving frequency, indicated by ω_d, with which the cantilever is forced to oscillate is fixed. Therefore, the measured oscillation amplitude at this frequency has decreased by an amount ΔA compared to the free oscillation (far away from the surface). In order to maintain the free amplitude, the sample has to be moved away from the tip, in order to compensate for the repulsive forces. After Ref. [19].

from the quantum mechanical tunnel effect that was first experimentally observed and described in field emission experiments [21]. The quantum mechanical tunnel effect allows particles to penetrate a thin barrier, whose energetic maximum is higher than the energy of the particle. In STM, as depicted in Fig. 2.9, the tunnel effect is exploited by bringing two conductive electrodes into close vicinity, with one electrode being a sharp metal tip (typically made from Ir, W or PtIr) and the other one being the sample to be investigated. The distance between the tip electrode and the conductive sample electrode is typically on the order of few Å [14]. Applying a bias voltage between tip and sample leads to a tunnel current flowing through the barrier between tip and sample, which is typically on the order of 1pA up to few nA [14]. Below, it is discussed how this can be used to obtain real-space images of the sample surface.

The magnitude of the tunnel current depends exponentially on the width of the barrier. Changing the barrier width by 1 Å leads to a change in the measured tunnelling current by one order of magnitude. This strong dependence on the tip-sample distance (that eventually defines the barrier width) leads to the fact that only the outermost atoms of the tunnelling tip, in the ideal case only one single atom, contribute to the formation of the tunnelling current. The result is the possibility of achieving atomic resolution in scanning tunnelling microscopy.
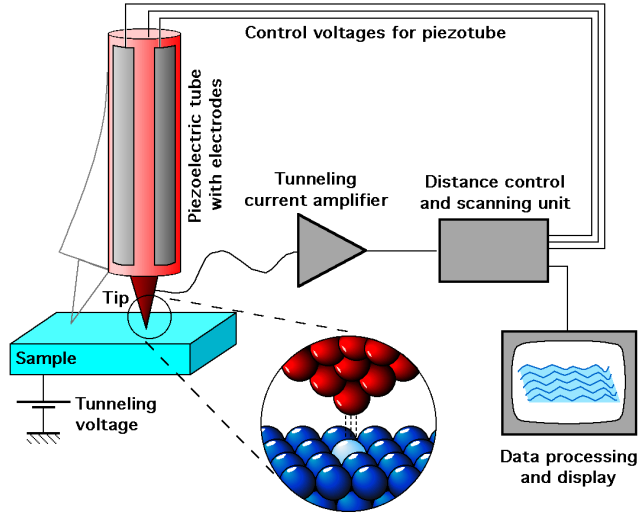
Figure 2.9: Principle of STM. A sharp metallic tip is raster-scanned parallel to the surface of a conductive sample in close vertical vicinity, while a bias voltage is being applied between tip and sample. The tunnelling current flowing between the outermost tip atom and the sample surface is amplified. The tip is raster-scanned across the sample surface by means of piezoelectric elements. The tunnelling current flowing at each point is determined by the local geometric and electronic structure of the surface. After amplification, it is processed by the control unit. In this way, one can obtain a real-space image of the surface, ideally with atomic resolution. (*Image taken from http://commons.wikimedia.org.*)

2.3.1 Theory of scanning tunnelling microscopy

A sketch of the energy diagrams for tip and sample in tunnelling contact can be seen in Fig. 2.10. The sample is here assumed to be undoped graphene, with its density of states being $\rho_{sample}(E) \propto |E|$. The tip is shown to have an energy-independent density of states, $\rho_{tip}(E) = const.$. In both, tip and sample electrode, the available states are filled up to the Fermi energy, E_F. The two electrodes are separated by a small vacuum gap z_0, with the tip being positioned at $z{=}0$. An applied bias voltage V across this tunnel junction shifts the two Fermi energies relative to each other, by an amount eV. We use the convention that a positive bias voltage applied to the sample increases the energy in the tip. The distance z, the two work functions of tip and sample, Φ_t and Φ_s, and the energy eV represent a trapezoidal tunnel barrier for the electrons.

According to quantum mechanics [22], an electron in the tip can be described

36
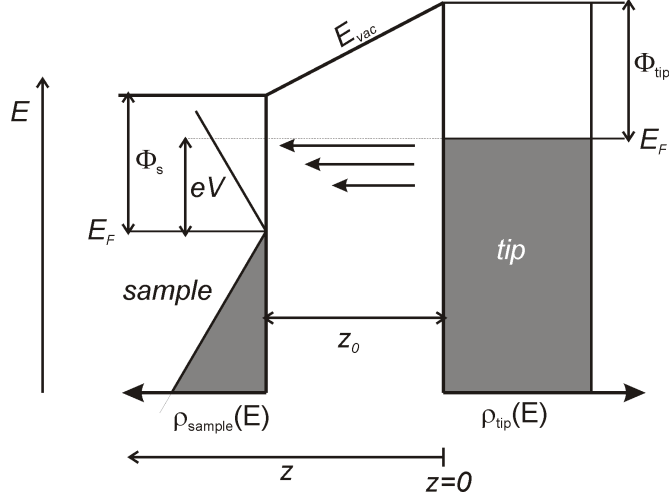
Figure 2.10: Schematic view of the tunnelling process between a tip with a constant density of states, $\rho_{tip}(E) = const.$ and a graphene sample with a local density of states $\rho_{sample}(E) \propto E$. The distance between tip and sample is z_0. The tip is positioned at $z = 0$. When a positive voltage V is applied to the sample with respect to the tip, electrons from occupied states in the tip can tunnel into unoccupied states of the sample, as indicated by the arrows inside the barrier region. Therefore they must overcome the barrier formed by the sum of the workfunctions Φ_s of the sample and Φ_{tip} of the tip and the applied bias energy eV.

by its wave function Ψ. By applying the bias voltage V, a tunnelling current occurs. The probability density of observing an electron at a point z inside the sample electrode is proportional to:

$$|\Psi(0)|^2 e^{-2\kappa z} \qquad with \qquad \kappa = \frac{\sqrt{m(\Phi_t + \Phi_s - 2E + eV)}}{\hbar}. \qquad (2.25)$$

Because it has a non-zero value, there is a non-zero probability for the electron propagating through the barrier.

The total current measured at the sample electrode is hence proportional to $e^{-2\kappa z}$. Using the free electron mass, assuming the tip and sample work functions to be equal and assuming that the bias is much smaller than the value of the work function, the decay constant can be expressed as:

$$\kappa = 5.1\sqrt{\Phi(eV)}nm^{-1}. \qquad (2.26)$$

Taking an average value of the work function of $\Phi \approx 5$ eV [22], the decay constant becomes $\kappa \approx 11.4$ nm^{-1}. The current thus decreases by one order of magnitude per 0.1 nm increase in the barrier separation z.

A theoretical description of electron tunnel experiments in planar tunnel junctions (consisting of two planar metal electrodes separated by an insulating layer) was first given by Bardeen [23]. His quantum mechanical time-dependant perturbation approach allows to calculate the tunnelling current flowing between two planar metal electrodes separated by a thin insulator under an applied bias voltage. For the tunnelling current between the two electrodes, as shown in Fig. 2.10, it follows [22]:

$$I = \frac{4\pi e}{\hbar} \int\limits_{-\infty}^{\infty} [f(E_F - eV + \epsilon) - f(E_F + \epsilon)] \tag{2.27}$$

$$\times \rho_{tip}(E_F - eV + \epsilon)\rho_{sample}(E_F + \epsilon)|M|^2 d\epsilon, \tag{2.28}$$

where $f(E) = (1 + exp[(E - E_F)/k_bT])^{-1}$ is the Fermi distribution function. ρ_{tip} and ρ_{sample} are the density of states (DOS) of the tip and sample electrode, respectively. The tunnelling matrix elements M are given in one-dimensional form by [22]:

$$M = -\frac{\hbar^2}{2m} \int\limits_{z=0} [\chi^* \frac{\partial \psi}{\partial z} - \psi \frac{\partial \chi^*}{\partial z}]dxdy, \tag{2.29}$$

where the integration goes over the sample surface, $z=0$. m is the electron mass, ψ is a wave function of an electron in the sample, and χ is a wave function of an electron in the tip.

If k_BT is smaller than the energy resolution required in the measurement, then the Fermi distribution function can be approximated by a step function [22]. The tunnelling current then reads:

$$I = \frac{4\pi e}{\hbar} \int\limits_{0}^{eV} \rho_{tip}(E_F - eV + \epsilon)\rho_{sample}(E_F + \epsilon)|M|^2 d\epsilon. \tag{2.30}$$

The last equation can be further simplified, if one makes the following assumptions [22],

1. the tip state is spherically symmetric;

2. the tunneling matrix element does not depend on energy level;

3. the tip DOS is a constant over the energy interval of interest; and

4. the sample DOS varies in energy not much in each k_BT.

This yields the following formula for the tunnelling current:

$$I \approx \frac{4\pi e}{\hbar} \rho_{tip} |M|^2 \int_0^{eV} \rho_{sample}(E_F + \epsilon) d\epsilon. \tag{2.31}$$

Since the DOS of the tip is independent of E, it can be taken out from the integration, and taken as a constant.

Tersoff and Hamann [24, 25] now evaluated the tunnelling matrix element M by modelling the tip as a geometrical point, with arbitrarily localized potential and wave functions. The matrix element $M_{\mu\nu}$ is then simply proportional to the amplitude of the wave function of an electron in the sample Ψ_{sample} at the position $\mathbf{r_0}$ of the tip:

$$M \propto \Psi(\mathbf{r_0}). \tag{2.32}$$

Using this expression for the tunnelling matrix element, the tunnelling current reads:

$$I \propto \rho_{tip} |\Psi(\mathbf{r_0})|^2 \int_0^{eV} \rho_{sample}(E_F + \epsilon) d\epsilon. \tag{2.33}$$

With the definition that the local density of states of the sample at the energy level E at the center of curvature of the tip is

$$\rho_{sample}(E, \mathbf{r_0}) \equiv |\Psi(\mathbf{r_0})|^2 \rho_{sample}(E) \tag{2.34}$$

the tunnelling current is proportional to

$$I \propto \int_0^{eV} \rho_{sample}(E_F + \epsilon, \mathbf{r_0}) d\epsilon. \tag{2.35}$$

Hence the STM image is related to a property of the surface alone [22]. Thus, in the Tersoff-Hamann model, the STM image is a contour map of constant surface LDOS, i.e. the charge density from sample states at the Fermi level.

2.3.2 STM imaging modes

Images are obtained by scanning the tip over the sample surface line by line. This raster-scanning is facilitated by piezoelectric elements that are either mounted to the tip, with the sample being fixed, or vice versa. Applying well-defined voltages to the piezo elements changes their shape and thus lead to a movement of the parts rigidly mounted to the piezo elements. In order to achieve atomic resolution, two operating modes are used for scanning tunneling microscopy, both shown in Fig.2.11:
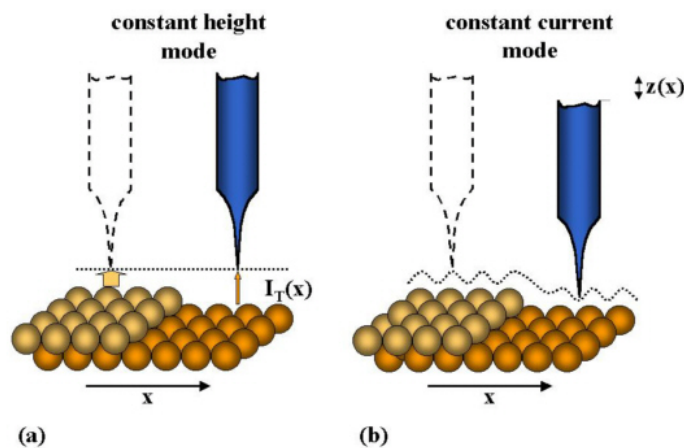
Figure 2.11: Left: Constant height mode. The tip is scanned in a constant height above the sample surface, and changes in the tunnelling current are measured. On the upper terrace shown, the tip is closer to the sample than on the lower one, thus leading to higher tunnelling current flowing as indicated by the thicker arrow between tip and sample. Right: Constant current mode. The vertical distance between tip and sample is adjusted such that the tunnelling current flowing is kept constant. When going from the higher to the lower terrace, the tip is moved down accordingly. (*Image taken from http://www.fz-juelich.de.*)

- The constant-current mode. In constant-current mode an image of constant tunnelling current flowing between tip and sample is obtained. A feedback loop consisting of a proportional and an integral circuit compares the measured value of the tunnelling current at each point with the setpoint value for the tunnelling current. From the calculated difference a voltage is generated, which is applied to the piezoelement responsible for adjusting the tip-sample distance. This leads to a permanent adjustment

of the tip-sample distance, such that the difference between the measured tunnelling current and the setpoint value is minimal at each point. While the tip is raster-scanned across the sample surface, the voltage applied to the z-piezo, to keep the tunnelling current constant close to the setpoint value, is recorded and displayed. The image obtained in this way shows contours of constant local density of states (LDOS) of the sample surface close to the Fermi level.

- The constant-height mode. In this mode, the feedback loop is limited to a very narrow bandwidth, while the tip is raster-scanning the sample surface. The result is that the distance between tip and sample surface is almost constant during the measurement. One records the tunnelling current flowing between tip and sample surface. The change in the tunnelling current is then interpreted as the change in topography at the corresponding points of the sample surface. This method allows for very high scanning speeds, since no adjustment of either tip or sample is necessary. High scanning speeds are desirable in order to minimize the influence of thermal drift. Nevertheless, a disadvantage of this method is that it is limited to very flat sample surfaces. Otherwise, tip and sample might touch each other at very small tip-sample separations, or in case of too large tip-sample separations, no tunnelling current might be measured at all.

The images obtained with scanning tunneling microscopy are images of the local density of states of the sample surface. Thus an exact assignment of STM images to the position of atoms on the sample surface is only permitted in certain cases.

2.3.3 Considerations on Vibrational Stability

The tunnelling current flowing between a conductive tip and the surface of a conductive sample in STM experiments depends exponentially on the distance between tip and sample surface. A change of this tip-sample-distance of 1 Å thus leads to a change in the tunneling current of 1 order of magnitude. In order to successfully perform STM experiments, the mechanical stability of the distance between tip and sample, Δz, has to be $\Delta z \simeq 1$ pm $= 1 \cdot 10^{-12}$ m, according to [26]. Building vibrations can be regarded as the main sources jeopardizing STM investigations. They are caused either through wind load and seismic activities (e.g. traffic) with vibration frequencies in the range between 1 Hz and 10 Hz. The

other major source of building vibrations comes from machines in the building, operated at the line frequency of 50 Hz. This produces vibrations in the range between 10 Hz and 100 Hz, with maximal amplitudes lying typically between 15 Hz and 20 Hz [26].

In order to allow ourselves to perform STM experiments, a vibration-isolation setup was constructed, shown in Fig. 2.12, which should considerably reduce the influence of building vibrations on the scanning probe microscope. The vibration isolation stage consists of a metal-cage C, in which the scanning probe unit (consisting of an optical microscope D and the actual scanning probe microscope, E) is placed. Afterwards the whole cage gets suspended from the ceiling A of a lab located in the basement of Schuster Building (University of Manchester) through elastic bungee ropes B. The whole microscope is then suspended freely in a certain height above the floor F. The STM images presented in a later chapter are a clear proof that this vibration isolation is sufficient to achieve atomic resolution on both HOPG and graphene under ambient conditions.

2.4   AFM topography of graphene

The proof, whether a given flake of graphite consists out of just one atomic layer of carbon atoms is a non-trivial task. The theoretical thickness of a single graphene layer is 3.35 Å, which is close to the resolution limit of scanning probe microscopes. For the Digital Instruments Multimode AFM with Nanoscope IIIa controller, the ultimate resolution perpendicular to the sample surface is given to be between 0.3 Å and $\sim$1 Å by the manufacturer [27]. Two methods to determine the height of a given graphite flake on a substrate are optical microscopy and atomic force microscopy. With optical microscopy, one is able to spot graphite flakes of monoatomic height (single-layer graphene) on an oxidized silicon wafer [1,28]. An optical image of single layer graphene is shown in the left part of Fig. 2.13. The image shows two single layer graphene sheets. This could be confirmed by means of atomic force microscopy (AFM) investigations. On the right, an AFM image of the marked area in the optical image, shown on the left, is displayed. The measurements were performed under ambient conditions with a Digital Instruments Multimode atomic force microscope with Nanoscope IIIa controller.
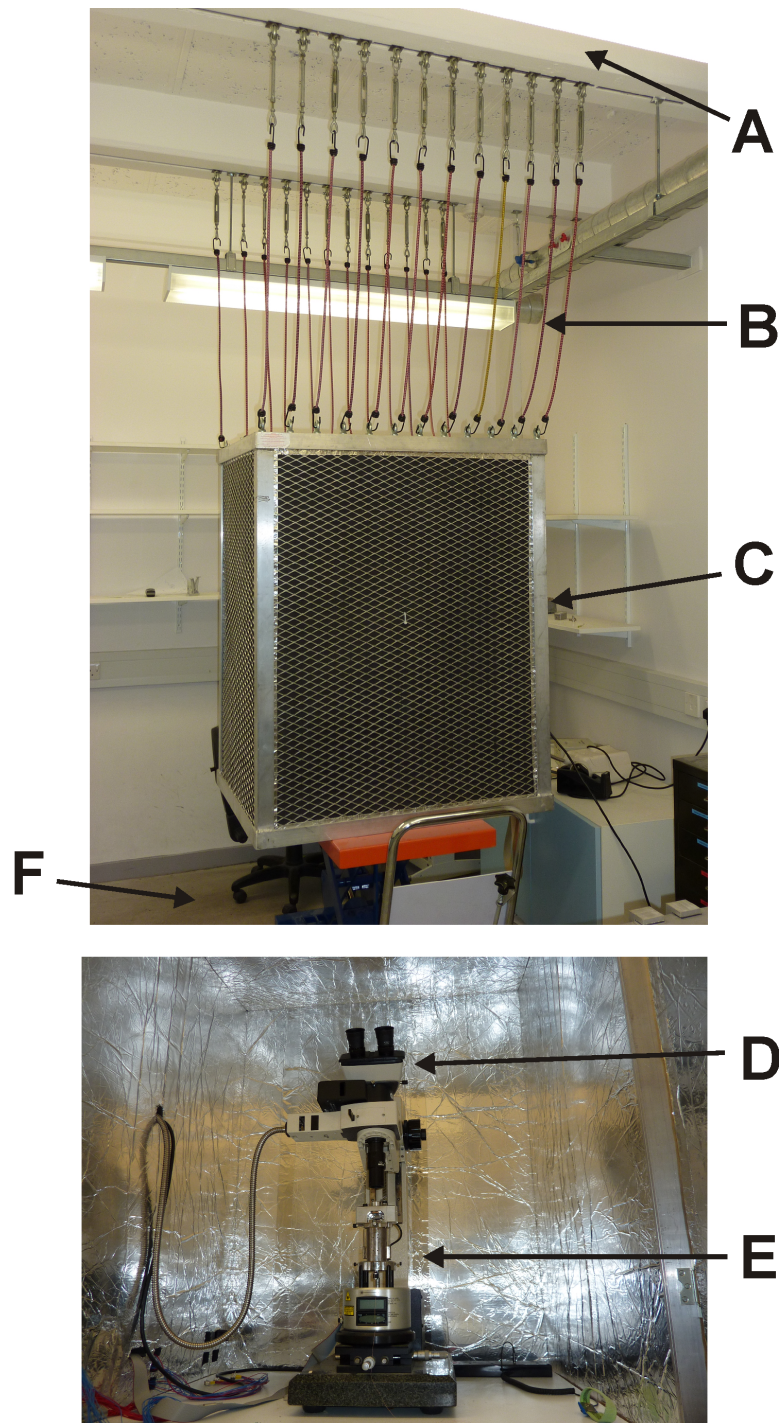
Figure 2.12: The scanning probe unit, consisting of the SPM E and an optical microscope D, is placed in a metal cage C. This cage is suspended from the ceiling A of the lab through elastic bungee ropes B. Thus, the whole setup is hanging freely above the ground floor F.
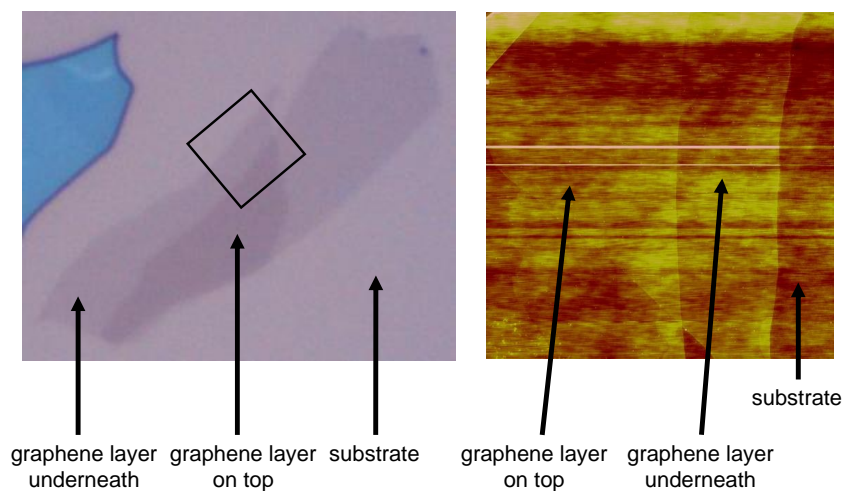
Figure 2.13: The left part shows an optical microscope image of single layer graphene. The magnification used was 100 times. One graphene sheet lying over another one can be seen. The optical contrast between each graphene layer and the underlying SiO_2-substrate is the same, thus indicating the same thickness for both layers. (*Sample and image courtesy of Peter Blake, University of Manchester.*) The right part shows an image taken with TappingMode AFM. It shows the raw data without any image processing applied. It corresponds to the marked area in the optical image. The different parts of the image are indicated. The image size is 6.2 μm×6.2 μm.

To confirm, that the graphene layers identified with optical microscopy are indeed single layer sheets, the TappingMode AFM image shown in Fig. 2.13 was evaluated in terms of determining the step height between the imaged terraces. The results are given in Fig. 2.14 and Fig. 2.15, respectively. The stepheight between the two graphene layers was determined to be 4.1 Å, which is very close to the vertical separation of 3.35 Å of individual graphene layers inside a graphite crystal. Since both layers show the same contrast in the optical image, Fig. 2.13, this result confirms that the given sample consists of two single layer graphene flakes.

The observation that the step height from the SiO_2 surface to the first graphene layer after averaging is not around 4 Å, but rather 8 Å, i.e. twice the value expected, could be due to the presence of ambient species, like nitrogen, oxygen or water between the first graphene sheet and the SiO_2-surface, or on top of the graphene sheet [29]. AFM experiments of measuring the step height of a graphene
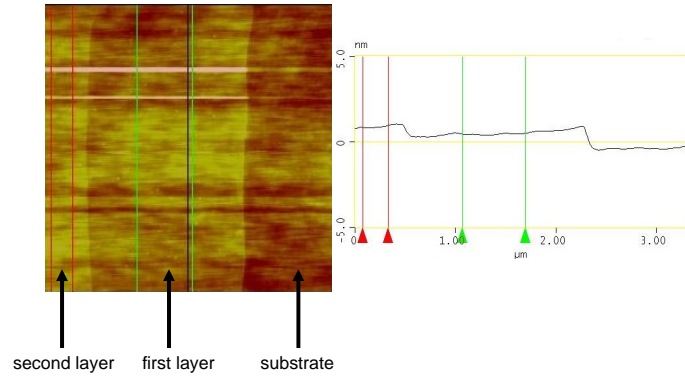
Figure 2.14: The left part shows an image obtained with Tapping-Mode AFM. It has a size of 3.317μm $\times$ 3.317μm. Three different areas in this image have been indicated by arrows. To measure the hight between adjacent terraces, all lines parallel to the vertical black line have been averaged. The averaged linescan is shown in the right part of the image. The stepheigt between terraces is determined as the difference between the averaged z-positions of the red and green cursors, each pair being positioned on one terrace. In this way the stepheight between the second graphene layer and the first graphene layer was determined to be 4.1 Å.
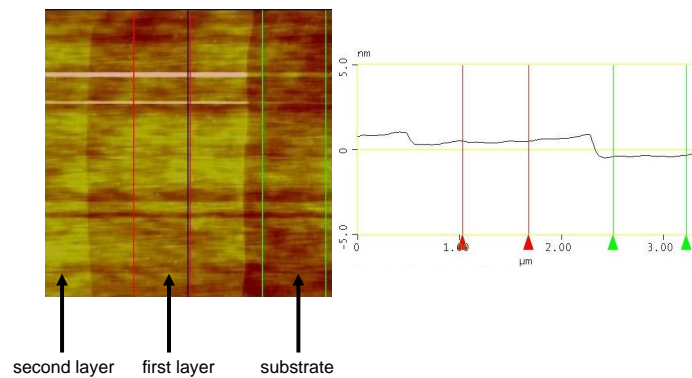
Figure 2.15: The same averaged linescan as in Fig. 2.14 was taken to determine the stepheight between the SiO_2-substrate and the first graphene layer. The stephight between the first graphene layer and the underlying SiO_2-substrate was determined to be 8.4 Å.

flake on SiO_2 carried out in ultrahigh vacuum [29] directly gave a value of 4 Å. Additionally, it was reported [30] that when the step height of graphene on SiO_2 was measured by AFM immediately after the sample has been taken out of vacuum storage (graphene flake stored under a pressure of 1×10^{-6} Torr for several days), the measured step height between the flake and the SiO_2-surface was also found to be only 4 Å.

A further point was made by Song and Cho [31], who studied the interaction between single layer graphene and different dielectric substrates. They found an increase in the step height between graphene and the substrate obtained from AFM images after averaging, when going from substrates with high dielectric constant to a substrate with lower dielectric constant. They attribute this increase in step height to a decrease of van der Waals interaction between the graphene layer and the substrate.

2.5 Raman spectroscopy on graphene

Raman spectroscopy is a very useful tool in studying graphene. In [32], it has been shown how Raman spectroscopy can be used to determine the number of graphene layers being present in graphite thin films. With Raman spectroscopy, it is possible to unambigously determine whether a given ultrathin graphite sample consists of only one atomic layer.

A typical Raman spectrum obtained for a pristine single layer graphene crystal is shown in Fig. 2.16. The spectrum shown has been obtained using a Renishaw Raman spectrometer with an excitation wavelength of 514 nm. The size of the laser spot was around 2 μm.

The most important features of this spectrum are as follows. First, the so-called G-peak at a wavelength of 1580 cm^{-1}. This peak is observed for all graphitic materials. The second important peak is the so-called 2D-peak (sometimes also referred to as G′-peak) at around 2700 cm^{-1}. The 2D-peak can be used to determine the number of graphene layers for a given ultrathin graphite sample.

In the case of single layer graphene, the 2D-peak is a single Lorentzian [32]. If this criteria is satisfied for a given sample, then the given sample consists of a single layer graphene crystal. As an example, the 2D-peak of the Raman

Raman spectrum of graphene

514nm excitation wavelength

2D-peak
2673cm^{-1}
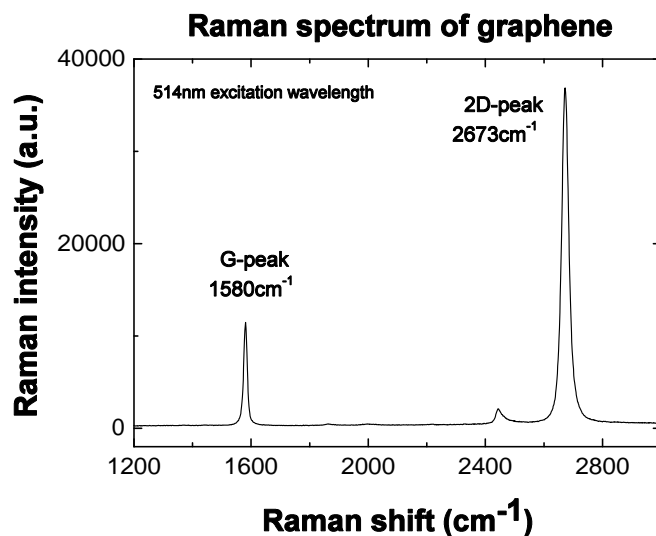
G-peak
1580cm^{-1}

Figure 2.16: Raman spectrum of a single layer graphene flake obtained at an excitation wavelength of 514nm. The peaks routinely observed are the G-peak at 1580 cm^{-1}, present in all graphitic materials, and the 2D-peak at around 2700 cm^{-1}. The 2D-peak can be used to determine the number of layers in a given ultrathin graphite sample.

spectrum in Fig. 2.16 and the plot of single Lorentzian lineshape to fit the 2D-peak are shown in Fig. 2.17. For bilayer graphene, the 2D-peak can no longer be described by a single Lorentzian lineshape, but rather as a convolution of four Lorentzians. Additionally, when comparing the full width at half maximum, bilayer graphene has a FWHM twice as large as that for single layer graphene [32]. These two observations, as well as the evolution of the Raman spectrum for samples consisting of even more layers, are shown in Fig. 2.18.

In defected graphene, one additionally observes the so-called D-peak at around 1350 cm^{-1} [32]. The fact that there is no such peak observed in the Raman spectrum shown in Fig. 2.16 indicates the absence of a significant number of defects in the sample that was measured.
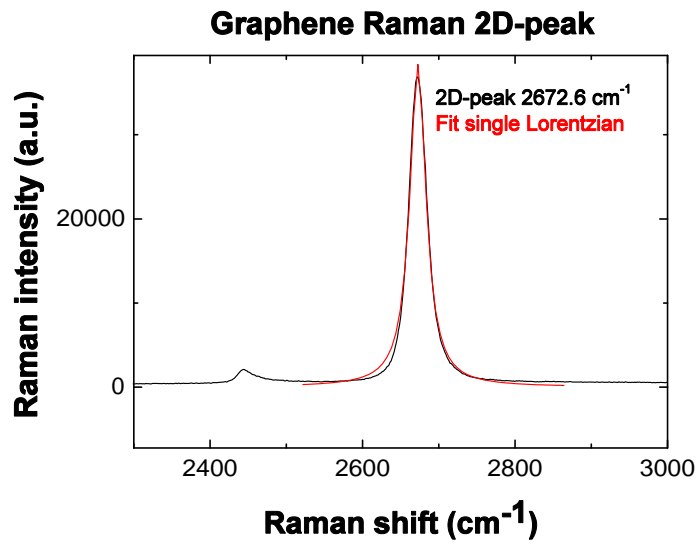
Figure 2.17: Magnification of the 2D-peak of the Raman spectrum (black curve) shown in Fig.2.16. A single Lorentzian lineshape (red curve) has been fitted to the experimental data. One clearly sees a very good agreement between the fit and the experimental data. This indicates that the measured 2D-peak consists of a single, sharp and symmetric peak and thus confirms that our sample is a single layer graphene crystal.
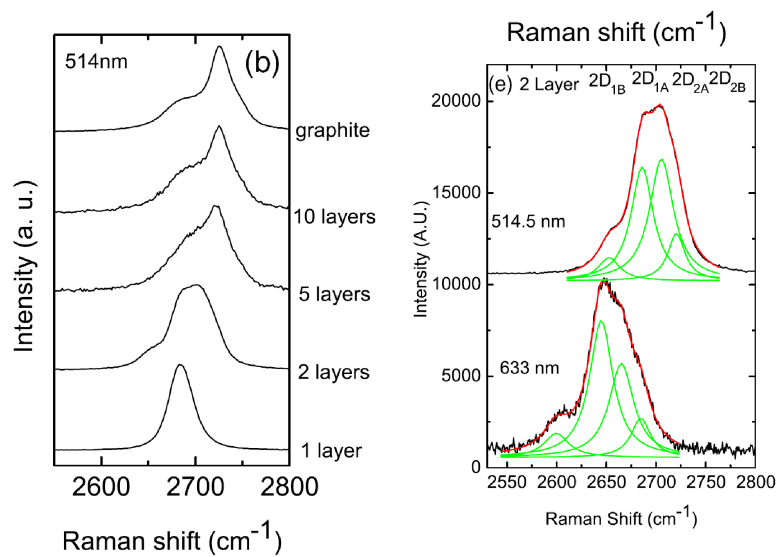
Figure 2.18: In the left part, the evolution of the Raman 2D-peak of ultrathin graphite samples with the number of constituting graphene layers, obtained at an excitation wavelength of 514 nm, is shown. While for a single graphene layer the 2D-peak at about 2680 cm^{-1} is a single Lorentzian, it broadens more and more with an increasing number of graphene layers. For bilayer graphene, the 2D-peak is already twice as broad as in the case of single layer graphene. The right part of the image shows two Raman spectra for the 2D-peak of bilayer graphene, obtained at two different excitation wavelengths, as well as the deconvolution of this peak into four Lorentzians. This is in stark contrast to single layer graphene, where one only has a single Lorentzian peak. Figure taken from Ref. [32].

Chapter 3

Scanning probe lithography on graphene

Graphene, since its first experimental observation in 2004 [1], attracted great attention due to the remarkable electronic properties. Very high mobilities and charge carriers behaving as massless Dirac fermions, open bright prospects both in the field of future integrated device electronics, as well as in the field of more fundamental studies aiming at exploring the properties of Dirac fermions in solid-state structures [3]. Confining the macroscopically sized graphene flakes down to nanometre sizes [33, 34, 35] combines its unique properties with quantum phenomena arising from confinement. To carve nanostructures out of graphene, most commonly electron beam lithography with subsequent reactive ion etching is carried out [33, 34, 35, 36]. A promising alternative is given by AFM-based local anodic oxidation (LAO), also referred to as scanning probe lithography, since it offers resist-free structuring and thus avoids contaminating the graphene flake with resist residues. First being applied to silicon [37] and metal surfaces [38], scanning probe lithography was also used to manipulate the surface of graphite (HOPG) [39] and to create nanoelectronic devices by patterning two-dimensional electron gases [40, 41]. In [42] it was first shown how this technique can be applied to perform nanolithography on graphene. Subsequently, first examples of graphene-based nanoelectronic devices created by scanning probe lithography were reported [43, 44, 45].

3.1 Introduction to local anodic oxidation

In local anodic oxidation (LAO), the conductive tip of a scanning probe microscope acts as a cathode, while the surface of the conductive sample to be oxidized is the anode. Usually, a water layer present on the sample surface acts as the electrolyte between AFM tip and sample surface.

In order to perform LAO, a voltage between the AFM tip and the surface has to be applied. This voltage creates a very high electric field at the apex of the AFM tip, which eventually causes the formation of OH^--ions in the water layer present on the substrate surface. These hydroxide ions react with the substrate, causing an oxidation of the substrate material.

When the AFM tip is brought into close vicinity of the sample surface, the water layer on the sample surface forms a meniscus between the AFM tip and the sample surface, as shown in Fig. 3.1. Shape and dimensions of the meniscus
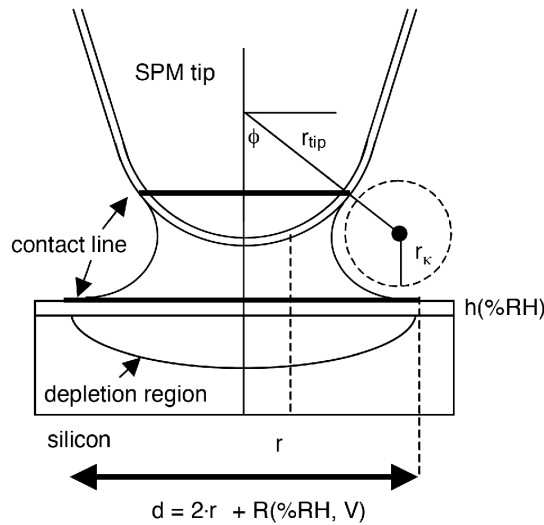
Figure 3.1: The water layer on the sample surface forms a meniscus with the AFM-tip being close to the sample surface. Shape and size of the meniscus depend on the voltage applied between AFM-tip and sample, the hydrophobicity of both tip and sample and the relative humidity. The meniscus formed determines the lithographic resolution of SPL, as indicated by d in the sketch. Graphic taken from Ref. [46].

depend on how hydrophobic or hydrophilic the tip and the substrate are, as well as the relative humidity and the tips radius Ref. [46]. The size of the meniscus, d in Fig. 3.1, limits the lithographic resolution. When a negative voltage is applied between AFM tip and grounded sample, the hydroxide ions gather kinetic energy

in the electric field before they hit the substrate. Depending on the substrates chemical reactivity and the incident kinetic energy, the hydroxide ions can either oxidize the substrate (oxide formation) or etch it, i.e. remove material from the substrate [47].

3.2 Experimental set-up for scanning probe lithography

In order to carry out scanning probe lithography, we need to consider several factors. First, we have to ensure that we can apply a bias voltage between tip and sample. This is done by electrically connecting both the sample and the AFM tip. Furthermore, we have to be able to control and adjust the humidity, in which the LAO experiments are performed. Since the humidity controls the amount of water on the sample, it is a key parameter in local anodic oxidation experiments. Our scanning probe lithography experiments were carried out using a Digital Instruments MultiMode scanning probe microscope (labelled C in Fig. 3.2) with a Nanoscope IIIa controller and a signal access module (SAM, F). The SPM is mounted under an optical microscope (E), which itself is placed on a stone block for vibration isolation. The MultiMode SPM is equipped with a AS-130 scanner, which offers a horizontal scan range of up to 125×125 μm^2 and allows for a vertical movement of the sample of 5 μm. For performing local anodic oxidation experiments, we used Nanosensors PPP-CONTR (n$^+$-doped silicon, resistivity 0.01-0.02 Ωcm, tip radius < 10 nm) contact mode cantilevers or NT-MDT NSG11/TiN AFM-tips (TiN conductive coating, tip radius < 35 nm).

The entire scanning probe microscope was operated inside an air-tight enclosure (plastic bag A), allowing for control of the relative humidity between tip and sample. In order to change the relative humidity, we used a hotplate with a beaker filled with distilled water. Therefore the beaker is also covered by a plastic bag (D) and connected to the plastic bag housing the SPM. To probe the humidity, a Farnell ST-321 THERMO HYGROMETER (accuracy +/- 3.5% relative humidity) was held $\approx$10 cm in front of the sample inside the SPM.

The electrical connections used for local anodic oxidation on graphene are sketched on the left in Fig. 3.3. A voltage between the tip and the sample is applied by a Keithley 2410 source meter through the Nanoscope signal access

(a)   (b)
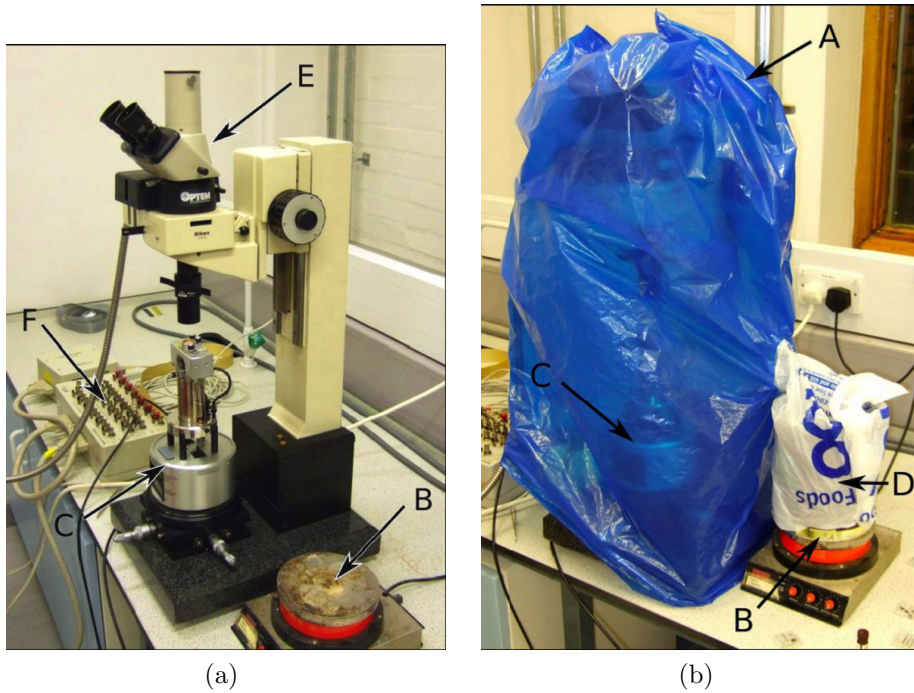
Figure 3.2: The experimental set-up: A plastic bag (A) covers the Digital Instruments Multimode SPM (C) to create an environmentally controlled atmosphere. The hot plate (B) heats a beaker containing distilled water. The beaker is covered with a plastic bag (D), to increase the humidity at the AFM. SPM and optical microscope (E) are placed on a solid block to allow for vibration isolation. The AFM-tip can be electrically contacted through the signal access module (F).

module. Before placing the samples in the SPM, the samples were mounted on a chip-carrier to contact them electrically via a break-out box. For in-situ resistance measurements a SR830 lock-in amplifier (Stanford Research Systems) was connected to the break-out box in either a 2-probe or 4-probe set-up. Self-written LabVIEW (National Instruments Corporation) programs control the SourceMeter and lock-in amplifier as well as they record the data (current flowing between tip and sample and sample resistance). A typical sample which was investigated is shown on the right side in Fig. 3.3: on top of a silicon wafer (B), several graphene flakes of different thicknesses (D) are contacted by electrical contacts, (C), made from Ti/Au. At least one of the contacts is set to ground while performing SPL on a graphene device. Before structuring the graphene samples, they were annealed for 2.5 h at 250°C in a H_2/Ar atmosphere. This treatment was suggested by Ishigami et al. [29] in order to remove any residual photoresist on the graphene flake. However, a thin film of material remained, but could eventually be removed
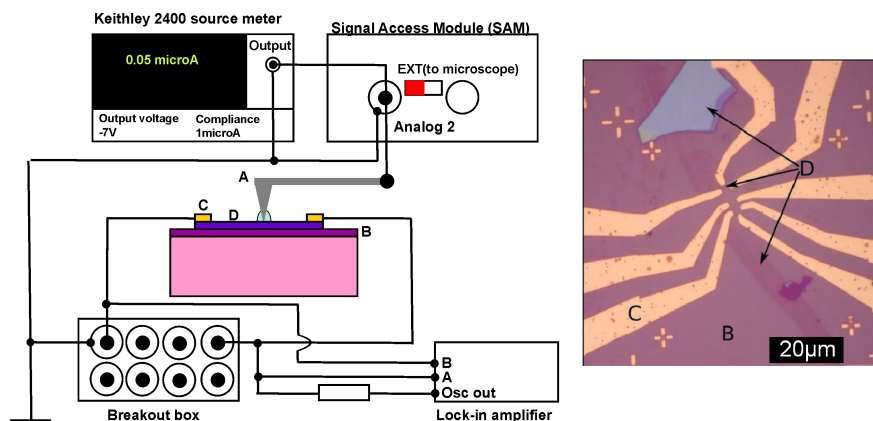
Figure 3.3: Left: Electrical setup for scanning probe lithography. The tip voltage is applied through a Signal Access Module using a sourcemeter. The oxidation current flowing between tip (A) and the grounded graphene flake (D), is limited to 1 μA in order to avoid accidental damage to the flake. The resistance of the graphene flake can be monitored in-situ through a breakout-box by connecting a lock-in amplifier to the sample contacts (C). Right: Optical image of a graphene device used for scanning probe lithography. Several thinner and thicker graphene flakes are placed on top of an oxidized silicon wafer (B) (oxide thickness typically 300 nm). The flakes are connected through Ti/Au-contacts, allowing the flakes to be set to ground with respect to the AFM tip. (*Sample courtesy of Rui Yang, University of Manchester.*)

by scanning over the flake with a low negative voltage applied between the SPM tip and the grounded sample.

3.3 Fabrication of nanometre-sized structures on graphene

3.3.1 TiN-coated tips

For the first attempts to perform local anodic oxidation experiments, we used AFM tips coated with TiN. These are conductive tips, and hence should be suitable for AFM lithography. Using these tips, we were able to etch lines in thin graphite and few-layer graphene with a tip bias ranging from -10 V to -20 V with respect to the grounded sample. The relative humidity was in the range of 50-60%.

Two typical lines etched with TiN-coated tips in a thin graphite sample under above conditions are shown in Fig. 3.4. As an example, the second line shown
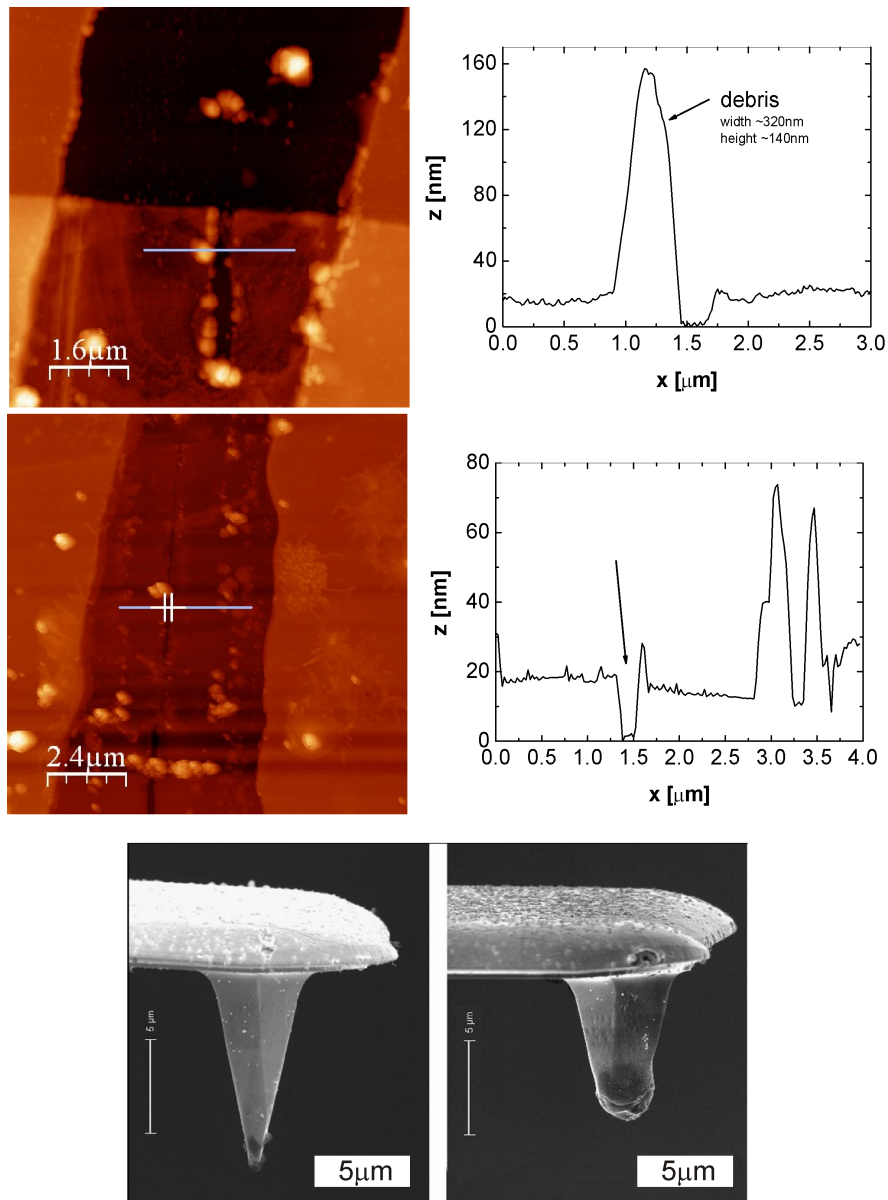
Figure 3.4: Top part: Two examples of lines oxidised in thin graphite with TiN-coated tips. Both lines show an irregular shape. The corresponding line profiles for each contact-mode AFM image are shown on the right. They indicate that both lines are around 200 nm wide and up to 20 nm deep. Material is scattered around the etched areas (high particles). The SEM images, shown in the bottom part, confirm that the TiN-coated tips get worn out strongly when used for AFM-etching of few-layer graphite. The left image shows a nearly new tip (rather sharp), whereas in the right a heavily used one is shown. It is very blunt, and the conductive coating was ablated.

was etched with a tip bias of -10 V under a relative humidity of 58%. The tip velocity used was 2 μm/s. To characterize the etched lines, line profiles were taken perpendicular to the cut. They are shown in the top part of Fig. 3.4, on the right side of the corresponding contact mode AFM images. One can see that the etched lines are around 200 nm wide, 15-20 nm deep and irregular in shape. No linewidths narrower than that could be achieved using TiN-coated tips.

Additionally to etching away graphite, mounds (seen as white spots on the AFM-images) appeared around the area were SPL was performed. Most probably these mounds are material from the tip that was ablated when performing the etching, since the TiN-coated tips got strongly consumed during local oxidation. This is clearly seen on SEM-images, shown in the bottom part of Fig. 3.4, were both a nearly new tip as well as one used for a couple of etchings are shown. The used tip, shown on the right, is both much shorter and much more blunt when compared to the nearly new one shown on the left. While for a new TiN-coated tip an etching voltage of -10 V or less was sufficient to achieve etching, higher voltages had to be applied to oxidize the graphene after each further oxidation cycle. Usually, after ten oxidation cycles no more oxidation was possible and the tip had to be replaced.

During the etching process, currents of about 100 nA flowing between the AFM tip and the sample have been observed. On the other hand, scanning the same area of the graphene flake for minutes without applying a bias voltage did not lead to any removal of graphene or appearance of mounds. That clearly indicates that the lines were etched with local anodic oxidation.

3.3.2 Silicon tips

The lithographic resolution of 200 nm obtained with TiN-coated AFM tips was not good enough to create graphene nanostructures of the required sizes of around 30 nm. Hence we investigated the performance of highly doped silicon AFM tips in our local anodic oxidation experiments.

Lithographic resolution

Operating the AFM in contact mode, we achieved successful local anodic oxidation when a tip voltage of -7 V was applied to the silicon tips at a relative humidity of 70%. The tip was scanned along the chosen directions with a probe velocity ranging from 200 nm/s up to 1 μm/s. Higher scanning speeds led to irregular line shapes or even complete suppression of oxidation. The spring force acting on the tip was set close to zero. This condition was found to yield the most reliable oxidation while achieving the thinnest line widths. Under these conditions, an oxidation current flowing between the AFM tip and the grounded graphene flake of 10-100 nA could be measured at the source meter.

For a relative humidity of 70% we found that for the given probe velocity, the line widths increased approximately linearly with applying a higher negative potential to the AFM tip. The dependence of the width of the oxidized lines as function of bias voltage applied to the AFM tip is shown in Fig. 3.5. For tip
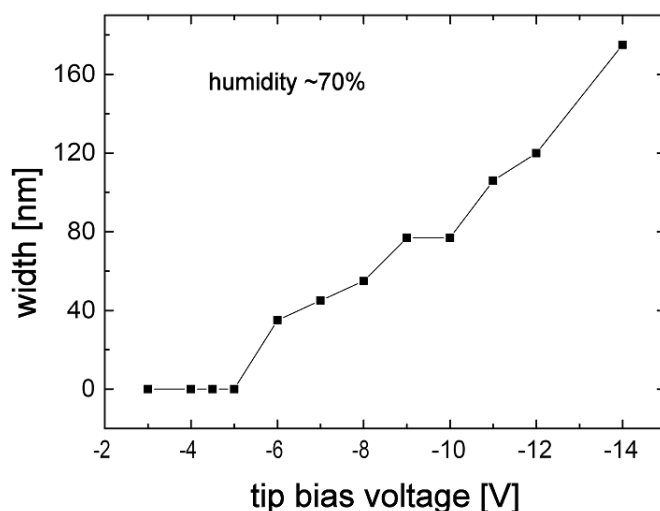
Figure 3.5: Dependence of the linewidth on applied AFM-tip bias voltage. The width of the etched lines increases approximately linearly with more negative bias voltages. Redrawn from [45].

voltages less negative than -5 V, no oxidation was observed at all. Typically, tip voltages of -7 V were found to yield the best results in terms of reliability and achieving narrow line widths. For the relative humidity lower than 60%, higher negative tip voltages, often in excess of -20 V, were needed to start oxidation. On the other hand, for relative humidities higher than 80%, no oxidation was found to occur. In this case, the oxidation current flowing between tip and sample

reached the set current limit of 1 μA.

An example of lines oxidized with silicon tips is shown in the upper part of Fig. 3.6. On the top left, several lines can be seen, which were oxidized by applying
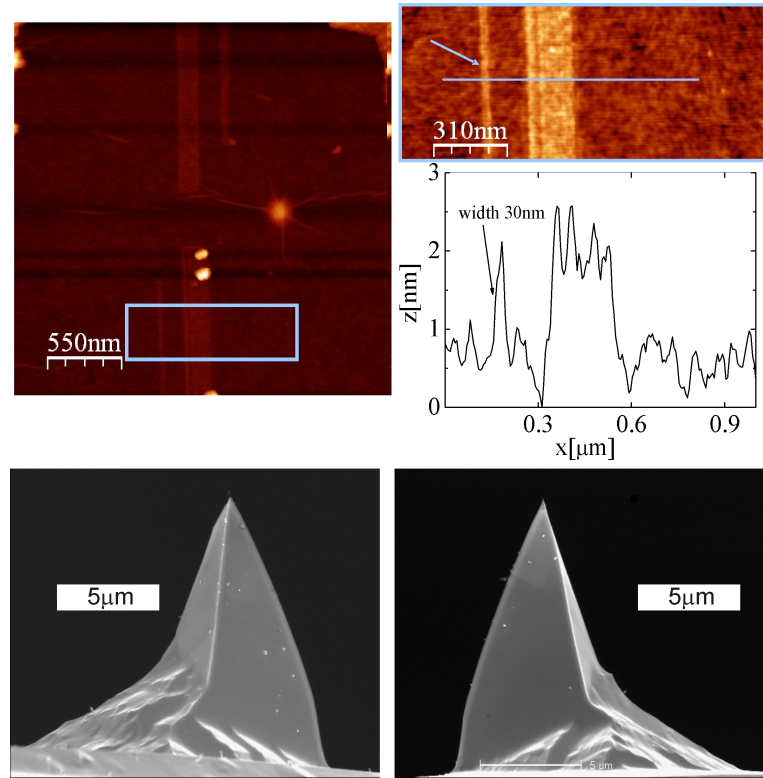
Figure 3.6: Top part: Left: Several lines oxidized in graphene (tip bias -7 V, relative humidty 65-80%, tip velocity 1 μm/s). Note that all lines appear as protrusions. Right: In the upper part, a magnified image of the region on the left indicated by the blue box is displayed, showing two straight lines oxidized in graphene. The bottom part shows an AFM line profile taken perpendicular to the oxidized lines (blue line in the upper image), indicating that the thinnest line (left) only has a width of 30 nm. Bottom part: The left shows an SEM image of a silicon tip that was used for oxidizing graphene. On the right, the SEM image of a new silicon tip is shown for comparison. No significant wear of the used tip can be seen.

a voltage of V=-7 V to the silicon tip with respect to the grounded graphene flake in an atmosphere with the relative humidity between 65% and 80% and a probe velocity of 1 μm/s. The upper image on the right shows a magnified view of two of the lines, as indicated by the box on the left. The thinnest line (left) is only 30 nm wide, as shown by the line profile (corresponding to the blue line in the upper image) below this image. It is worth mentioning that this particular line

appears as a protrusion. Additionally, in the large scale AFM image shown in the top left, no debris is observed. SEM images of silicon tips used for anodic oxidation are shown in the bottom part of Fig. 3.6. On the bottom left, a silicon tip that was used for local anodic oxidation is shown. On the right, a new AFM tip is shown for comparison. In contrast to TiN coated tips (Fig. 3.4), the silicon tips remained intact even after several oxidation cycles.

Chemical nature of oxidized graphene

In general, we have found that the oxidized areas when imaged in contact mode AFM sometimes appeared as protrusions and sometimes as depressions, depending on the scan direction. This observation can be related to the influence of frictional forces on the contact AFM imaging process. Hence the question whether we created a stable graphitic oxide, or whether we etched away the graphene completely cannot be answered from contact AFM images alone.

However, performing local anodic oxidation under identical conditions (same humidity, bias voltage, tip velocity) results in a similar height (within experimental error) of the measured protrusions or depressions found for the respective oxidation conditions. To further investigate this question, we have imaged lines oxidized in graphene (oxidation conditions: tip bias -7 V to -9 V, relative humidity 60% - 80%, tip velocities 200 nm/s - 1.2μm/s) by both contact mode AFM and TappingMode AFM. The results are shown in Fig. 3.7. While in contact AFM imaging (top panel, image on the left, indicated line profile on the right) all four lines, labelled A, B, C, D, appear as protrusions, in Tapping Mode AFM-imaging the broadest line (A) appears as depression containing some debris, while the lines labelled B, C and D still appear as protrusions. The different behaviour for line A is due to the different oxidation conditions, under which this line was oxidized.

Whereas the lines B, C and D are only 80 nm wide (equal to a single scan of the AFM tip), for line A an area of about 450 nm (equal to multiple scans) was oxidized. Apparently, the time for which the area corresponding to line A was exposed to the AFM tip voltage is much greater than that for lines B, C and D. The result of mostly etching away graphene (indicated by the solid arrow) for area A is in line with our observations that prolonged exposure to the tip voltage leads to the eventual removal of graphene. The debris in area A, which appears as protrusions, is formed from residual pieces of oxidised graphene (dashed arrows).
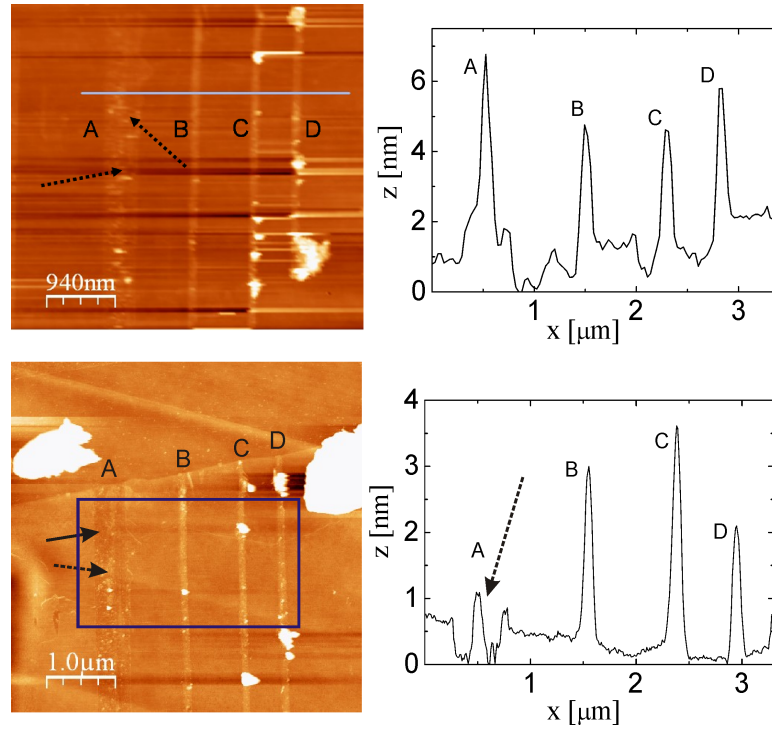
Figure 3.7: Top: On the left, a contact mode AFM image showing four different lines (labelled A, B, C and D) oxidized on graphene is displayed. The dashed arrows indicate inhomogeneous areas on line A, but which are not well resolved in contact mode AFM. The corresponding line profile (solid line in the image) on the right indicates all of the lines as being protrusions. Bottom: Tapping Mode AFM image of the same four oxidized lines as shown in the top panel. The improved lateral resolution allows distinguishing areas for line A where graphene was etched away (solid arrow) and where residual pieces of oxidised graphene remained (dashed arrows). The line profile on the right (averaged over the area indicated by the blue square in the image on the left) shows that the broadest line (A) appears as depression, but still shows spikes originating from residual oxidised graphene (dashed arrow). All other three lines (B, C, D) appear as protrusions.

Scanning area A in contact mode gives rise to the appearance of a protrusion, because of these residual oxidised graphene pieces. The lateral resolution in contact mode AFM is affected by lateral forces, and hence this area appears as protrusion. In Tapping Mode AFM, the lateral resolution is less affected by lateral forces, and so both the areas where graphene was etched away and the single residual oxidised graphene pieces are better resolved. In the corresponding line profile, which was averaged over an area indicated by a blue square in the Tapping Mode AFM image on the left, the latter appear as spikes (dashed arrow), whereas the etched areas appear as depression.

Although these results clearly confirm the chemical alteration of graphene by local anodic oxidation, they still don't allow for a clear assignment of the chemical composition of the oxidized areas appearing as protrusions. Ideally, the oxidation of graphite should lead to gaseous products, leaving a fully etched area as is observed in our case, when using a prolonged expsoure of graphene to the tip voltage.

To understand the chemical nature of the protrusions, one has to consider that the experimental scheme used for local anodic oxidation resembles that of an electrochemical cell. In Ref. [48], the electrochemical oxidation of the graphite (HOPG) surface in a low concentration sulfuric acid solution was investigated. In this paper, the authors also report the formation of protrusions (about 1 nm high) during the initial stage of electrochemical oxidation of HOPG. They conducted x-ray photoelectron spectroscopy (XPS) experiments, which showed clear signatures of C-O bonds having formed on the HOPG surface after the electrochemical treatment. Their suggestion is that the hydrolysis reaction, which leads to the formation of functional groups, such as alcohols, can be considered as the initiation reaction for the electrochemical oxidation of HOPG.

The oxidized areas appearing as protrusions which we observe could thus possibly consist of this metastable graphitic oxide, containing carbonyl and carboxyl groups, or could simply be made out of hydrocarbons, which are present in the air surrounding the water meniscus of the AFM tip. Hydrocarbons might also be present as contaminations adsorbed on the pristine graphene crystal. In the same way, other adsorbates, such as nitrogen or oxygen, present on pristine graphene [29] might also contribute to the formation of the protrusions formed during local anodic oxidation.

Element specific analysis, such as X-ray photoelectron spectroscopy (XPS) (as mentioned above) can unfortunately not be conducted on these protrusions, since their area is far to small to lead to an appreciable signal representing the protrusions alone. One way though would be the use of a conductive AFM technique, the so-called scanning spreading resistance microscopy (SSRM). In this technique one measures the current flowing between AFM tip and sample when a bias voltage is applied between AFM tip and the oxidized graphene sample. The bias voltage applied should be smaller than what is used for local anodic oxidation. From the resultant resistance of the areas containing the protrusions, one could confirm whether they are all identical, and would hence point to the

existence of specific material formed. If this should be the case, the resistances could be compared to what is reported in literature for materials that are likely to be formed, such as graphitic oxide mentioned above.

Confining graphene to nanometre sizes

Having established the working parameters for AFM-based lithography of graphene, we focus on oxidizing nanometre-sized structures that could operate as nanoelectronic devices. Electronic transport measurements of structures created by local anodic oxidation will be discussed in the following two chapters.

An example of a graphene quantum point contact created by AFM-lithography is shown in Fig. 3.8. On the left side, a contact mode AFM image is shown. It
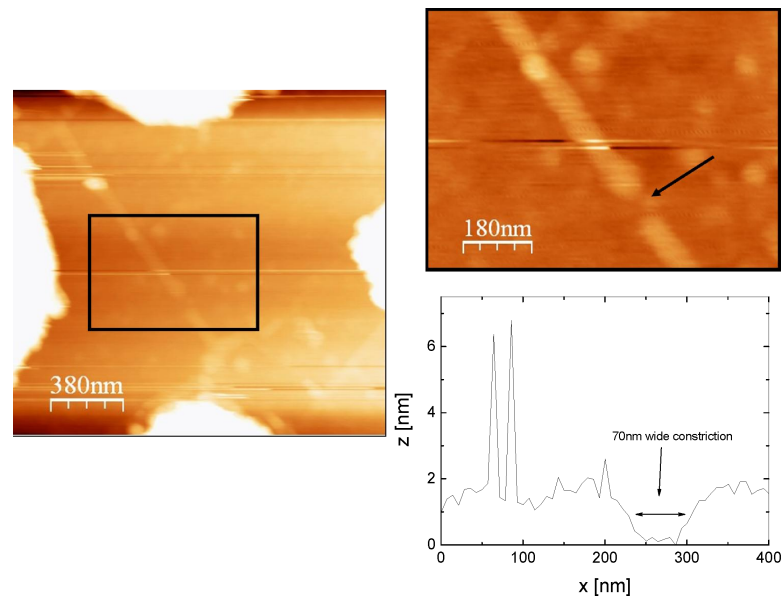
Figure 3.8: Left: Contact AFM image of a graphene flake equipped with gold contacts (white areas in the middle of the four image edges), on which a quantum point contact was formed (area inside the black box). Right: The upper part shows a magnified image of the area marked with the black box. The quantum point contact was made oxidizing a straight line on the flake, only interrupted by a small gap. This gap is about 70 nm wide, as is shown in the line profile in the bottom part.

shows a single layer graphene flake with four Ti/Au contacts (seen in the middle of each edge, white colour). A straight white line runs diagonal through the image, which is interrupted by a small gap. That gapped region is marked with a black box. The upper part on the right side of Fig. 3.8 shows a magnified image

of the area enclosed by the black box. The structure shown can be regarded as a graphene quantum point contact. It was formed by oxidising a constriction, i.e. separating the graphene flake into two independent parts by leaving only a thin conducting connection between them.

To oxidize a quantum point contact in graphene using SPL, we first oxidised a straight line, interrupted with a small gap (the gap is an area where no oxidation took place, such to leave the graphene unperturbed). For the quantum point contact shown in the right part of Fig. 3.8, we used a tip voltage of V_{ox}=-7 V, a scan size of 1.5 μm and a probe velocity of 0.3 μm/s. The temperature was 21°C, and the oxidation was carried out at a relative humidity of 78%. The gap in the oxidized line was formed by applying a positive voltage pulse of +1 V (setting the voltage to 0V didn't result in gap formation) for 0.5 s in between two voltage pulses of -7 V. The total exposure time for the three voltage pulses was adjusted such, that the probe only scanned the required line once (i.e. it only completed one pass, either trace or retrace). For the values mentioned, the oxidized line was interrupted by a gap of 170 nm width. Because we didn't see any effect on the electronic transport properties for this size of the constriction, the gap was further narrowed with oxidizing a series of dots, using a tip voltage of -6 V for 5 s while keeping the tip at a fixed position. Finally, we ended up with a gap of about 70 nm width, as can be inferred from the line profile taken across the gap, which is shown in the bottom part on the right side of Fig. 3.8.

A second example of a quantum point contact etched in graphene using AFM-lithography is shown in Fig. 3.9. The left part of the image shows a contact mode AFM overview image of the structure, fabricated with a tip bias of -7 V, relative humidity of 60-70% and probe velocities between 0.2-0.7 μm/s. In the top part of that image, a V-shaped line oxidized in graphene can be seen. This line is a cut in graphene and serves to electrically insulate a contact from the remaining part of the flake. The region separated by the oxidised line, which can be used as a sidegate, is indicated by SG. Next to the sidegate, a narrow graphene constriction (60 nm×60 nm in size) was fabricated that essentially forms a graphene quantum point contact. A black arrow points to the graphene constriction, which is also shown in larger magnification in the center of the top image on the right part of of Fig. 3.9. The line profile in the lower right part of Fig. 3.9 was taken perpendicular to the etched diagonal line, and clearly shows the step-height of
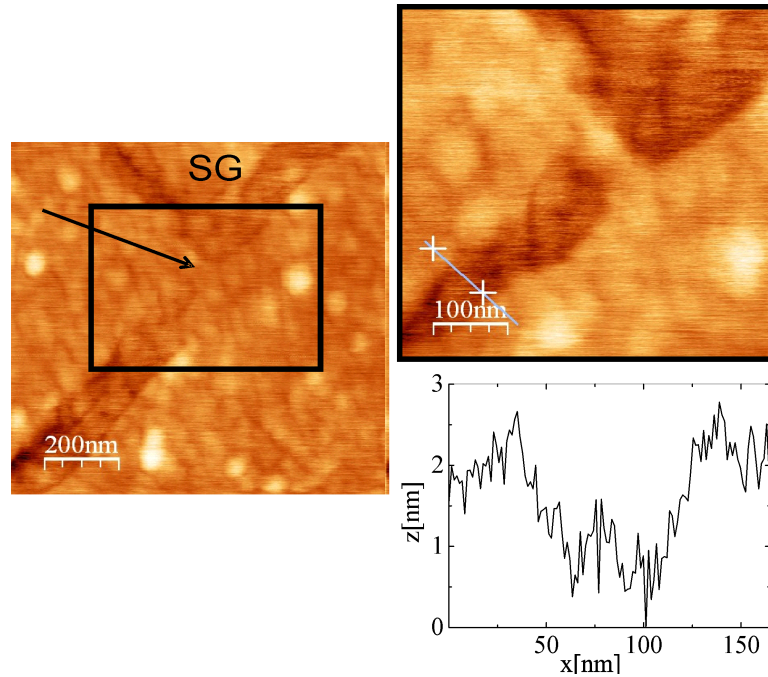
Figure 3.9: Left: Contact mode AFM image showing a quantum point contact (black arrow) with adjacent sidegate (top part, labelled SG) formed in single layer graphene by scanning probe lithography. The sidegate consists of a contact that has been electrically isolated from the remaining graphene flake by etching a V-shaped line around it. Oxidation was carried out at -7 V tip bias, a relative humidity of 60-70% and probe velocities ranging from 0.2-0.7 μm/s. Right: On top, a magnified image of the quantum point contact, marked in the left image with a black box, is shown. The quantum point contact is a region of intact graphene with a size of about 60 nm$\times$60 nm. On the bottom, an AFM line profile perpendicular to the etched line that forms the quantum point contact is displayed, indicating a stepheight of the cut of around 0.8-1 nm, the stepheight of single layer graphene (as discussed before). This is an example of an area oxidized on graphene appearing as a depression, i.e. indicating that graphene got etched away completely.

single layer graphene as measured by AFM, i.e. a step-height of around 0.8 nm.

3.3.3 Conclusions

In conclusion, we have shown how to create graphene nanostructures using AFM-based local anodic oxidation. It was shown that this approach yields a resolution better than 30 nm and is capable of producing structures that could be used as nanoelectronic devices.

Electronic transport measurements, which also demonstrate the insulating behavior of the oxidized lines, will be presented in the next two chapters. Out of

five graphene devices, we were able to create three nanostructures, with two of them working at low temperatures.

While we have clear evidence that graphene is chemically altered, the chemical nature of the structures oxidised in graphene by this scanning probe lithography technique can yet not be clearly assigned.

Chapter 4

Graphene-based nanoelectronic devices

Many of the unusual and fascinating properties of graphene are attributed to the linear and gapless band structure of this two-dimensional material. On the other hand, many applications, e.g. in the field of micro-and nanoelectronic devices, require the presence of a band gap. A feasible strategy to create a band gap in graphene is to confine it to nanometer sizes. Investigations on so called graphene nanoribbons (GNRs), nanometer wide and micrometer long strips of graphene, have shown that indeed an energy gap can be opened in graphene due to size confinement [33]. Confining graphene to nanometer sizes is usually done by removing unwanted material from a graphene crystal by etching in a reactive plasma (e.g. in an oxygen plasma).

Another structure that can be achieved by confining graphene to nanometer sizes are quantum dots made from graphene [34, 35]. Quantum dots can be seen as confined islands of a conductor or semiconductor, which are coupled to source and drain electrodes by highly resistive barriers and to a backgate. A schematic picture depicting this situation is given in Fig. 4.1.

In this chapter, I will first give an introduction to quantum dots by explaining the fundamentals of charge carrier transport in these structures. In the second part, I will present an example of a graphene quantum dot fabricated using AFM lithography. The results of measuring electronic transport through a graphene quantum dot defined by this technique are presented and discussed in the third part. Finally, I will conclude with summarizing our main achievements and giving an outlook to where this work might eventually lead.

a

lateral quantum dot

SOURCE   DRAIN

GATE

V_{SD} V_g I
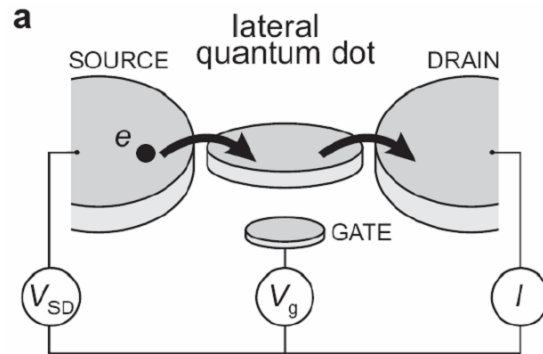
Figure 4.1: Schematic of a quantum dot, in the shape of a disk, connected to source and drain contacts by tunnel junctions and to a gate by a capacitor. The current I through the device, emanating from electrons tunneling on and off the dot, is measured as a function of bias voltage V_{SD} between source and drain electrode and of gate voltage V_g. Taken from [49]

The main results of this chapter have been published in [45].

4.1   Introduction to quantum dots

Quantum dots are the main building block of a class of nanoelectronic devices known as single electron transistors. They are particularly interesting as possible candidates for the operation as switching elements in future very large scale integration circuits. Their main importance lies in their behavior with respect to how they conduct electric current. However, a relatively common problem with quantum dots based on conventional materials used in the semiconductor industry is that they only show single electron switching behaviour at temperatures far below room temperature. To operate at room temperature, quantum dots have to be made very small. However, at the nanometre sizes required, materials like Silicon are likely to encounter fundamental limitations, according to the semiconductor industry roadmap [3]. Contrary to this, it was recently shown [34] that quantum dots made from graphene can still operate as single electron transistors even at room temperature.

4.1.1 Electron transport through quantum dots

A quantum dot is a small conducting island, which is weakly coupled to charge reservoirs (source and drain electrodes). In equilibrium, an integer number of electrons are localized on the dot. If one now adds one more electron to the dot, the charge on the dot is increased by e. The resulting change in the Coulomb energy of the dot is e^2/C, where C is the total capacitance of the island. Should the energy of an electron from the reservoirs be smaller than e^2/C, this electron can't tunnel onto the dot. In order to occupy the dot, it has to have an energy larger than the electrostatic energy of the dot. This phenomenon is therefore called Coulomb blockade. In effect, an energy gap of size e^2/C, called the charging energy, separates the highest occupied energy level of electrons in the dot from the lowest unoccupied energy levels.

In order to observe Coulomb blockade in electronic transport measurements through a quantum dot, two conditions have to be met.

- The charging energy of the dot must be much larger than the thermal energy:

$$E_C = \frac{e^2}{C_{dot}} \gg k_B T \tag{4.1}$$

  The capacitance of the dot, C_{dot}, which sets the charging energy, is defined by the geometry of the device as well as by the distance to source, drain and gate contacts. Hence, making a quantum dot small enough might eventually enable the observation of Coulomb blockade at a given temperature.

- The tunnelling barriers that weakly couple the dot to both source and drain electrodes, have to be sufficiently opaque. The observation of Coulomb blockade relies on the fact that the number of electrons on the dot is fixed at a given integer value. Thus, the electrons have to be located in either the source or drain reservoirs or on the dot, such that no fluctuations in the number of electrons on the dot occur over the time span of a typical measurement.

  Taking the typical time to charge or discharge the island, $\Delta t = R_{barrier} C_{dot}$, and the Heisenberg uncertainty relation: $\Delta E \Delta t = (e^2/C_{dot}) R_{barrier} C_{dot}$, we obtain that the tunnelling resistance of the barriers need to be much larger

than the resistance quantum h/e^2=25.813kΩ.

$$R_{barrier} \gg h/e^2 \qquad (4.2)$$

Weakly coupling the dot to source and drain electrodes can be achieved by using narrow constrictions that are usually referred to as quantum point contacts (QPCs). But there exists also an upper limit on the barrier resistance, such to allow at all for conducting transport measurements. The optimal value for $R_{barrier}$ is around 100kΩ when applying lock-in measurements to characterize the electronic transport properties of the quantum dot.

A common way to overcome Coulomb blockade is by applying a gate voltage to the dot. This voltage changes the electrostatic energy of the dot. Once the charging energy has been overcome, a single electron can tunnel on the dot. This process of charging an electrode one at a time is called single electron charging. It is described in more detail below.

An important addition to the model just described is the existence of quantum mechanical energy levels inside the quantum dot. If the dots are small enough, these energy levels arise because of the quantum mechanical nature of electrons, and the energy spacing between subsequent levels increases when the quantum dots are made smaller. When electrons are confined to small sizes, they behave according to the quantum mechanical model of a small particle confined inside a potential well ("particle in a box"). The resulting single-particle energy level spacing $\Delta E = E_N - E_{N-1}$ has to be added to the charging energy to properly describe the energy barrier an electron faces when attempting to tunnel on the dot. Aside from the geometric dimensions, material parameters can influence the intrinsic energy level spacing as well.

4.1.2   Theory of Coulomb blockade

To understand charge carrier transport through quantum dots for the device configuration shown in Fig. 4.1, I will follow the theory as described in Ref. [50,49].

The potential landscape of a quantum dot is shown in the top part of Fig. 4.2. An equivalent circuit diagram can be constructed, which is shown in Fig. 4.3. Given that the resistance of the tunnel barriers between source and drain electrodes and the dot are high enough, an integer number of electrons residues in
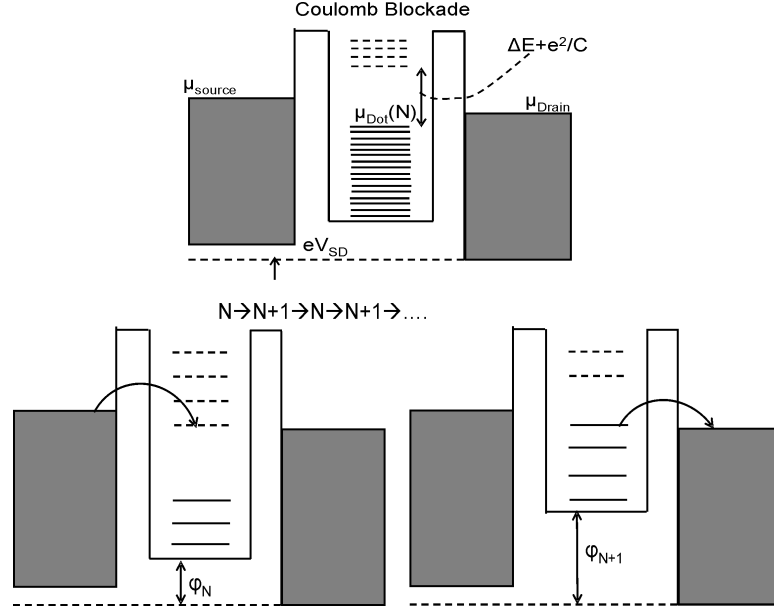
Figure 4.2: Potential landscape through a quantum dot. The states in both source and drain electrode are filled up to the electrochemical potentials μ_{source} and μ_{drain} which are related via the bias voltage $V_s d = (\mu_{source}-\mu_{drain})/e$. The discrete states in the quantum dot are filled with N electrons up to $\mu_{dot}(N)$. The addition of one electron to the dot would raise $\mu_{Dot}(N)$ (the highest solid line) to $\mu_{dot}(N+1)$, the lowest dashed line. In the top part of the image, this addition is blocked at sufficiently low temperature $(k_B T << \Delta E + e^2/C)$. By changing the gate voltage applied to the dot, the highest unoccupied energy level of the dot, $\mu_{dot}(N+1)$, is aligned in a window between μ_{source} and μ_{drain}. Now to addition of an electron to the dot is allowed. The lower two images illustrate the sequential tunneling process that now takes place. In the lower left, an electron from the source occupies the dot state with energy $\mu_{dot}(N+1)$. Now, N+1 electrons occupy the dot. In the lower right picture, this electron tunnels off to the source electrode, leaving the dot with N electrons on it. After [49]

the dot. The electrostatic energy of the dot can be written as:

$$E_{el-stat} = \frac{(-en + Q_0)^2}{2C} \tag{4.3}$$

with: $n = N - N_0$, $Q_0 = C_{source}V_{source} + C_{drain}V_{drain} + C_{gate}V_{gate}$ and $C = C_{source} + C_{drain} + C_{gate}$. The integer part of the excess charge in the dot is $en = e(N - N_0)$, with N being the number of electrons in the dot, and the elementary charge e (taken positive). N_0 is the number of electrons at zero gate voltage and zero bias voltage (i.e. source-drain voltage), which might arise due to doping. Q_0 represents the continuous part of the excess charge on the dot, which is induced on the dot by the voltage differences V_{source} and V_{drain} between the

71
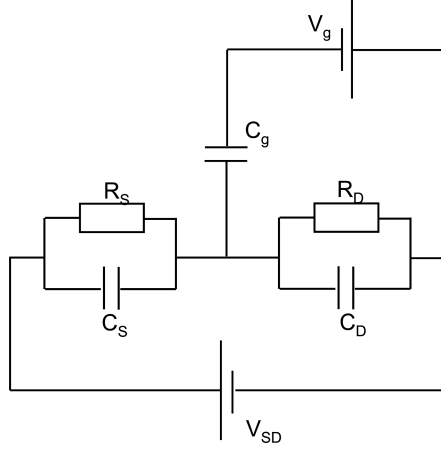
Figure 4.3: Equivalent circuit diagram of the configuration shown in Fig. 4.1

dot and the leads, and by the gate voltage. C is the total capacitance of the dot with respect to ground, which consists of the capacitances between the dot and the leads (C_{source} and C_{drain}), and the capacitance between dot and gate (C_{gate}).

To measure electronic transport through the dot, we apply a small bias voltage, $V_{sd} = (\mu_{Source} - \mu_{Drain})/e$, across the dot as the gate voltage is varied. Then the continuous part of the excess charge on the dot becomes $Q_0 = C_g V_g$, where V_g stands for the gate voltage which is varied, and C_g denotes the capacitance between gate and the dot. The ground state energy for N electrons in the dot at zero temperature is the sum over the single particle energies relative to the bottom of the conduction band, and the electrostatic energy of the dot:

$$U(N) = \sum_{p=1}^{N} E_p + \frac{(-en + C_g V_g)^2}{2C}. \tag{4.4}$$

From Eq. 4.4 we can calculate the electrochemical potential which by definition is the minimum energy necessary to add the Nth electron to the dot: $\mu_d(N) = U(N) - U(N-1)$,

$$\mu_d(N) = E_N + \frac{(n - 1/2)e^2}{C} - e\frac{C_g}{C}V_g. \tag{4.5}$$

This can be written as $\mu_d(N) = \mu_{ch}(N) + e\phi_N$. The electrochemical potential is the sum of the chemical potential $\mu_{ch}(N) = E_N$ and the electrostatic potential $e\phi_N$. When the number of electrons on the dot is changed by one, the resulting

change in electrochemical potential at fixed gate voltage reads:

$$\mu_d(N+1) - \mu_d(N) = E_{N+1} - E_N + e^2/C. \tag{4.6}$$

Equation 4.6 implies that the electrochemical potential changes by a finite energy when an electron is added to the dot. $\mu_d(N+1) - \mu_d(N)$ is large for large energy splitting between consecutive quantum dot states, and/or for a small capacitance. This energy gap can lead to a blockade for tunnelling of electrons into and out of the dot, as is shown in the top part of Fig. 4.2. The $N+1$ electron can not tunnel into the dot, because the resulting electrochemical potential $\mu_d(N+1)$ is higher than the electrochemical potential of the reservoirs. In other words, current through the dot is zero in this case, since there is no available state on the dot in the energy window between μ_{source} and μ_{drain}. So for $\mu_d(N) < \mu_{source}, \mu_{drain} < \mu_d(N+1)$ the electron transport is blocked, which is known as the Coulomb blockade.

The Coulomb blockade can be eliminated by changing the gate voltage (or equivalently, the induced charge Q_0, so that $\mu_d(N+1)$ is lined up between μ_{source} and $\mu_{drain}[\mu_{source} > \mu_d(N+1) > \mu_{drain}]$. This is shown in the two images in the lower part of Fig. 4.2. Here, an electron can tunnel from the source electrode into the dot $[\mu_{source} > \mu_d(N+1)]$. The electrochemical potential in the dot increases by the amount given in 4.6, which for the depicted situation is dominated by $e\phi_{N+1} - e\phi_N = e^2/C$. Because $\mu_d(N+1) > \mu_{drain}$, one electron can tunnel out of the dot to the drain electrode on the right, causing the electrochemical potential to drop to $\mu_d(N)$. Now, an electron from the source electrode can again tunnel into the dot and repeat the cycle. This process, where current is carried by successive charging and discharging of the dot, is known as single charge tunnelling.

As the gate voltage is changed, the conductance of the quantum dot oscillates between zero (Coulomb blockade), and non-zero (no Coulomb blockade). These so called Coulomb oscillations are illustrated in Fig. 4.4. In the case of Coulomb blockade, where no current can flow through the dot, a conductance minimum is found. This situation corresponds to a fixed number of electrons in the dot. At a conductance maximum, this number oscillates by one electron. The period of the conductance oscillations can thus be determined using Eq. 4.5 and the condition $\mu_d(N, V_g) = \mu_d(N+1, V_g + \Delta V_g)$. For the period of the oscillations in gate voltage

73
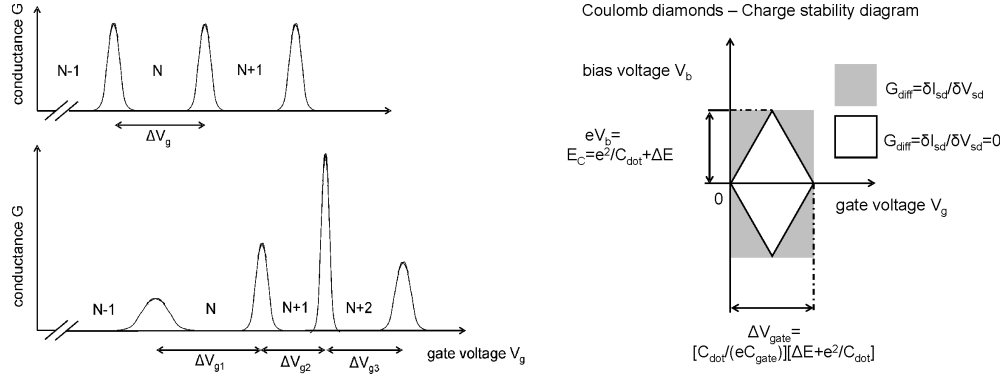
Figure 4.4: Left: The conductance through a quantum dot as a function of gate voltage at fixed source-drain voltage. In the upper part the situation for a vanishing energy splitting ΔE is shown. Here, all peaks are strictly periodic as a function of gate voltage, and their height is the same. In the bottom part, the same situation is depicted for quantum dots with a non-vanishing energy splitting. The conductance peaks are no longer periodic and the peak height is no longer constant. Right: Schematic model of the charge stability diagram of a quantum dot. It is obtained when measuring the differential conductance, i.e. the change of source-drain current as the bias voltage between source and drain is varied, at a fixed gate voltage for a series of gate voltages. Inside the Coulomb diamond (white), electronic transport through the dot is blocked (Coulomb blockade), and hence the conductance is zero. Outside the diamond (grey area), Coulomb blockade is overcome, and a current can flow through the dot.

ΔV_g corresponding to a change of one electron, we get:

$$\Delta V_g = \frac{C}{C_g}\left(\frac{E_{N+1} - E_N}{e}\right) + \frac{e}{C_g}. \tag{4.7}$$

For vanishing energy splitting $E_{N+1} - E_N = 0$, the classical capacitance-voltage relation for a single electron charge $\Delta V_g = e/C_g$ is obtained. This situation reflects in periodic conductance peaks as a function of voltage, and is shown in the upper part on the left of Fig. 4.4. A non-vanishing energy splitting results in aperiodic oscillations, as shown in the diagram underneath.

Another way to lift the Coulomb blockade is given by changing the bias voltage that is applied between source and drain electrode. Measuring the differential conductance through a quantum dot as a function of varying bias voltage at fixed gate voltages for a large range of gate voltages, one obtains the so called charge stability diagram. This is schematically shown on the right part of Fig. 4.4. The regions in which Coulomb blockade occurs, and hence no current flows through the dot, is indicated by a white diamond that is called Coulomb diamond. It corresponds to the conductance minima shown on the left, where the dot carries

74

a fixed number of electrons. Here, the number of electrons on the dot is stable. Outside the diamond (grey areas), the conductance is non-zero, corresponding to the conductance peaks in the left part of that image, there shown for a fixed bias voltage.

As outlined above, the size of a Coulomb diamond in gate voltage around zero bias voltage equals the distance between two adjacent conductance peaks. This distance, as shown in the scheme, is determined by the charging energy of the quantum dot and the spacing between the two successive energy levels in the quantum dot. On the other hand, from the height of the Coulomb diamonds in the direction of the bias voltage, the energy required to add one additional electron to the dot can be directly determined: $eV_{bias} = e^2/C_{dot} + \Delta E$. In the case of vanishing splitting between the energy levels, all Coulomb diamonds will have equal height ($eV_{bias} = e^2/C_{dot}$) and equal distance around zero bias voltage ($\Delta V_g = e/C_{dot}$). This can be observed in the case of classical Coulomb blockade.

Temperature dependence of conductance oscillations

In electronic transport measurements through quantum dots, three different temperature regimes can be distinguished:

1. $e^2/C \ll k_B T$. Here, the discreteness of charge cannot be resolved in transport measurements.

2. $\Delta E \ll k_B T \ll e^2/C_{dot}$. This is the so called classical or metallic Coulomb blockade, where many single-particle energy levels of the dot are thermally excited. The conductance through the dot is only affected by the charging energy e^2/C_{dot}.

3. $k_B T \ll \Delta E < e^2/C$. This is the quantum Coulomb blockade regime. Here, only one or a few of the quantum mechanical energy levels of the dot participate in transport. The energy level spacing ΔE becomes important.

In the classical Coulomb blockade regime, the conductance maxima are independent of temperature and Coulomb oscillations are visible for temperatures up to $k_B T < 0.3 e^2/C_{dot}$ [49].

In the quantum Coulomb blockade regime, electronic transport occurs through a single quantum mechanical energy level of the dot. One would expect a monotonic increase in peak height as the temperature is reduced. Generally, for temperatures close to the energy level spacing ΔE inside the dot, the charging energy should dominate the energy gap. This leads to relatively weak changes in the height of the conductance peaks, as opposed to the classical regime, where the peak height should stay constant. On decreasing the temperature further, upon entering the quantum regime ($k_B T \ll \Delta E$), the peak heights increase, with maximum peak heights at lowest temperatures. But experimentally, a slightly different situation was found. Meirav et al. [51] observed a non-monotonic behaviour of the conductance peaks. In their experiment, some peaks decreased with rising temperature at low temperatures and then increased again at a higher temperature. On the other hand they have found other peaks that do not show such a decrease at low temperatures. This observed random peak behaviour is usually due to the variations in the nature of the energy levels inside the quantum dot [49]. For different single-particle energy levels in the dot their coupling to the reservoirs might differ. This has been considered in the work of Meir et al. [52] in order to explain the unusual temperature dependence of the conductance peaks observed in the experiment of e.g. Meirav et al. [51]. Meir et al. modelled electronic transport through a single quantum dot, incorporating both the effect of Coulomb interaction and the energy level spacing between two single particle energy levels in the dot. In their model, they also accounted for a different coupling of these single-particle energy levels of the quantum dot to the charge reservoirs. As a result, they calculate that the conductance peak corresponding to the stronger coupled level shows a monotonic decrease as the temperature is increased. On the other hand, the conductance peak corresponding to the weaker coupled energy level of the quantum dot first decreases as temperature is increased. But as the temperature approaches the bare level spacing, $\Delta E \simeq k_B T$, the height of this conductance peak increases again. Meir et al. explain this behaviour by considering that at temperatures comparable to the energy level spacing the second energy level in the dot starts contributing to the conductance of the first peak. Because this second energy level has a stronger coupling to the reservoirs, an increase in conductance occurs. Extending their theory to multiple energy levels in the quantum dot, with different couplings to the reservoirs for each energy level, they were able to qualitatively reproduce experimental data shown within their

paper [52]. This model thus can be used to explain the temperature dependence of the conductance peaks in the regime of quantum Coulomb blockade.

On the other hand, from the temperature dependence of the conductance minima in the quantum Coulomb blockade regime one is able to determine the energy gap of the quantum dot. By considering two adjacent, discrete energy levels confined in a quantum dot, spaced by an amount of ΔE, the Fermi energy lies halfway between these two energy levels when a conductance minimum occurs. By calculating the conductance through the dot at the Fermi energy, one obtains the conductance minimum as a function of temperature [53].

If the temperature, at which the conductance through the quantum dot is measured, is much smaller than the energy gap of the quantum dot, i.e.

$$k_{\mathrm{B}}T \ll \Delta E + \frac{e^2}{C}, \tag{4.8}$$

the conductance minimum between two adjacent conductance peaks was found to show thermally activated behavior over some temperature range [53]:

$$G_{min} \propto exp(-E_{act}/k_B T). \tag{4.9}$$

In this expression, the activation energy equals half of the energy gap of the quantum dot, which is the sum of quantization energy plus charging energy:

$$E_{act} = \frac{1}{2}(\Delta E + e^2/C) \tag{4.10}$$

Accordingly, from plotting the natural logarithm of the value of the conductance minimum as a function of inverse temperature, the slope from the resulting linear function equals half the value of the energy gap.

4.2   Graphene quantum dots

It was demonstrated in the works of Ponomarenko et al. [34] and Stampfer et al. [35] that quantum dots from graphene can be made by etching graphene in a reactive oxygen plasma to obtain the desired geometric structure. An alternative route to remove unwanted material from graphene to create an island, which is

weakly coupled to source and drain electrodes, is given by scanning probe lithography. This approach consists of local electrochemical etching of graphene under the influence of a biased conductive AFM-tip in the presence of an etchant. The most common etchant for scanning probe lithography is water. In the previous chapter it was demonstrated how this approach is applied to locally cut and oxidise graphene. Following this procedure, we were successful in creating quantum dots in single layer graphene. Measurements of electronic transport through the quantum dot structures obtained revealed the existence of Coulomb blockade oscillations at low temperatures.

To start with the fabrication of a graphene-based quantum dot, graphene crystallites were prepared from natural graphite [54] on an oxidized Si substrate (300 nm of silicon oxide) by micromechanical cleavage [3, 1, 2]. Standard electron beam lithography and thin film deposition were then used to define electrical contacts, consisting of Ti and Au, on the graphene flake [1, 4]. Prior to further treatment by scanning probe lithography, the samples were annealed for 4 hours at 550K in hydrogen/argon atmosphere (10per cent hydrogen) to remove resist residues due to the lithography. Electrical measurements revealed an electron mobility of 13,000cm^2 (Vs)$^{-1}$ (measured at typical carrier concentrations of n = 10^{12} cm^{-2}). The single layer nature of the device was confirmed by optical microscopy and Raman spectroscopy [4, 55]. Topography scans reveal the height of our graphene samples to be typically about 0.8 nm above the SiO$_2$ surface, which is the standard value for monolayer graphene in AFM measurements.

The final fabrication of a quantum dot structure in the graphene sample was done using local electrochemical oxidation, as described in Chapter 3. The biased tip (V$_{tip}$=-7 V with respect to the grounded graphene sample) was scanned at a speed of about 200 nm/s along chosen lines across the graphene sample. The temperature was 22°C and the relative humidity was 70%.

Figure 4.5 shows an example of a quantum dot structure etched in graphene using local anodic oxidation. The left part of the image shows a contact mode AFM topography of our device. The bright lines appearing as protrusions, about 20 nm wide, were fabricated using scanning probe lithography. They confine the graphene crystal to a central island, labelled as quantum dot (QD), which
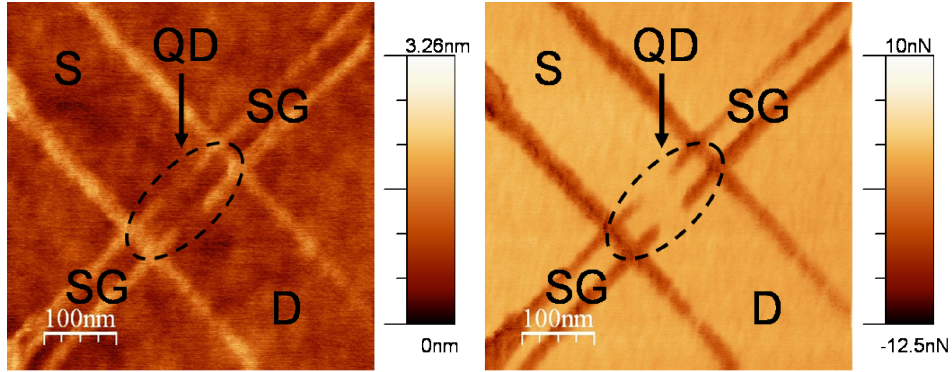
Figure 4.5: Example of a graphene QD structure created by local anodic oxidation. Contact-AFM height image shown in the left. The corresponding friction image is shown on the right. The bright regions in the right image are intact graphene, and dark lines the areas where graphene was etched away. The central island marked as the quantum dot (QD) is connected to the source (S) and the drain (D) electrodes via two narrow constrictions. Side gates (SG) are also formed from graphene. Taken from [45]

is connected to graphene source and drain electrodes (S,D) via two narrow constrictions. These constrictions (in the example shown about 40 nm wide), which can be referred to as quantum point contacts (QPCs), provide the barriers to decouple the quantum dot from the source and drain contacts. Sidegates were also formed from confining graphene by local anodic oxidation, indicated in the picture by SG. The right part of Fig. 4.5 shows a lateral force image obtained simultaneously with the topography. The dark regions in this image are the areas were graphene has been oxidized using local anodic oxidation, while the bright regions are intact graphene. The Si wafer was used as a global backgate.

4.2.1 Electronic transport through graphene quantum dots

The transport measurements of our quantum dot devices obtained by scanning probe lithography took place in a Wessington Cryogenics CH120 dewar, equipped with a He^3 system capable of cooling down to 300 mK. A SR830 lock-in amplifier (Stanford Research Systems) and several Keithley 2400 sourcemeters completed the set-up. We performed transport measurements on our quantum dot devices at various temperatures. The typical behavior of their conductivity is presented in Fig. 4.6 for a quantum dot similar to the one shown in Fig. 4.5 The conductivity shows the strongly distorted V-shape [34] behavior, and its value drops well below one conductivity quantum (e^2/h)in the voltage range between 33 V
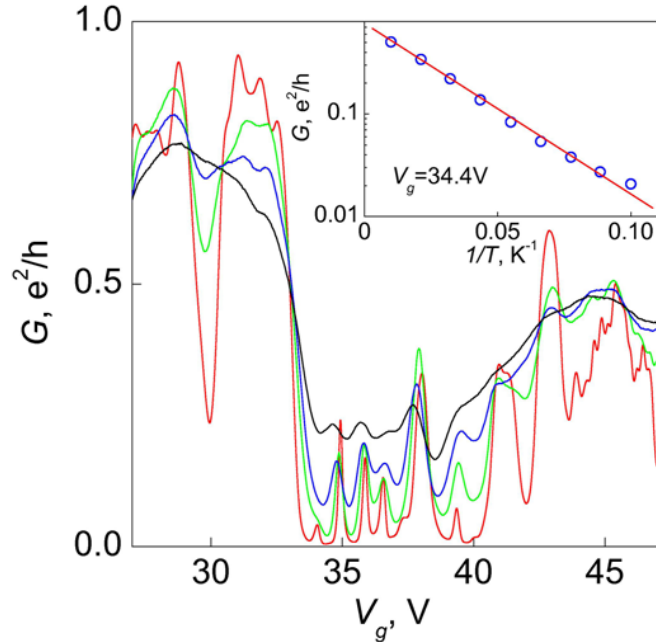
Figure 4.6: Conductivity through one of our QD devices (size of 100 nm) as a function of back-gate voltage for different temperatures. Red curve corresponds to 2.5 K; green curve to 10 K; blue curve to 20 K; black curve to 30 K. Inset: Temperature dependence of conductivity at a minimum between peaks (V_g=34.4 V). Taken from [45].

and 41 V. In this range several sharp conductivity peaks are observed. Outside this region the conductivity grows above $0.5e^2$/h, which we attribute to increased conductance through the constrictions (QPCs) between the QD and the S and D contacts, and the QD levels could not be resolved. The non-monotonic behavior of G in the region below 33 V and above 41 V is probably due to changes in the transmission through the QPCs [35]. One has to consider that the QPCs consist of nanometer-sized graphene ribbons (size on the order of 20 nm). It has been shown, that graphene confined to these geometries has energy states in the gap due to the irregular edge structure [33]. This might be one reason, why transmission through our constrictions might have changed.

The resonances in the voltage range between 33 V and 41 V are associated with the energy levels in the QD. The peaks are strongly aperiodic, which suggests that both the Coulomb energy and the size quantization energies are contributing to the splitting between the energy levels [49] (see bottom part of Fig. 4.4 for a schematic illustration of that situation). We observe that the number of peaks stays constant for T < 20 K. Also, the relatively weak temperature dependence

in the resonances (that can be as high as $0.5e^2/h$) indicates that only one QD is present [52]. In the case of two quantum dots or more in series, one would also expect a seemingly random peak spacing. But additionally one would also expect in that case some conductance peaks to be completely suppressed at low temperatures, while they should appear at higher temperatures, thus changing the number of peaks [56]. This is clearly not the case in our experiment. Furthermore we see that the peak height increases at lowest temperatures, as expected for Coulomb blockade in the quantum case [52]. As described above, from the temperature dependence of the minimum conductivity one can extract the activation energy, which is directly proportional to the energy gap $e^2/C_{dot} + \Delta E$ of the dot (the sum of charging energy and confinement energy). The corresponding fit to our data is shown in the inset in Fig. 4.6. Our activation energy corresponds to an energy gap of 6.5 meV, in agreement with the typical level spacing expected for a 100 nm QD ($\Delta E = \alpha/D$, where α varies around a value of 1 eV/nm by a factor of 2 in different models [57, 58]).

Similar values of the gap are obtained from the stability diagrams (conductivity versus the gate voltage and source-drain bias) such as in Fig. 4.7, which shows the standard Coulomb diamonds. The height of the diamonds directly yields the
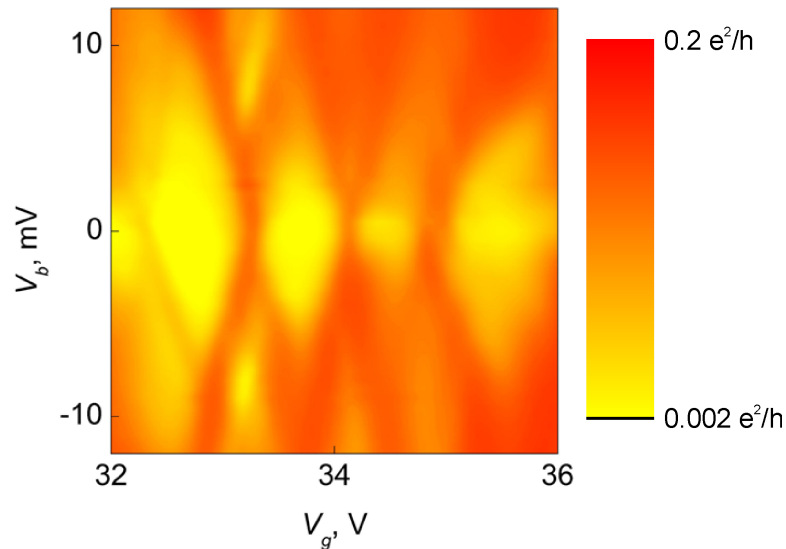
Figure 4.7: Coulomb diamonds for the QD in Fig. 4.6 as a function of the gate voltage (the horizontal axis) and the source-drain bias voltage (V_b, the vertical axis). T=2.5 K. The conductivity varies from 0.002 e^2/h (yellow) up to 0.2 e^2/h (red). Redrawn from [45].

distance between adjacent energy levels of the dot and for this particular sample

varies from 5 to 10 mV. This agrees well with the value of 6.5 meV obtained from the temperature dependence of the minimum conductance. The variation in height of the diamonds clearly shows that the size quantization contributes significantly to the formation of energy levels in our small quantum dots [49].

4.2.2 Conclusions and outlook

It was shown that graphene could be confined to a quantum dot geometry, consisting of a graphene island weakly coupled to graphene source and drain electrodes by two narrow constrictions, employing atomic force lithography. Using this technique, the constrictions can be made as small as 20 nm. This sets the lithographic resolution limit of our AFM-based technique. An example of a quantum dot consisting of a 100 nm×100 nm sized graphene island fabricated by AFM lithography was given. Electronic transport through a similarly sized device clearly reveals the presence of quantum Coulomb blockade phenomena in devices of that size. The contribution of individual quantum mechanical energy levels formed inside the graphene quantum dot can be directly obtained from the presented charge stability diagrams. Additionally, from the temperature dependence of the Coulomb blockade oscillations a behavior characteristic of quantum Coulomb blockade can be seen.

In principle, the lithographic resolution limit can be overcome using much sharper AFM tips. It has been shown [34] that the smallest quantum dots made from graphene show fascinating properties, both with respect to fundamental physics (behavior of Dirac fermions in confined geometries) as well as with respect to microelectronic applications (a single-electron transistor operationable at room temperature was demonstrated). The approach of using AFM lithography to create such small structures holds promise regarding ease of use (no cleanroom environment needed, much faster processing than electron beam lithography). Moreover, by using the sharpest tips available, the resolution limit of electron beam lithography of 5 nm (given by the size of an individual PMMA-molecule [34]) could be further reduced to about 2 nm, with keeping high reliability.

Another application of AFM-based lithography lies in its ability for local (nanometre sized) electrochemical modification of the substrate. One could think

of replacing water as the source of reactive ions by other chemicals. Thus, one might be able to chemically modify the graphene scaffold by grafting different functional groups originating from the electrolyte. This local chemical modification might similarly be employed to change the chemical nature of edges terminating graphene. One could hope for creation of electronically uniform edges, ideally mimicking the behaviour of ideal zig-zag and armchair graphene edges. This would then allow to study theoretical predictions, made for these boundary conditions, in artificially created graphene nanostructures.

Chapter 5

Scanning gate microscopy on a graphene quantum point contact (QPC)

In the previous chapter, it has been shown that a quantum dot structure fabricated in graphene using local anodic oxidation shows quantum Coulomb blockade behaviour at low temperatures. This implies directly that the lines confining the quantum dot structure, which have been oxidized using scanning probe lithography, are electrically insulating. Otherwise one wouldn't be able to measure the observed quantum dot characteristics of the graphene nanostructure. In this chapter, a further proof of the insulating electrical properties of the areas oxidized in graphene using local anodic oxidation is presented. Additionally, the experiment discussed below shows the possibility of changing the conductance through a graphene nanostructure using a moveable, local top-gate under ambient conditions.

Graphene nanostructures, such as nanoribbons [33] [59] [60], quantum point contacts (QPC) [34], single electron transistors [3] [35] and quantum dots (QD) [34] [45] offer intriguing new possibilities in the field of nanoelectronics. It has been shown how to routinely fabricate these graphene-based nanoelectronic devices, using either standard electron-beam lithography with subsequent reactive ion etching [33,59,34,35], or employing AFM-tip assisted etching of graphene [42, 45,22,43] (by applying a voltage between a conductive AFM tip and a grounded graphene flake in humid atmosphere to achieve direct etching of the graphene

crystal into the desired device structure). In both cases the electronic structure of graphene is altered (band-gap opened up) due to size quantization in nanostructured graphene. However, the transport properties of such structures depend strongly on the particular distribution of the Coulomb potential along their edges [61, 62, 63], so one would benefit from the detailed information about the spatial distribution of the energy gap introduced [64].

While the electronic properties of nanostructured graphene devices are most commonly studied using either the global electrostatic back-gate [33, 59, 45, 61, 63] or side-gates [60, 35, 61, 63], conducting transport experiments using local scanning electrostatic gating of such nanostructures is relatively new [64], and is yet to be further explored. Local electrostatic gating of graphene nanostructures complements experiments employing a global back-gate in that it allows for precise local control of the charge carrier density inside the final device structure. The local gating leaves the remaining part of the device, such as source and drain contacts, unaffected. It thus yields additional information on the electronic transport properties of these nanostructured devices, which allow for an exclusive characterisation of the working part, i.e. the respective nanostructure, of the graphene device.

A powerful tool in accessing this regime of electronic transport measurements is scanning gate microscopy (SGM). In SGM, the biased tip of a scanning probe microscope serves as a local top-gate, which can be moved across the sample surface. This enables one to measure changes in the conductance of a sample, when the charge carrier concentration in the sample is altered by the voltage applied to the tip, as a function of tip position. A further advantage of SGM over static local top-gates, as used e.g. in [62, 36], is the possibility to vary the coupling of the electric field of the top-gate (here the AFM tip) as the distance between the top-gate and the graphene device can be continuously changed.

First examples of the two-dimensional mapping of differences in the local conductance of graphene devices consisting of micrometer-sized graphene sheets using SGM were already given [65, 66, 67]. But so far, only one study [64] investigated the local conductance of a graphene nanostructure using SGM, at low temperature.

5.1 Introduction to scanning gate microscopy

Scanning gate microscopy (SGM) is an experimental method, which allows for the characterization and imaging of electrical transport in a given electronic device structure. It is a real space technique, with a spatial resolution in the nm-range. In the past, SGM was successfully applied to locate and characterize local potential barriers in electronic device structures based on carbon nanotubes [68, 69] and to reveal their influence on charge carrier transport in such devices [70, 71].

The physical principle behind SGM is the electric field effect, analogous to the working principle underlying the metal-insulator-semiconductor-(MIS)-capacitor. A potential difference (referred to as the gate voltage) between a metal electrode (called the gate) and a semiconductor, separated by a thin insulating layer, leads to either a depletion or an accumulation of charge carriers in the semiconductor. This gate voltage-induced change in the charge carrier concentration alters the conductance of the semiconductor.

In SGM, instead of having a fixed back-gate as in an MIS-capacitor, the tip of a scanning probe microscope serves as a local top-gate, which can be moved across the sample surface. This enables one to measure changes in the conductance of a sample, when the charge carrier concentration in the sample is altered by the voltage applied to the tip, as a function of tip position. Local perturbations of the sample, such as defects and the presence of localized charged impurities have by definition an electronic structure, that differs from the unperturbed sample. Hence SGM might provide a straight-forward way to image and characterize them.

The principle measurement setup for SGM is shown in Fig. 5.1. In SGM a voltage (in the shown case it is the AC-reference-voltage of a lock-in amplifier F) is applied to an electrically conductive tip A that is raster scanned in a certain height above a device structure to be investigated. A device structure consists of a graphene flake B on an oxidized D silicon wafer E, with the graphene flake being equipped with metal contacts C to allow the application of a current (in the picture indicated as a DC-voltage by using a battery H in combination with the resistor I) along the graphene flake. In order to do so, one of the electrodes must be grounded. The same ground is used for the voltage source which is connected to the tip.

Alternatively, one can also apply a DC-voltage to the AFM tip and pass an AC-current through the sample. The advantage of the former approach is that by performing a lock-in measurement, one obtains a higher sensitivity when the
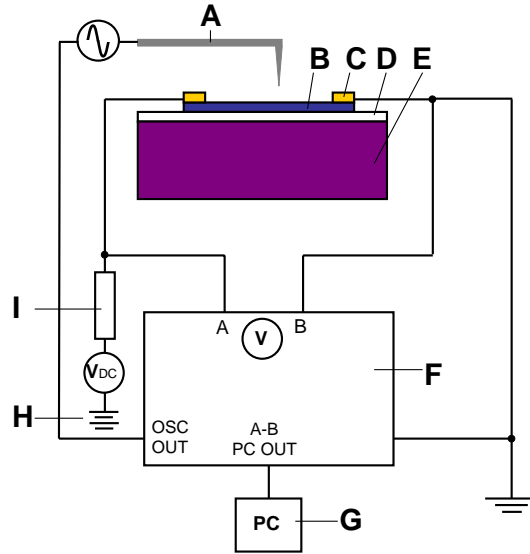
Figure 5.1: Schematic view of a possible scanning gate microscopy setup. An AC-biased conductive AFM-tip A is moved across the surface of an electrically contacted C graphene sample B. The graphene sample is supported on an oxidized silicon wafer D,E. Applying a DC-voltage H to the graphene sample leads to a current flowing through the graphene. The resistor I serves to limit the flowing current to not burn the sample. Since the AC-electric field of the tip changes the density of charge carriers in the graphene sample, a local change in sample resistance occurs. This change in sample resistivity can be detected with a Lock-In-Amplifier F. For displaying the change in sample resistance with respect to the tip position, a PC G is employed.

voltage applied to the AFM tip is modulated with the reference frequency of the lock-in amplifier.

While the AC-biased tip is scanned above the graphene flake, the electric field between the tip and the sample then changes the charge carrier concentration in the area of the graphene flake below the tip, and hence its conductivity. Since an AC-voltage is applied to the tip, there is a periodic change in the conductivity of the sample below the tip position. This is equal to a change in the local resistivity of the sample at the given tip position. A changed sample resistance implies that under the given constant DC-current through the sample this will result in a changed voltage drop across the sample (namely between the two contacts, between which the DC-current has been applied). The measurement of this voltage drop is carried out with the lock-in amplifier. The lock-in amplifier only measures a voltage drop, that is modulated with the frequency of the AC-voltage applied to the tip. Thus, one measures almost exclusively the local changes in the sample resistance that are caused by the influence of the electric field of the tip, which

is scanned above the sample.

Quantitatively, the AC-biased AFM tip changes the concentration of charge carriers, n, in the part of the sample below the tip according to:

$$n = n_0 + \beta \cdot V_{tip}, \tag{5.1}$$

with n_0 being the charge carrier concentration of the sample area below the tip without the tip being present. So the AC-biased tip is periodically depleting or accumulating charge carriers in the sample area below the tip. Plugging the AC-voltage applied to the tip into equation 5.1 gives:

$$n = n_0 + \beta \cdot V_0 sin(\omega \cdot t + \Phi). \tag{5.2}$$

V_0 is the amplitude of the AC-voltage, ω is the oscillation frequency and Φ is the phase of the AC-signal. The prefactor β is given by:

$$\beta = \frac{\epsilon_0 \epsilon}{ze}. \tag{5.3}$$

Herein ϵ_0 is the dielectric constant of vacuum, ϵ is the dielectric constant of the material between the AFM-tip and the sample, in our case it is the one of air. z is the distance between tip and sample, and e is the elementary charge of an electron.

This local change in the charge carrier concentration leads to a change of the local conductivity σ in the given sample area:

$$\sigma = n\mu e. \tag{5.4}$$

μ is the mobility of the charge carriers in the part of the sample below the AFM-tip. If the charge carrier concentration is changed as outlined above, the conductivity reads:

$$\sigma_{tip} = (n_0 + \beta \cdot V_0 sin(\omega \cdot t + \Phi))\mu e. \tag{5.5}$$

The sample is assumed to be split up into N squares of equal size, as shown in Fig. 5.2. σ_{tip} is the conductivity of the square, which is influenced by the tip. Because the DC-current through the sample is known, in the ideal case one
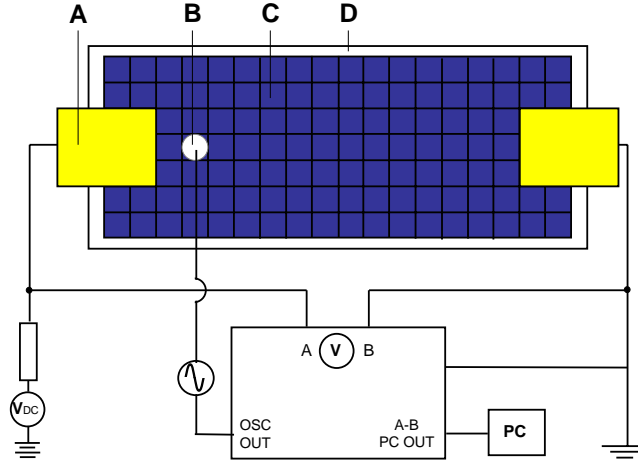
Figure 5.2: Top View of the scanning gate microscopy setup. A DC-current is applied to a an electrically contacted A graphene flake C, which is lying on an oxidized silicon wafer D. The graphene sheet can be divided into squares. Each square has a size of the order of 10nm, given by the resolution achievable in SGM. Raster scanning the conductive AFM-tip B across the graphene flake allows to obtain a two dimensional map of the conductivity in the device structure imaged.

measures (by measuring the voltage drop at the lock-in amplifier):

$$\sigma_{tip}^{mod} = (V_0 sin(\omega \cdot t + \Phi))\mu e. \tag{5.6}$$

Hence, SGM can be used to locally map variations in sample resistance (due to local variations in charge carrier concentration), as a function of AFM tip position.

In reality, there is always a background resistance being present, which depends on the sample size. The narrower the sample, as for example in the case of carbon nanotubes, or nanowires, the stronger the effect of the AFM tip-induced carrier modulation, and hence a larger signal at the lock-in will be detected. The wider the sample, the less the AFM tip induced change of carrier concentration affects the overall resistance. Accordingly, the signal measured at the lock-in will decrease.

The lateral resolution in SGM experiments depends on the tip-radius and on the distance between tip and sample. The achievable lateral resolution was estimated to be of the order of 10 nm [68]. In combination with the ability to raster scan the conductive AFM tip across the device structure to be investigated, this allows a two dimensional imaging of the sample conductivity with high lateral

resolution.

5.2 Experimental results

Graphene flakes were exfoliated from natural graphite and deposited on top of an oxidized silicon wafer. After selecting single layer flakes using optical microscopy [28] and Raman spectroscopy [32], Ti/Au-contacts were lithographically defined on the graphene flake. To confine these flakes to nanostructures, we have employed local anodic oxidation, as described in Chapter 3. Using contact mode AFM, we were scanning the biased AFM tip (V_{tip}= -7 V with respect to grounded sample) in a humid atmosphere (relative humidity of 70%) with a velocity of 200 nm/s to locally oxidize graphene to create the desired nanostructure geometries. The spring force applied to the AFM tip was set close to zero, but such that we were still able to obtain stable height images.

A QPC fabricated in this way in single layer graphene, as well as the corresponding scanning gate microscopy image, is shown in Fig. 5.3. On the left, a
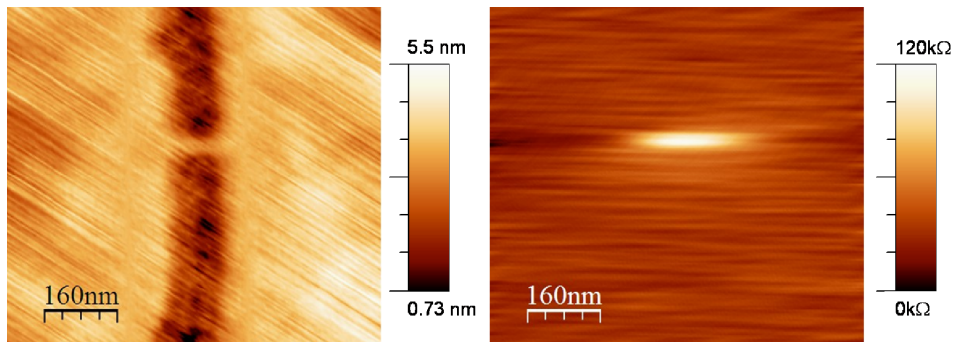
Figure 5.3: On the left, a contact mode AFM image of a quantum point contact (QPC) created in single layer graphene by AFM-based local anodic oxidation is shown. The graphene QPC is about 80 nm long and about 35 nm wide. On the right, the change in the resistance of the graphene device, obtained at the same position where the topography shown on the left was taken, is shown when scanning the DC biased AFM tip (V_{tip}=-0.5 V) across the sample surface. Clearly, the resistance of the sample under the influence of the electric field of the biased AFM tip only changes at the position of the graphene QPC, corresponding to the centre of both images, on the left and on the right. All other areas on the right image show the same color, indicating that no changes in sample resistance were detected when the AFM tip was scanning these positions. This background resistance is about 14 kΩ, while the resistance at the QPC increases to a maximum of 120 kΩ.

contact mode AFM topography of the final nanostructured graphene device is shown. A dark vertical line in the middle of the image can be seen, which corresponds to the area of the graphene sheet that was oxidized by AFM local anodic oxidation. Left and right of this line are intact graphene areas (bright color). The dark line is only interrupted by a small area, about 35 nm wide and about 80 nm long, which can be seen in the centre of the image. This small area is the graphene quantum point contact. The image on the right in Fig. 5.3 was obtained on the same area as shown on the topography image on the left. It corresponds to the voltage drop across the sample, measured with the lock-in technique at each position of the AFM tip, under ambient conditions. For the measurement shown, a DC-voltage of V_{tip}=-0.5 V with respect to ground was applied to the AFM tip (Nanosensors PPP-CONTR highly doped silicon tips). An AC-current of 1 μA was applied across the QPC shown on the left. We chose contact mode AFM to scan the biased AFM tip across the sample, while simultaneously measuring the sample resistance. This is slightly different to the common operational mode of SGM of lifting the biased AFM tip to a certain height (e.g. about 5 nm [66]) above the sample. We assumed the resistance between AFM tip and sample to be on the order of several hundred kΩ , and hence chose contact mode scanning to have the strongest coupling of the electric field of the AFM tip to the graphene nanostructure (due to minimal distance between the AFM tip and the sample). The rather uniform background (all areas of the image except the centre part) on the right image of Fig. 5.3 justifies our assumption that there is no ohmic current between the biased AFM tip and the sample.

As is clearly visible, the only significant change in the sample conductance happens at the position of the quantum point contact. This manifests itself in the bright spot seen in the centre of the right image in Fig. 5.3, at exactly the same position where the QPC is found in the sample topography, as shown on the left side. All other areas of the sample show a more or less uniform colour, indicating that the sample conductance in these areas was not affected at all by the local gating exerted by the AFM-tip.

This result also proves the electrically insulating behaviour of the lines created by scanning probe lithography, which in the case discussed here effectively define the graphene quantum point contact. If these lines were not electrically insulating, the area where the quantum point contact is defined shouldn't differ in terms of conductance from the remaining part of the graphene flake. But then,

one would not expect to observe a pronounced susceptibility to the electric field of the AFM tip at this position. This contradicts our results, as is evident from Fig. 5.3.

5.3 Conclusions

This experiment successfully demonstrates the ability to locally change the conductance of a graphene nanostructure by means of a biased AFM tip under ambient conditions. It opens the possibility for more refined studies, examining either the electronic transport behaviour for any user-defined geometry of the graphene nanostructure. Alternatively, one could also vary the voltage being applied to the AFM tip, or the distance between AFM tip and sample, to study in more detail how this will affect the charge carrier transport through the nanostructures.

Furthermore, it was confirmed that the lines oxidized in graphene using local anodic oxidation are insulating in terms of electronic transport. If they were not insulating, no pronounced effect of the applied AFM tip bias on the conductance through the sample in the region of the constriction should be seen during the SGM experiment. The constriction would then not behave as a bottleneck for electronic transport, contrary to what we have observed. This result proves that AFM-based local anodic oxidation is a well-suited technique to perform lithography on graphene crystals, yielding nanostructured graphene devices with the same quality as those fabricated using standard electron beam lithography with subsequent plasma etching.

Chapter 6

Determining the chirality of graphene edges

Single layer graphene was first isolated in 2004 by using the micromechanical cleavage technique [1, 2]. Although a number of other methods for graphene synthesis have been proposed since then (including the reduction of graphene oxide [72], decomposition of silicon carbide [73, 74], epitaxial growth on Nickel and other substrates [75, 76, 77, 78] or direct chemical exfoliation [79, 80] the micromechanical technique (also known as the "Scotch-tape method") is still the procedure of choice for many researchers. Furthermore, the uniqueness of this procedure is that it reveals the peculiar micromechanical properties of this material, which might be used in obtaining crystallographically oriented graphene samples [3, 81]. The choice of crystallographic orientation of the graphene flakes might be of crucial importance for the electronic properties of resulting devices [58, 57, 82]. Two problems generally arise: (i) how to determine the crystallographic orientation of a particular graphene crystallite and (ii) how to prepare a device which is oriented exactly along one of those directions. Whenever there are quite a few ways for determination of the orientation [83, 84, 85, 86, 87], preparation of well oriented edges is a challenging task. It has been noted [81] that flakes obtained by the "Scotch-tape method" often exhibit straight edges with the angle between the adjacent ones being a multiple of 30°. An example of such a flake is shown in Figure 6.1.

Considering the hexagonal symmetry of graphene crystals, it has been suggested that the breaking occurs along the principal crystallographic directions, yielding flakes terminated with either armchair or zigzag edges [3, 81]. Previously,
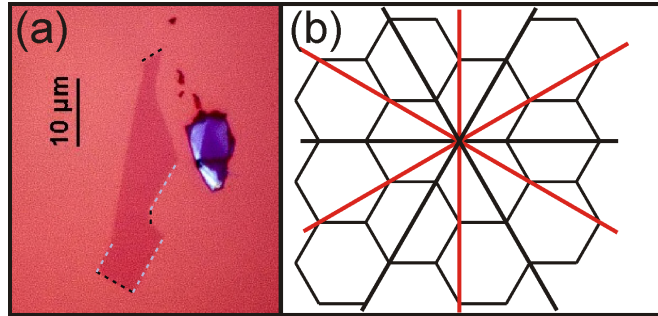
Figure 6.1: (a) Optical image of a single layer graphene flake prepared by microme-chanical cleavage. It can be clearly seen that the edges terminating the graphene crystal follow straight lines up to lengths of several micrometers. Certain edges of this particular flake, oriented relative to each other in integer multiples of 30°, have been highlighted by a dashed line (black and light-blue, for the respective type of edge). (b) Sketch of the honeycomb crystal lattice of graphene. Two distinct crystallographic orientations of a graphene crystal are possible: armchair (black), and zigzag (red). Redrawn from [88]

Raman measurements have been employed to verify this idea [85, 86], demonstrating a clear difference in the amplitude of the D peak for edges oriented along zigzag and armchair directions. However, Raman measurements require elaborate modeling to explain the finding. In this chapter, I will show how high-resolution scanning tunneling microscopy (STM) can be used to prove beyond doubt that edges of graphene crystals are predominantly oriented along crystallographic directions. The main advantage of high-resolution STM compared to the aforementioned techniques is its ability to provide direct real-space images of the graphene crystal lattice with atomic resolution. Additionally, there is no need to have suspended samples, as e.g. for transmission electron microscopy (TEM) experiments, in order to carry out STM investigations. Thus, it ultimately enables one to directly determine the crystallographic orientation of a given graphene flake, and hence the orientation of the edges terminating that sample. I will also compare the results of the STM study to the Raman measurements.

The main results of this chapter have been published in [88].

6.1   STM on graphene and graphite

In an atomically resolved image of a graphene crystal, obtained by STM, one should see all six atoms forming the honeycomb unit cell of the crystal lattice of

graphene [89]. This is in contrast to three dimensional graphite, as for example in highly oriented pyrolithic graphite (HOPG), where one only sees every second atom of the surface honeycomb unit cell in an atomically resolved STM-image.

In HOPG, the single graphene layers are stacked together perpendicular to the plane in the so-called Bernal stacking (see Fig. 6.2 for a schematic depiction), following an ABAB... alternation of atomic planes. This implies that every second
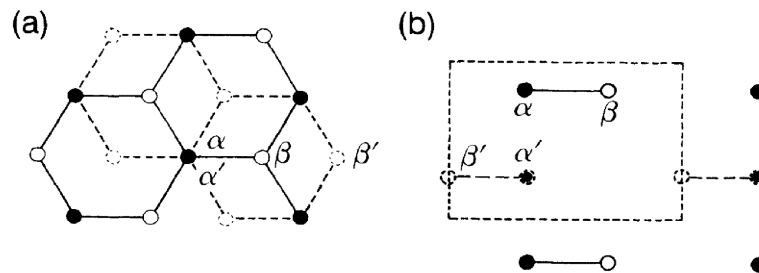
Figure 6.2: Schematic of the Bernal stacking of graphene layers in graphite (HOPG). Top view (a) and side view(b) of two stacked graphene layers, representing A and B. The unit cell of HOPG is drawn in (b) as a dashed line. While the atoms labelled α in the topmost layer sit directly on top of an atom of the underlying layer, the atoms labelled β sit on top of the center of the honeycomb of the underlying atomic plane. After [90].

atom, called α in Fig. 6.2, of the honeycomb unit cell of the topmost graphene sheet sits on top of a Carbon atom (labelled α') of the graphene sheet located directly below the topmost sheet. The remaining three Carbon atoms of the honeycomb unit cell of the topmost layer sit on so-called hollow sites, where there is no Carbon atom located directly underneath them. These Carbon atoms are labelled as β in the topmost layer, and β' in the layer directly underneath the topmost layer.

An example of an atomically resolved STM image taken on HOPG is shown on the left in Fig. 6.3. This STM-image shows the trigonal symmetric arrangement of atoms that is commonly observed for atomically resolved images of the HOPG surface. The reason that only every second atom (appearing as bright protrusion in Fig. 6.3) of the honeycomb unit cell of the topmost graphene sheet on the surface of HOPG is observed can be explained by the site asymmetry of the α- and β-Carbon atoms in Bernal-stacked HOPG.

Because the α-atoms sit on top of a Carbon atom in the layer directly underneath them, their electronic bands along the vertical line at the corner of the
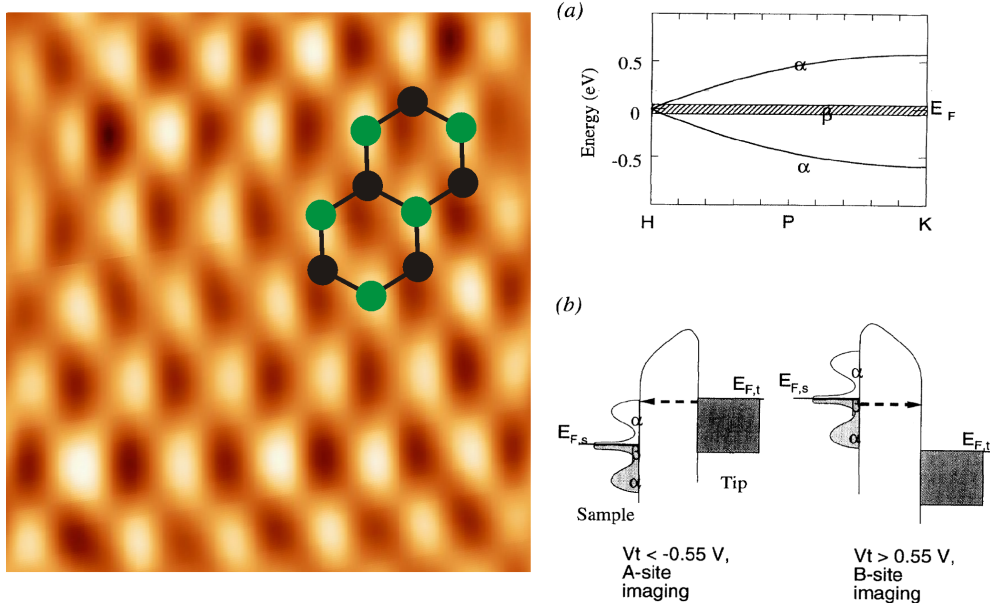
Figure 6.3: Left: Atomically resolved constant-height STM image of HOPG (sample bias +240 mV, tunnel current 1.7±0.2 nA). The trigonal symmetry indicates that only every second atom of the honeycomb unit cell of the topmost graphene layer is visible. These atoms appear as bright protrusions, whereas the dark spots correspond to the center of the honeycomb unit cell. A model honeycomb is drawn on top for illustration, showing that one type of Carbon atoms (green spots) is seen, whereas the nearest neighbour atoms (black spots) are not visible. Right: In (a) the energy dispersion of the bands belonging to α- and β-atoms along the vertical line on the corner of the Brillouin zone of HOPG are shown. In (b) the energy landscape for electrons tunneling from tip to sample (left) or vice versa are shown. The density of states of the sample is depicted qualitatively for the HOPG surface, with its contributions arising from α and β-atoms indicated. In the absence of any mechanical interactions between the STM-tip and the HOPG surface, one can only image α-atoms at tunneling voltages smaller than -0.55V applied with respect to the sample. After [91].

Brillouin zone of HOPG show dispersion, as shown on the top of Fig. 6.3(a). On the other hand, the electronic band of the β-atoms is localized near the Fermi level for that part of the Brillouin zone. This results in a higher one-dimensional density of states near the Fermi-level (predominantly β-atoms), as shown qualitatively in the bottom part of Fig. 6.3(b). Gwo and Shih [91] have demonstrated for the first time that it is possible to selectively image both α- and β- atoms of the HOPG surface, depending on the polarity and the magnitude of the tunneling bias voltage.

Thus, while it is possible to image both type of atoms, still only one type of atoms will be visible under each respective condition only. In the case of a single

isolated graphene sheet, this situation is entirely different. Because in the latter case, we investigate only a single layer of Carbon atoms arranged in a honeycomb lattice, there is no site asymmetry between the Carbon atoms of the honeycomb unit cell. Thus, all six Carbon atoms constituting the honeycomb have the same electronic dispersion, and hence the same density of states. Therefore, in an atomically resolved STM-image of single layer graphene, we should see all six atoms of the honeycomb unit cell.

6.2 Determining the chirality of graphene edges

For certain flakes obtained by micromechanical cleavage, there is strong evidence that their edges are crystallographic, i.e. that they follow well-defined crystallographic orientations.

Single layer graphene flakes were obtained by micromechanical cleavage of natural graphite. Exfoliated graphite flakes were deposited on top of an oxidized silicon wafer (300 nm of SiO_2), and crystallites of single layer thickness were identified using optical microscopy [28]. For our studies, we used flakes with a significant percentage of edges forming angles which are integer multiples of 30°. Examples of such flakes are shown in Figure6.1(a) and Figure 6.4(a). Upon selection of appropriate flakes, we used e-beam lithography to define electrical contacts on the flakes (Ti, 5 nm + Au, 40 nm) (Figure 6.4(b)). In order to find out whether the edges of e.g. the graphene flake shown in Fig. 6.4 follow crystallographic orientations, we carried out high-resolution scanning tunneling microscopy investigations. A Multimode scanning probe microscope with a Nanoscope IIIa controller was employed for conducting the STM experiments. All STM experiments were carried out under ambient conditions. Tunneling tips were made out of mechanically cut Pt_{80}/Ir_{20}-wire. The samples were precisely positioned in our STM, and the scanning direction was carefully aligned with one of the edges. Prior to imaging, the flakes were annealed at 250°C in a hydrogen/argon-atmosphere [29], in order to remove resist residuals due to the lithography treatment. After that, the flakes were found to be clean enough to achieve atomic resolution. Figure 6.4(c) shows an STM image of the graphene flake shown in Figure 6.4(a), taken in constant-height mode at a sample bias of 223mV and a set-point tunneling current of 2.8 nA (the tunneling current varied
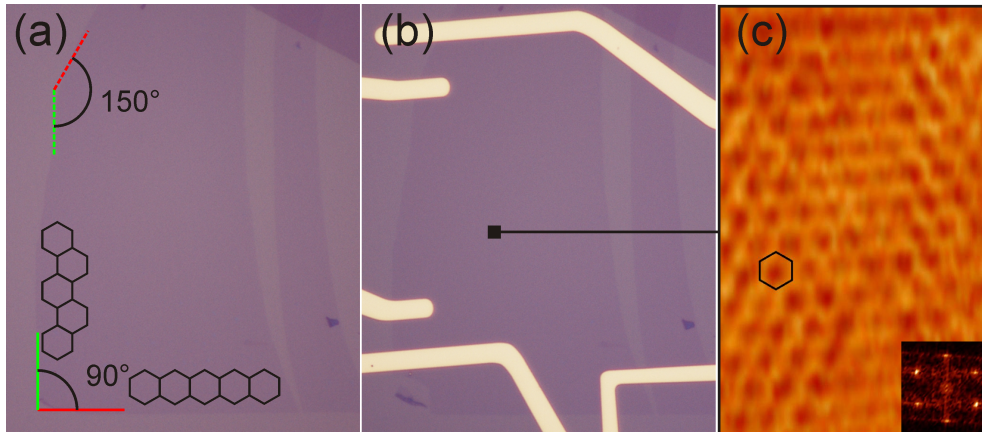
Figure 6.4: (a) Typical graphene flake obtained by micromechanical cleavage. Two distinct types of edges, rotated against each other in multiples of 30°, are indicated as armchair type (green) and zigzag type (red). (b) To carry out STM imaging, the flake in (a) was equipped with electrical contacts, and oriented carefully along the scanning direction of the STM-tip. (c) STM constant-height image (+0.223V, (2.8 plus minus 0.3)nA), showing atomic resolution of the graphene hexagonal lattice. The inset on the lower right shows the Fourier transform of that image, where six well resolved diffraction spots are clearly visible. A single black hexagon is drawn as guide to the eye. Superimposing that hexagon onto the optical image proves the crystallographic orientation of the two indicated edge types. Redrawn from [88].

by a maximum of ± 0.3 nA between positions on the atoms and interatomic positions). The atomically resolved hexagonal graphene lattice can be clearly seen, which is a clear proof of the monolayer character of this particular sample [89]. The Fourier transform of that image, shown in the inset on the lower right of Fig.2(c), accordingly shows six well-resolved diffraction peaks. Both the atomically resolved image of the lattice and the Fourier transform image allow us to determine the orientation of the edges of a given graphene flake. This is done by virtually tiling the entire graphene flake in question with the experimentally observed hexagonal unit cell (or equivalently the corresponding Fourier transform). Following this approach for the flake shown in Figure 6.4(a), we can identify the green edge as being armchair and the red edge as being zigzag.

Additional information about the edges can be obtained from the Raman measurements. Recent results show that it is possible to distinguish between armchair and zigzag orientation by Raman spectroscopy [85]. The disorder-induced Raman feature of graphene (D peak at approximately 1350 cm^{-1}) is activated through a double resonance process [92] and is often observed at the edges. This is because

the edges act as defects, allowing elastic backscattering of electrons to fulfill the double resonance condition [93]. The D peak was reported to be stronger at the armchair edge and weaker at the zigzag edge, due to the momentum conservation (armchair edges can scatter electrons between two non-equivalent Dirac cones, while zigzag edges cannot) [85, 93]. Raman measurements were carried out using a WITec CRM200 confocal microscopy Raman system with a 100x objective lens (numerical aperture=0.95). The excitation laser wavelength is 532 nm. We measured Raman spectra from points A and B, which are two edges forming an angle of 90°, as labelled in the inset (optical image) of Figure 6.5. During the
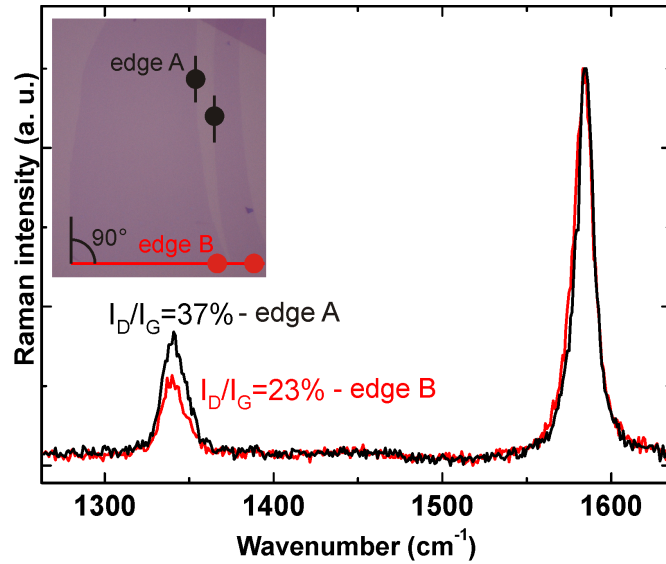
Figure 6.5: Raman spectra taken from two different edges (optical image shown in the inset on the upper left), labelled edge A (vertical line, black spots) and edge B (horizontal line, red spots), forming an angle of 90°. As graphene has a hexagonal crystal lattice, the two edges are believed to have different chirality. During the measurement, the laser polarization (linear) is oriented parallel to the graphene edge being measured, to maximize the D peak signal. The Raman spectra at edge A (black) shows a D-peak intensity of 37% compared to the G-peak intensity, while it is only 23% for the spectra taken at edge B (red). Raman spectra from different spots of the two edges gave similar results. This confirms our finding that edge A is armchair, whereas edge B is zigzag. Redrawn from [88].

measurement, the laser polarization (linear) is oriented parallel to the graphene edge under investigation, in order to maximize the D peak signal [85, 93]. To determine the exact position of the graphene edge, Raman spectra were taken at different positions while scanning the laser spot perpendicularly across the particular edge under question (with a step size of 50 nm). The maximum intensity

of the D-band measured under these conditions was taken in order to compare the two different edges. As shown in Figure 6.5, at point A, the D peak intensity is 37% of that of the G peak, while it is only 23% at point B. This suggests that the edge containing point A is armchair while the other edge is zigzag. Raman spectra from different points of the two edges were checked and similar results were obtained. The Raman results confirm the STM results of the graphene crystallographic orientation. Here, we have to clarify that the edges mentioned above are predominantly crystallographic, as perfect zigzag and armchair edges are extremely rare. There are small amounts of armchair sections even on zigzag edges, both on exfoliated single layer graphene [57, 62, 94] and terraces on bulk graphite [95], which contribute to the observed D peak at point B.

6.3 Conclusions

In conclusion, we have demonstrated the direct determination of the crystallographic orientation of graphene edges by using high-resolution STM. The obtained atomic resolution images of the graphene crystal lattice have allowed us to unambiguously identify both armchair and zigzag edges of a given graphene flake prepared by mechanical exfoliation. Complementary information has been obtained by Raman spectroscopy, fully justifying our assumption that certain edges on micromechanically exfoliated samples predominantly follow crystallographic orientations of the underlying graphene crystal lattice.

Moreover, these experiments constitute a direct proof that the theoretical model underlying the interpretation of Raman spectra of graphene edges is valid. The Raman spectra obtained from the two different crystallographic edge types show the behaviour as expected from the model, which predicts that no D-peak should occur at zigzag edges, but that it should be observed on armchair edges. The atomic resolution images obtained from STM experiments fully support these findings, and hence validate the theoretical model. For graphene flakes being terminated by straight edges which enclose an angle of integer multiples of 30° with each other, Raman spectroscopy can thus be used to determine the crystallographic orientation of the underlying graphene crystal reliably.

Chapter 7

Engineering resistance in graphene

Elias et al. [11] demonstrated for the first time the reversible chemical modification of graphene crystals using atomic hydrogen. They showed that exposing a pristine graphene crystal to atomic hydrogen transforms the zero-gap semiconductor graphene into a material exhibiting a metal-insulator transition. Furthermore, by studying the hydrogenated graphene crystals with Raman spectroscopy, the occurence of a pronounced D-peak was found. Annealing the hydrogenated graphene crystals led to the recovery of the properties of pristine graphene in terms of electronic transport. Additionally, the observed D-peak in the Raman spectra of hydrogenated graphene was found to be strongly suppressed after annealing.

Besides the fact that this approach showed the fabrication of a new two-dimensional material based on graphene, its implications for the behavior of electronic transport in graphene are equally important. Pristine graphene is a zero-gap semiconductor, with very high charge carrier mobilities that are practically independent of charge carrier concentration [3]. The latter causes problems, if graphene is considered to be used in conventional semiconductor circuit technology, where a non-conducting state of the materials used has to be present. As was demonstrated by Elias et al. [11], hydrogenated graphene offers a promising opportunity to address this point.

In this chapter, I will present further investigations on single-sided hydrogenated graphene (i.e. graphene on top of an oxidized silicon wafer that was

hydrogenated). In particular, we investigated the surface morphology of hydrogenated graphene using TappingMode AFM. Afterwards, fundamental changes induced in the hydrogenated samples by scanning them using contact mode AFM are discussed.

7.0.1 Sample fabrication

All pristine graphene crystals used in this work were prepared using micromechanical exfoliation from natural graphite [1] on top of an oxidized silicon wafer. The single-layer nature was identified using optical microscopy [28] and Raman spectroscopy [32]. Hydrogenation of the monolayer graphene crystals was done according to [11] by exposing the samples to a cold hydrogen plasma. A low-pressure (0.1 mbar) hydrogen/argon mixture (10% H_2) with dc plasma ignited between two aluminum electrodes was used, as described in Ref. [11]. In total, the samples studied in this chapter have been exposed for a total of 45 min to the dc plasma.

7.0.2 Raman spectroscopy of hydrogenated graphene

The changes in the properties of graphene induced by hydrogenation have been corroborated by Raman spectroscopy [11]. The main features in the Raman spectra of graphene have been discussed in the first chapter. The results obtained by Elias et al. for the evolution of Raman spectra for graphene crystals that are hydrogenated and annealed, are shown in Fig. 7.1. The red curve corresponds to pristine single layer graphene. It was taken at a laser excitation wavelength of 514 nm. It shows the G-peak at 1580 cm^{-1} and the 2D-peak at around 2680 cm^{-1}, as discussed in the first chapter. No D-peak was observed. The blue curve corresponds to hydrogenated graphene. Next to the G- and 2D-peak, sharp D- and D$'$-peaks appeared. Additionally, a slight broadening and a decrease of the height of the 2D-peak relative to the G-peak is observed. The onset of a combination mode D+D$'$ is also visible around 2950cm^{-1}. The D-peak in graphitic materials lies at 1350 cm^{-1}. It is a breathing-like mode, caused by transverse optical phonons near the K-point of the reciprocal lattice, and requires a defect for activation via an intervalley double resonance process. The ratio of the intensity of the D-peak over the intensity of the G-peak is a measure for the amount of
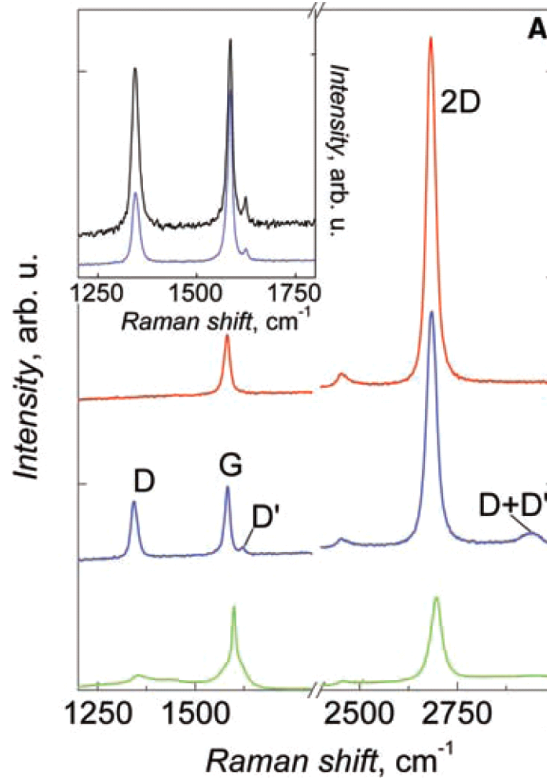
Figure 7.1: Changes in Raman spectra of graphene on top of silicon oxide caused by hydrogenation. Red, blue, and green curves (top to bottom) correspond to pristine, hydrogenated, and annealed samples, respectively. The spectra were measured with a Renishaw spectrometer at wavelength 514 nm and low power to avoid damage to the graphene during measurements. The inset shows the comparison between the evolution of the D- and D′-peaks for single- and double sided exposure to atomic hydrogen. For double sided exposure (black curve), the intensity of the Raman D-peak is found to be twice as large as that for single sided exposure (blue curve). This proves that the observed Raman D-peak is caused by hydrogen adsorbed to graphene. Figure taken from Ref. [11].

disorder being present. In the Raman spectra shown, the D-peak for hydrogenated graphene is found at 1342 cm^{-1}. It is very sharp. Elias et al. attributed the activation of this sharp D-peak in hydrogenated graphene to the breaking of the translational symmetry of the C-C sp^2-bonds of the graphene lattice after the formation of C-H sp^3-bonds during hydrogenation [11]. From the inset of Fig. 7.1, where Raman spectra are shown for the cases of single- and double sided exposure to atomic hydrogen, one can conclude that Raman spectroscopy is a suitable tool to characterize the hydrogenation of graphene. For the case of double sided exposure to atomic hydrogen (black curve), which was achieved by using a freestanding graphene membrane as sample, the intensity of the D-peak in

the Raman spectrum is twice as large as that for single sided exposure to atomic hydrogen (blue curve), obtained for graphene placed on a substrate. This directly leads to the conclusion that the intensity of the Raman D-peak is a measure of the amount of adsorbed hydrogen. The D'-peak is found at 1620 cm^{-1}. This Raman mode occurs via an intravalley double-resonance process in the presence of defects.

The green curve corresponds to the Raman spectrum of hydrogenated graphene after annealing (450°C in Ar atmosphere for 24 hours). After annealing, the Raman spectrum recovered to almost its original shape, and all of the defect-related peaks (D, D', and D+D') were strongly suppressed. However, two broad low intensity bands appeared, overlapping a sharper G and residual D peaks. These bands are indicative of some residual structural disorder [96]. The 2D peak remained relatively small with respect to the G peak when compared with the same ratio in the pristine sample, and both became shifted to higher energies, indicating that the annealed graphene is p-doped [97].

Elias et al. have found a broad agreement between the Raman spectra and transport measurements of the electronic properties of pristine graphene, hydrogenated graphene and annealed hydrogenated graphene [11]. Hence, for most studies of hydrogenated graphene presented in the following part, the Raman spectra were used to identify the samples under question as being hydrogenated.

7.0.3   Atomic force microscopy

After the initial characterization of hydrogenated graphene by electronic transport measurements and Raman spectroscopy, the question arose what the topography of hydrogenated graphene will look like. Since pristine graphene on silicon oxide was already well studied using atomic force microscopy [29], we chose to employ this technique in order to be able to compare our findings for hydrogenated graphene. A comparison of the topographies of pristine graphene on silicon oxide and hydrogenated graphene on silicon oxide is shown in Fig. 7.2. On the left, a TappingMode-AFM topography of a pristine graphene flake on silicon oxide is shown. The right image shows the topography of a hydrogenated graphene flake on silicon oxide, also measured using TappingMode AFM. The left image has a z-scale of 2.5 nm, and the right image has a z-scale of 10 nm. Judging from the images, one clearly observes a much rougher surface structure for hydrogenated
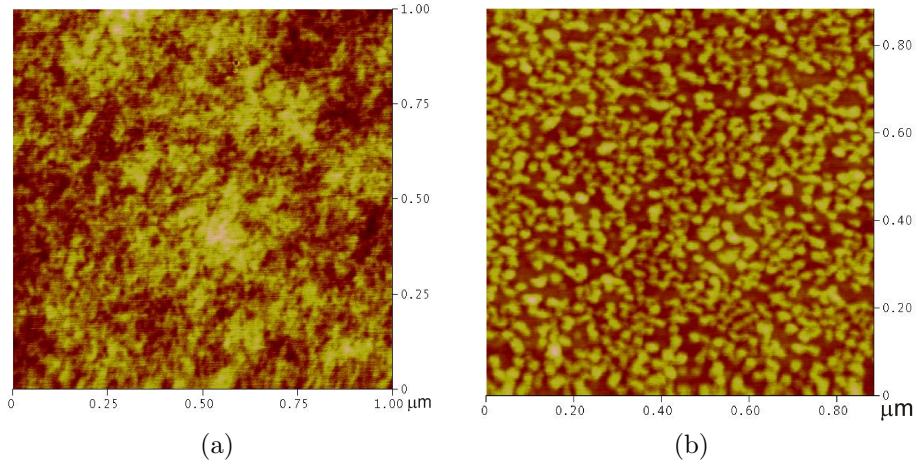
Figure 7.2: TappingMode AFM height images of (a) pristine graphene on silicon oxide and (b)Hydrogenated graphene on silicon oxide. Both images have to same z-scale of 2.5 nm. The hydrogenated graphene flake looks much rougher (rms value of surface roughness 0.4 nm) than the pristine graphene flake (rms roughness 0.11 nm). Whereas the pristine graphene flake looks rather flat, the hydrogenated flake shows a worm-like surface structure.

graphene (right image, rms roughness [1] of 0.4 nm) as compared to the case of a pristine graphene flake (left image, rms roughness of 0.11 nm), which looks rather flat and smooth. This value corresponds to what is routinely observed for the surface roughness of a graphene monolayer on silicon oxide [29].[2] A further analysis of the surface structure of hydrogenated graphene on silicon oxide is shown in Figs.7.3 and 7.4. To characterize the surface structure, the height and the width of have been determined on two representative positions. These are indicated by red arrows on the line profiles shown in part (b) of Figs. 7.3 and 7.4. The height and the width of the surface structure of hydrogenated graphene typically observed in TappingMode AFM imaging are determined to be 1.1 nm and 24.2 nm, respectively.

Because of this large difference in the surface structure of pristine graphene and hydrogenated graphene, we conclude that the worm-like surface structure is entirely due to hydrogenating graphene. Still, it remains unclear at which moment the characteristic worm-like surface structure forms on hydrogenated

---

[1]The rms roughness was taken as the root mean square average of the the height deviations from the mean data plane for all data points. This is expressed as: rms $= \sqrt{\frac{\Sigma z_i^2}{n}}$ [98].

[2]It is by now common to assume that a pristine graphene monolayer on silicon oxide acquires the morphology of the underlying silicon oxide substrate [29].
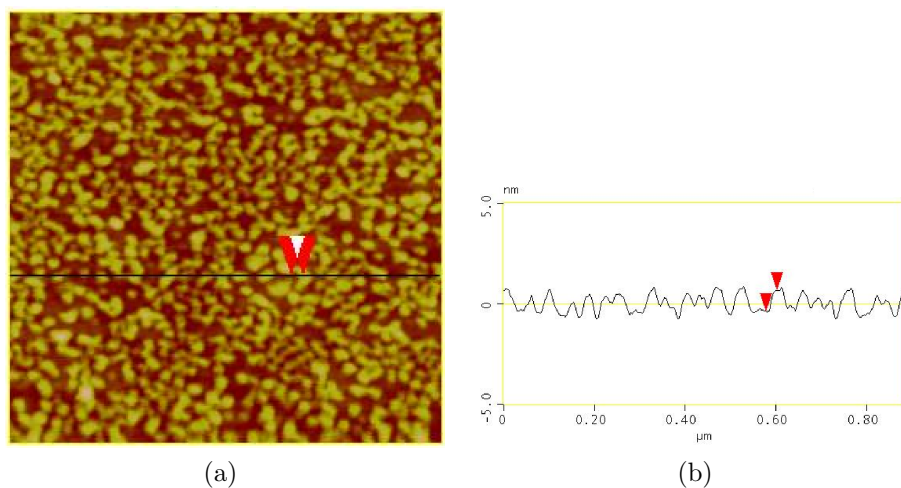
Figure 7.3: Analysis of the height of the surface structure of hydrogenated graphene. (a) Tapping Mode AFM topography. Two red arrows indicate the position where a typical surface feature of hydrogenated graphene has been measured. (b) The corresponding line profile. The height of the indicated surface structure is 1.1 nm.
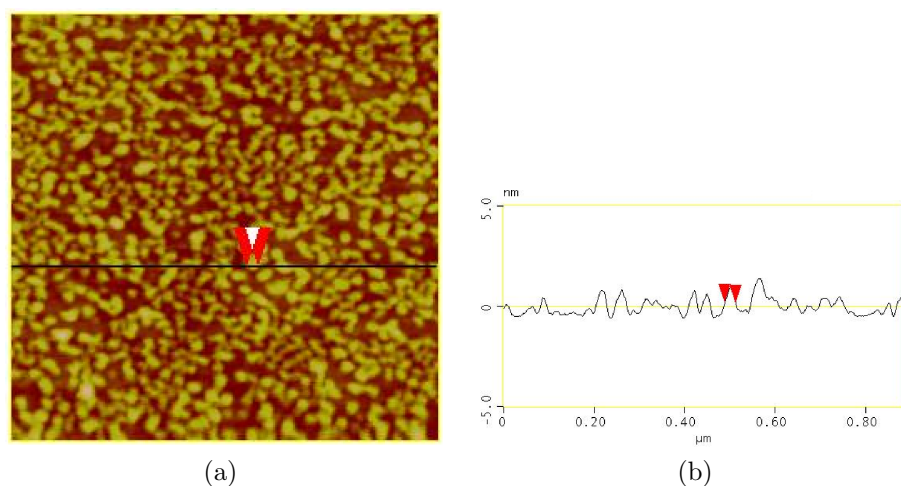
Figure 7.4: Analysis of the typical width of the surface structure of hydrogenated graphene. (a) Tapping Mode AFM topography. Two red arrows indicate, where the width of the surface structure has been determined. (b) Corresponding line profile. The typical width of the surface structure amounts to be 24.2 nm.

graphene. Furthermore, judging from the TappingMode AFM images alone it cannot be concluded whether the worm-like structure resembles the topography of the graphene flake after hydrogenation, or whether it is an adsorbate on top of the hydrogenated graphene flake. [3]

7.1 Scratching hydrogenated graphene

An interesting observation was made when imaging a hydrogenated graphene flake in contact mode AFM. The image of a hydrogenated flake in Fig. 7.5 was obtained in TappingMode AFM, after the same flake was partially imaged in contact mode AFM. There is a clear difference visible between the areas on the same
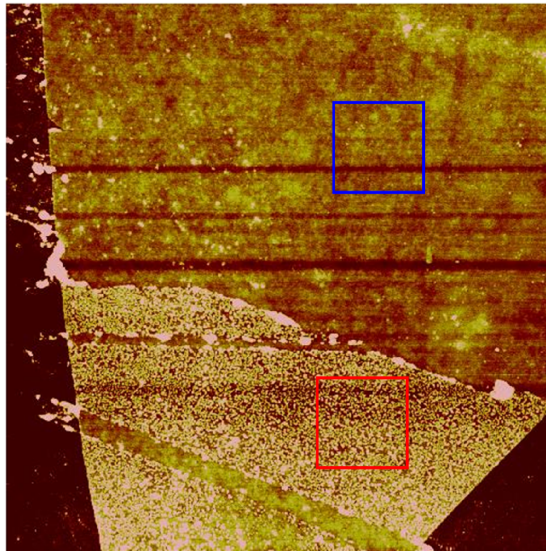
Figure 7.5: TappingMode AFM image (6 μm $\times$ 6 μm) of a hydrogenated graphene flake on silicon oxide after it was partially imaged in contact mode AFM. The area indicated by the blue square was imaged in contact AFM, whereas the area indicated by the red square was never imaged in contact AFM.

hydrogenated flake that have been exclusively imaged in TappingMode AFM, indicated by the red square, and those that have been imaged in contact mode AFM, indicated by the blue square. To further investigate this observation, high resolution images of the respective areas were taken in TappingMode AFM. They are shown in Fig. 7.6. On the left, a magnified topography of the area that was imaged in contact mode AFM is shown. The rms value of the surface roughness

---

[3]In [11], the possibility of water adsorbing on hydrogenated graphene is mentioned.
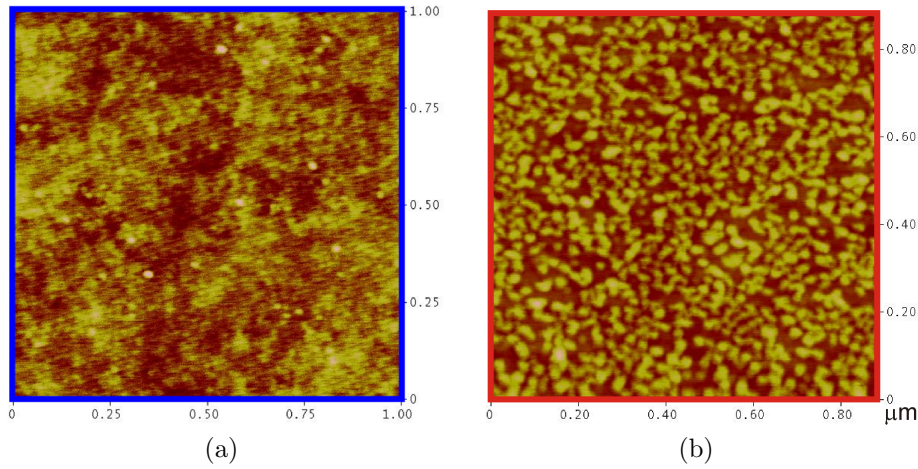
Figure 7.6: Two TappingMode AFM images of different areas of a hydrogenated graphene flake. (a)Height image of an area that has been previously been imaged in contact mode AFM. It looks rather flat, similar to pristine graphene on silicon oxide. Rms roughness 0.1 nm. (b) Height image of an area of the same hydrogenated graphene flake, that has been imaged exclusively in TappingMode. It shows the pronounced worm-like surface structure, with an rms roughness of 0.4 nm.

is 0.1 nm, a value similar to what is obtained for pristine graphene on silicon oxide [29]. The surface in this image looks flat, without any pronounced surface structure. It basically resembles the topography of a pristine graphene flake, as for example shown in Fig. 7.2 (a). This situation is markedly different when looking at an area of the same flake that was never imaged in contact mode AFM. An example of the surface topography for the latter is shown in Fig. 7.6 (b). This image now shows an rms roughness of 0.4 nm and the characteristic worm-like structure on the surface.

The situation just described was always observed for graphene flakes hydrogenated under the same conditions when imaged in one of the respective AFM imaging modes. Imaging a hydrogenated graphene flake in contact mode AFM always resulted in removal of the worm-like structure, leaving a surface with a topography similar to pristine graphene. On the other hand, when imaging a hydrogenated flake exclusively in TappingMode, the worm-like structure on the surface of the flake always remained present and never got altered during TappingMode AFM imaging.

Regarding the nature of the worm-like surface structure, an interesting feature can be seen in the middle of Fig. 7.5, on the left side. At the border of the flat, contact mode AFM scanned region and the bottom region, that was exclusively

imaged in TappingMode, white hillocks can be seen. These hillocks are only seen adjacent to areas that have been imaged in contact mode AFM. Therefore, we conclude that they consist of the material that has previously formed the worm-like adsorbate structure on the hydrogenated graphene. Note, that the area that has been scanned in contact mode AFM shows no damage, like holes etc. Thus, the white hillocks are not made up out of graphene. Judging from this observation, we conclude that the worm-like surface structure of hydrogenated graphene is due to an adsorbate layer on the surface.

A possible explanation for the observed adsorbate removal might lie in the operational principle of the two different AFM-imaging modes. In contact mode AFM, the AFM tip is in permanent contact with the sample during scanning. Additionally to pressing perpendicular onto the sample surface while scanning, the AFM tip also exerts lateral forces on the sample. This lateral forces are a strong candidate for eventually removing the adsorbates present on the surface of hydrogenated graphene flakes. The case is different for TappingMode AFM imaging, since here the AFM-tip is only in point-wise contact with the sample, and hence only exerts forces perpendicular to the sample surface, for a small amount of time. Because in TappingMode AFM no change in the structure present on the surface of hydrogenated graphene samples is observed, the lateral forces, which are absent when imaging in TappingMode AFM, seem to be most likely responsible for the removal of the adsorbates.

This explanation can be further supported by the fact that in both AFM imaging modes cantilevers of the same material (Silicon) have been used. This would exclude the effect related to a chemical interaction between the AFM tip material and the surface of hydrogenated graphene. If an exclusive chemical interaction would be responsible for the removal of the adsorbate structure, it should be observed whenever Silicon tips would be used for AFM-imaging of the surface of hydrogenated graphene.

Because of the observed change in the surface structure of hydrogenated graphene, i.e. the apparent removal of the worm-like structure, after imaging in contact mode AFM, the question arose, whether the hydrogen bound to the graphene lattice was removed as well, and pristine graphene was restored. Since Raman spectroscopy can be used to distinguish pristine graphene from hydrogenated graphene, judging from the appearance or absence of the D-peak at 1342 cm^{-1} [11], we chose this technique to investigate our question.

7.1.1 Raman spectroscopy of AFM-scratched hydrogenated graphene

Fig. 7.7 shows Raman spectra taken on a hydrogenated graphene flake (the same flake that is shown in Fig. 7.5) after successively scratching the same area of the hydrogenated flake with increasing the loading force for each scratching. Before
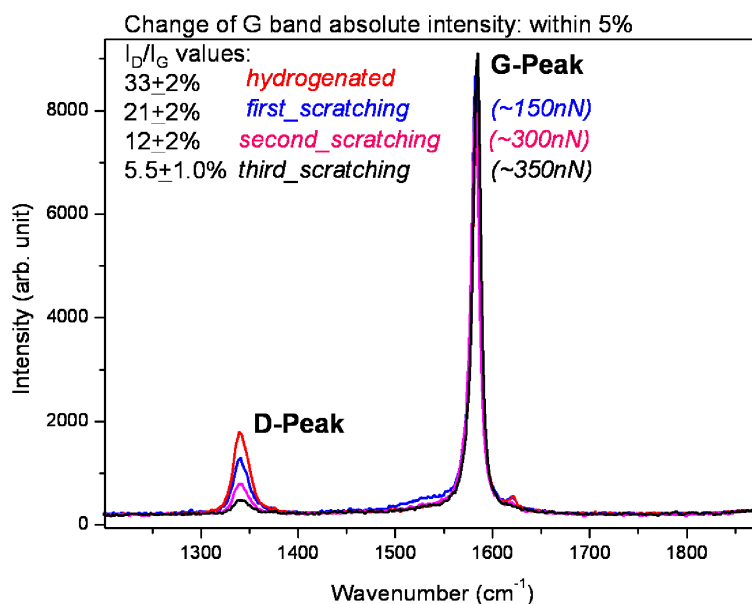
Figure 7.7: Raman spectra of hydrogenated graphene being scratched with contact mode AFM using increasing loading forces. The spectra were taken at an excitation wavelength of 514 nm and using low power. Red curve: The intensity ratio I_D/I_G of D-peak intensity over G-peak intensity is 33%. Blue curve: After AFM scratching with a load of 150 nN, the ratio I_D/I_G decreased to 21%. Magenta curve: Scratching the same area as for the blue curve, but with increased load of now 300nN, decreases the ratio further to 12%. Black curve: One more scratching of the same area, with now 350 nN, decreases I_D/I_G even further to 5.5%. For all four spectra shown, the variation of G-peak intensity is within 5%.

hydrogenating the flake, we took a Raman spectrum on the pristine graphene flake and found no apparent D-peak. The red curve shown is a Raman spectrum taken on a part of the hydrogenated graphene flake that was exclusively imaged in TappingMode-AFM, and that was never imaged in contact mode AFM. It corresponds to the area marked with the red square in Fig.7.5. A prominent D-peak can be seen, around 1350 cm^{-1}, with an intensity ratio of I_D/I_G=33% (comparing the intensity of the D-peak relative to the intensity of the G-peak). This comparison is justified by the fact that the variation in the total intensity

of the G-peak is within only 5%.

The blue curve was taken on an area that was imaged in contact mode AFM, corresponding to the area indicated by the blue square in Fig. 7.5. Scratching of this area was performed at a loading force of around 150nN. [4] For this particular area, the ratio of D-peak intensity over G-peak intensity was found to be only 21%, about 10% less than for the previous area. Afterwards, we scratched the area where the blue curve was taken again, this time using a loading force of 300nN. Then, we took again a Raman spectrum of this area, that was now scratched twice. This second Raman spectrum is displayed as the magenta curve, and an intensity ratio of D-peak intensity over G-peak intensity of now only 12% was extracted. Finally, we scratched the same area a third time, this time applying a loading force of 350nN to the particular sample area. The corresponding Raman spectrum, that was taken immediately after contact AFM scratching, is shown in Fig. 7.7 as the black curve. The intensity of the D-peak signal has decreased even further, and the intensity ratio of D-peak signal over G-peak signal now amounts to be only 5.5%. For all the Raman measurements after each contact AFM scratching step, we took Raman spectra both at the scratched area and the unscratched area, i.e. the area that got imaged exclusively in TappingMode AFM. The Raman spectra taken for the latter area of the sample (unscratched) were found to be virtually the same as the red curve in Fig. 7.7.

The measurements just described confirm that scanning a hydrogenated graphene flake in contact mode AFM, using a high loading force on the cantilever, leads to a reduction of the D-peak in the Raman spectrum of the hydrogenated graphene flake. For the measurements shown in Fig. 7.7, the Raman G-band varied only within 5% for all spectra shown, whereas the D-peak decreases for each loading force by about 10%. Thus, we conclude that hydrogen is removed, and the hydrogenated graphene flake is converted back towards pristine graphene. Furthermore, these results lead to the conclusion that the worm-like surface structure of hydrogenated graphene measured in AFM is an adsorbate, rather than the intrinsic structure of hydrogenated graphene. If the worm-like surface structure,

---

[4]From now on, I will use the term scratching, when talking about scanning a hydrogenated graphene flake repeatedly in contact mode AFM (probe velocities of 12 μm/s) with comparably high loading forces of the AFM tip (larger than 50 nN). Repeated scanning was performed by scanning the sample three times under one scan angle, and scanning the same area of the sample three times perpendicular to the first scan angle.

as shown in Figs. 7.3, 7.4, were the intrinsic structure of hydrogenated graphene, then the complete absence of this structure after AFM scratching should coincide with a complete disappearance of the Raman D-peak. This behavior is clearly not observed.

But taking into account the experimental procedure of repeatedly scratching the same area with an increase in loading force for every scratching performed, we are yet not able to directly assign the removal of hydrogen to either repeated application of AFM scratching or to the increase in loading force that is applied to the hydrogenated graphene flake in each scratching step. Thus, we hydrogenated another single layer graphene flake according to the procedure given above. But now, for scratching the flake in contact mode AFM for the first time, we've selected two different areas of the hydrogenated flake, which were scratched with two different loading forces. After contact AFM scratching, these two scratched areas, as well as the unscratched part of the hydrogenated flake were investigated using Raman spectroscopy. The results are shown in Fig. 7.8. The images (a), (b) and (c) are optical microscopy images, taken with $50\times$ magnification, of the hydrogenated graphene flake on top of an oxidized silicon wafer. The hydrogenated single layer graphene flake can be seen in the middle of the image, with a slightly darker color than the surface of the oxidized silicon wafer (left to the graphene flake).

In (d), three different Raman spectra are shown (the Raman spectrum for the same graphene flake before hydrogenation is shown in Chapter 1 and shows no apparent D-peak). The red curve corresponds to the unscratched hydrogenated graphene flake. In the optical image, Fig. 7.8(a), the area where this spectrum was obtained (the position of the laser spot) is indicated by the intersection of the horizontal and vertical line. The Raman intensity of the D-peak relative to the G-peak for this area was found to be 66%. The blue curve in (d) is a Raman spectrum taken on an area that was scratched with 150nN. The position were this Raman spectrum was taken is indicated in Fig. 7.8(b). The intersection of the horizontal and vertical line lie within a square-shaped region, the region that was scratched in contact AFM, whose borders are faintly visible as light-blue lines. The ratio of D-peak intensity over G-peak intensity for this particular area is found to be 35%, half the value compared to the unscratched hydrogenated graphene flake. Finally, the black curve in (d) is a Raman spectrum taken at an area of the hydrogenated graphene flake that was scratched with a loading
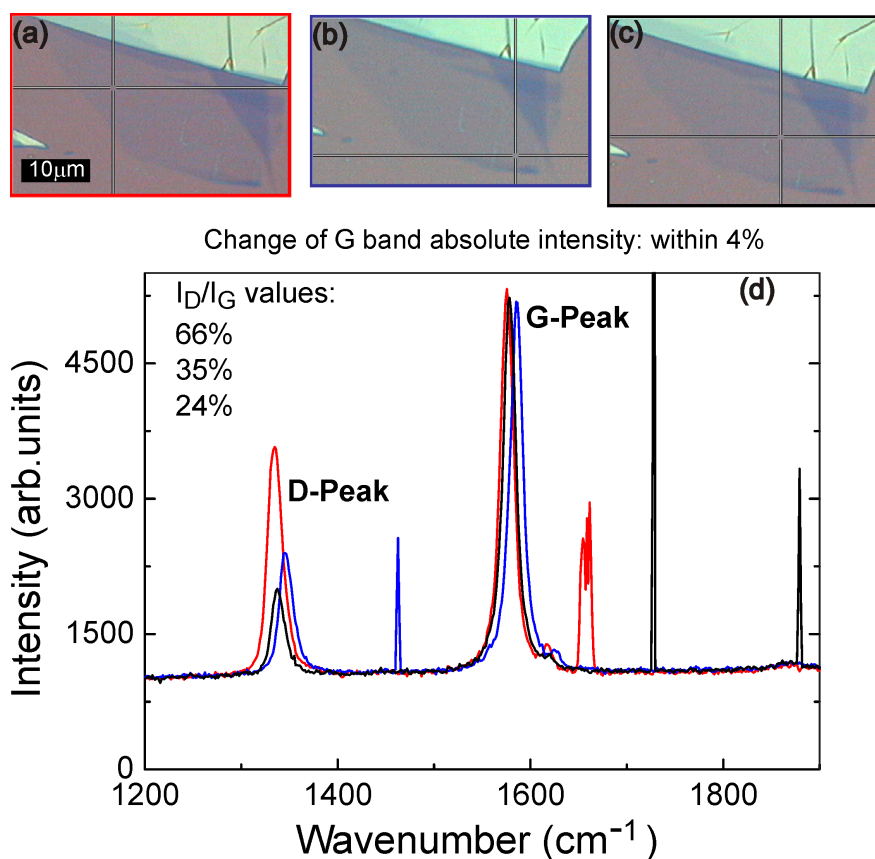
Figure 7.8: (a, b, c) 50× magnification optical images of a hydrogenated graphene flake (middle) on silicon oxide (left and bottom). The intersection of the vertical and horizontal line indicates the position where the Raman spectrum was taken. (d) Raman spectra taken on the positions indicated in (a, b, c), at an excitation wavelength of 514 nm at low power. Red curve: Spectrum taken at (a), unscratched hydrogenated graphene. I_D/I_G is 66%. Blue curve: Spectrum taken at (b), an area of the hydrogenated graphene flake that was scratched with 150 nN. I_D/I_G has decreased to 35%. Black curve: Spectrum taken at (c), an area that was scratched with 200nN. I_D/I_G decreased even further to 24%.

force of around 200 nN. The position where this Raman spectrum was obtained is indicated in Fig. 7.8(c). Again, the intersection of the horizontal and vertical line lie within a square shaped region with faintly visible light-blue borders. The ratio for D-peak intensity over G-peak intensity is now found to be only 24%, almost a third compared to the unscratched hydrogenated graphene flake.

Again, since the variation of G-peak intensity is within 4% for all three Raman spectra, we can conclude that hydrogen is removed, and that the hydrogenated graphene flake is transformed back towards pristine graphene. This first of all confirms our results presented in the first part of this section. Secondly, since this time we scratched two completely different areas of the same hydrogenated graphene flake, we can conclude that an increase in loading force leads to an increase in the reduction of the Raman D-peak.

Two questions now come up immediately. First, how much loading force is needed to fully transform hydrogenated graphene back into pristine graphene? Secondly, would repeated scratching of the same area with the same force lead to continous reduction of the Raman D-peak signal over time? These two questions still need to be answered by further experiments. Especially an answer to the first question would be tempting. Given that the loading force needed to fully recover pristine graphene, i.e. reduce the D-peak fully, is still smaller than the loading force at which the hydrogenated graphene sheet will rupture, we would have an easy and straight-forward method at hand to engineer junctions consisting of a hydrogenated graphene/ pristine graphene interface. In this way, novel nanoelectronic devices based on hydrogenated graphene could be made using nanomechanical lithography based on contact mode AFM.

7.1.2 Electric Transport

From the results of the Raman spectroscopy measurements on the scratched hydrogenated graphene flakes, i.e. the reduction of the Raman D-peak, it seems that the hydrogenated graphene is turned back towards pristine graphene. To further study this behavior, electronic transport measurements were performed on hydrogenated graphene flakes that were subsequently scratched in contact mode AFM.

In order to perform electronic transport experiments, graphene flakes on top of an oxidized silicon wafer were equipped with Ti/Au-contacts and etched into

116

a cross-shaped mesa in oxygen plasma. Afterwards, the graphene cross was hydrogenated. A sketch of the cross-shaped sample is shown on the top right of Fig. 7.9. The contacts connecting the hydrogenated graphene flake are labelled 1, 3, 12 and 14, respectively.

After hydrogenation, the sample was cooled down to T=3.7 K, and two-probe measurements of the sample resistance, as the backgate voltage is changed, were performed. In Fig. 7.9 the results of these measurements are shown.

The black curve, labelled R_{1-3} was taken after the first cool down. The label indicates that the sample resistance was measured between contacts 1 and 3 in a two-probe arrangement. The overall shape of the curve resembles that of pristine graphene, with a maximum of the sample resistance as a function of gate voltage at approx. +5 V. This value indicates p-doping, an observation also reported in [11]. The value of the resistance at this gate voltage lies around 3.5 MΩ.

To investigate how scratching the hydrogenated graphene flake by AFM changes the transport properties of the sample, we proceeded in a sequential manner. The cross-shaped device can be thought to consist of five different areas, four being adjacent to the contacts, and one area in the middle of the cross (see inset on the upper right of Fig. 7.9). To start, we scratched the area next to contact 12. After scratching, the device was again cooled down. Now, the two-probe resistance of the sample as a function of gate voltage was measured between contacts 12 and 14, thus probing the resistance of the scratched part adjacent to contact 14. The corresponding curve is colored red in Fig. 7.9 and is labelled R_{12-14}. On the left part in the image, the sketch of the cross is shown (pointed to by an arrow from the respective resistance-gate voltage curve), with the scratched area indicated by a grey rectangle. Compared to the black curve measured initially, the maximum resistance is still found at a gate voltage close to +5 V, but the resistance at that voltage has dropped by almost a factor of two, now being around 1.8 MΩ. For comparison, the green curve represents the two-probe measurements of the sample resistance between the contacts 1 and 3, where no AFM scratching has been performed. The green curve is almost similar to the black one, indicating that the sample hasn't changed much in the unscratched areas. Only a shift of the neutrality point (NP) to +4 V is observed.

In the next step, the area of the device next to contact 14 was scratched with AFM. After cooling the sample down, the resistance as a function of back gate voltage was again measured between contacts 12 and 14. This measurement is
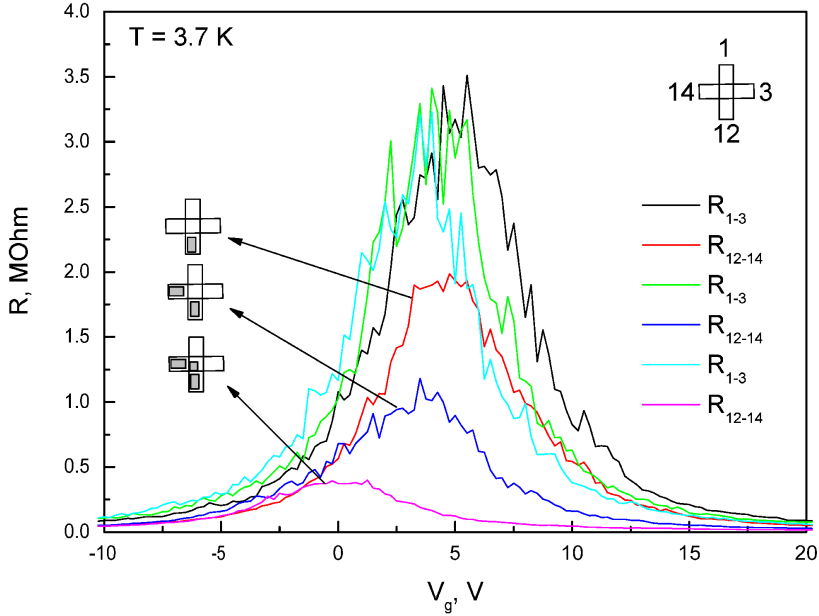
Figure 7.9: Two-probe measurements of resistance vs. backgate voltage of hydrogenated graphene as the cross-shaped sample is successively scratched. Black curve: Initial resistance between contacts 1 and 3 (drawing in the upper right), with a maximum value of 3.5 MΩ, and a neutrality point (NP, gate voltage for maximum resistance) of about +5 V, indicating p-doping. Red curve: Resistance between contacts 12 and 14, after the area close to contact 12 had been scratched (grey area in the sketch on the left). The maximum resistance drops by a factor of 2 compared to the black curve. Green curve: Resistance between contacts 1 and 3, measured after the red curve. Same maximum resistance as in black curve, shift of NP towards zero by 1 V. Blue curve: Resistance between contacts 12 and 14, after additionally the area close to contact 14 had been scratched. The maximum resistance has now dropped by a factor of 4 compared to the black or green curve. The NP has shifted closer to 0 V. Light-blue curve: Resistance between contacts 1 and 3, measured after the blue curve. No change in the maximum sample resistance. Compared to the green curve, the NP has shifted to 3 V. Magenta curve: Resistance between contacts 12 and 14 after the area in the middle of the cross was scratched as well. The maximum resistance drops to 350 kΩ, a factor of 10 compared to the black, green or light-blue curve. Additionally, the neutrality point is shifted to 0 V, as expected for pristine graphene. (*Data courtesy of Alexander Mayorov, University of Manchester.*)

displayed as the blue curve. An arrow points to the sketch of the cross on the left, where now two scratched areas, indicated by grey rectangles, can be seen. With two areas being scratched, the maximum of the sample resistance dropped down by a factor of two again when compared to the red curve, to a value of about 1 MΩ. Again, the resistance of the unscratched part, between contacts 1 and 3, of the cross-shaped device was measured for comparison. It corresponds to the light-blue curve, labelled R_{1-3} on the left. Compared to the previous measurements (black curve and green curve) of the sample resistance versus gate voltage of that part of the sample, again almost no change is visible. The maximum of the resistance is found again to be around 3.5 MΩ, only a further shift in the gate voltage position of this resistance peak towards zero gate voltage can be seen. It now lies at +3 V.

Finally, the middle part of the cross-shaped device was scratched, and afterwards the resistance was measured at low temperatures. The resistance versus gate voltage curve measured between contacts 12 and 14 for that last experiment is shown in Fig. 7.9 by the magenta curve (the arrow from that curve pointing to the sketch of the sample indicating the scratched areas by grey rectangles). Apparently, this last curve has the lowest maximum resistance of all curves measured in this experiment, being about 350 kΩ. Furthermore, the maximum resistance is found at 0 gate voltage.

Compared to the two-probe resistance of the hydrogenated, unscratched device, as measured between contacts 1 and 3 and being represented by the black, green and light-blue curves two major results were obtained. First of all, the resistance of the hydrogenated unscratched device was reduced by a factor of 10, from initially 3.5 MΩ to 350 kΩ, by scratching the entire area through which the current is flowing in the two-probe transport measurements. Secondly, the position of the resistance maximum as a function of gate voltage changed for this part of the sample from +5 V to about 0 V, starting from the hydrogenated and unscratched sample, and finishing when the entire area where the two-probe resistance was measured was being scratched.

The observed behavior indicates that scratching a hydrogenated single layer graphene device leads to recovery of the electronic transport properties of pristine graphene. In that sense the transport measurements complement and corroborate our findings from Raman spectroscopy (the reduction in D-peak signal with scratching the hydrogenated graphene flake using contact mode AFM) in terms of

119

observing a release of hydrogen and thus piecewise recovery of the characteristics of pristine graphene. Further electronic transport studies could be made to investigate the effect of increasing the load when scratching hydrogenated graphene. For this scenario, I would expect an even stronger appearance of pristine graphene characteristics, namely a further decrease of the maximum resistance, as Raman spectroscopy shows a further decrease in D-peak for increasing the loading force when scratching.

7.2 Mechanism responsible for hydrogen removal by AFM-scratching

Given the experimental observations presented in this chapter, several questions still remain to be answered. First of all, the mechanism responsible for hydrogen removal by scratching the hydrogenated graphene flakes with contact mode AFM needs to be established. Once this mechanism is understood, one would have to consider, whether it is possible to fully recover pristine graphene from hydrogenated samples by AFM-scratching.

Several mechanisms can in principle lead to a removal of the hydrogen atoms from the graphene lattice using atomic force microscopy.

One possibility would be a chemical process occurring between the AFM tip and hydrogenated graphene. To investigate this, AFM scratching of hydrogenated graphene was performed using Diamond-coated tips. Unfortunately, it turned out that Diamond-coated tips mechanically destroy (slashing) the hydrogenated graphene flake very easily. The range of loading forces that could be applied to Diamond-coated tips operated in contact mode thus was too small to conduct the AFM scratching experiment under the same conditions used for AFM scratching with Silicon tips, i.e. applying the same loading forces.

Another point regarding the possibility of a chemical reaction between AFM tip and sample is the observation that during TappingMode AFM investigations using Silicon tips no change of the surface structure of hydrogenated graphene was observed. Although in TappingMode AFM the tip only experiences contact with the sample for a very short period of time, if a chemical reaction would occur between tip and sample one would at least expect minor changes in the surface structure. However, no such changes were observed.

A second possible mechanism for the removal of hydrogen by AFM scratching is the local straining of the hydrogenated graphene flake while the AFM tip is scanned in contact over the sample. One would expect that a higher loading force of the tip would result in a larger area of contact between AFM tip and sample [99]. If the AFM tip now gets dragged across the surface, the flake underneath might be deformed, hence locally straining the hydrogenated graphene flake. Dependent on the particular local shape of the hydrogenated flake being scanned, it might be energetically favorable for the flake to release the hydrogen. The idea of a specific local surface curvature being essential for the bonding of hydrogen to the graphene lattice was already put forward in the paper of Elias [11]. There it is argued that the intrinsically rippled surface of graphene [100], leading to convex shapes, facilitates the bonding of hydrogen to a Carbon atom. It was shown that single-sided hydrogenation of ideal graphene would create a material that is thermodynamically unstable [101] [102]. If hydrogen gets attached to a Carbon atom, it is expected that an sp^3-bond forms, with angles of 110° between all of the bonds [101]. To achieve this, the initially sp^2-hybridized Carbon atoms have to move out of the plane in the direction of the attached hydrogen, at the cost of an increase in elastic energy. However, for a convex surface, the lattice is already deformed in the direction that favors sp^3 bonding, which lowers the total energy. In [11] it has been shown that single-sided hydrogenation of graphene becomes favorable for a typical size of ripples observed experimentally [100].

Examining this argument, we investigated whether the Raman D-peak of a hydrogenated graphene crystal changes under strain. A single layer graphene flake placed on top of a macroscopic PMMA bar was hydrogenated and subsequently characterized by Raman spectroscopy. Afterwards, the PMMA bar was bent and the induced strain was estimated to be 1%. Nevertheless, although the PMMA bar was left bent for several weeks, no change in the Raman D-peak signal was observed during that time. Regarding this particular experiment, a limiting factor might be that the hydrogenated graphene flake on a bent PMMA bar is subject to uniaxial strain alone. To finally prove the assumption, whether mechanical strain can lead to a release of hydrogen and thus transform hydrogenated graphene back to its pristine state, membranes consisting of hydrogenated graphene have to be investigated. The idea of this experiment is to have hydrogenated graphene covering circular holes in a substrate. Then, these membranes have to be indented

by pressing the tip of an AFM into them. The resulting deflection of the membrane induces an isotropic mechanical strain. After the AFM indentation, the corresponding hydrogenated membranes have to be investigated using Raman spectroscopy.

A third possible mechanism leading to a release of hydrogen could be heating of the hydrogenated sample due to the friction occuring between the AFM tip and the area of the sample being scanned in contact mode. Friction can dissipate as heat, and could thus lead to a local annealing of the sample. The effect of annealing would then lead to the removal of hydrogen and recovering pristine graphene, in the same way as it was already reported [11]. The only difference would be that this possible local annealing could be adjusted by the amount of normal force exerted by the AFM tip onto the sample surface (an increase in loading force leads to a larger area of contact between tip and sample, and hence to higher friction).

7.3   Conclusions and Outlook

Hydrogenated graphene was produced following the method of Elias et al. [11]. After careful inspection with Raman spectroscopy, the hydrogenated samples were scratched using contact mode AFM. Scratching was done scanning a selected area of the hydrogenated graphene flake while applying a high loading force. Subsequently, the samples scratched in this way were investigated again using Raman spectroscopy. Compared to the Raman spectra taken before the AFM scratching, the samples now show a strong reduction of the D-peak Raman signal at 1350 cm^{-1} compared to the G-peak Raman signal at 1580 cm^{-1}. These findings indicate that during AFM scratching, the hydrogenated graphene flakes were partially transformed back into pristine graphene. To further test this hypothesis, electronic transport measurements were conducted at low temperatures. To that end, the area between two contacts of a cross-shaped hydrogenated device was piecewise scratched until the full area between these contacts was scratched. The two-probe resistance between these two contacts was measured at 3.7 K after each scratching step. To be able to directly evaluate the effect of AFM scratching, the

area between the two other contacts of the cross-shaped sample remained completely untouched by contact mode AFM. The resistance of the sample between these two contacts was likewise measured between the scratching steps. We found that after scratching, the two-probe resistance has dropped by a factor of 10 compared to the fully unscratched area. Furthermore, the resistance maximum of the sample shifted to 0 V in gate voltage after the entire area for which the resistance was measured was being completely scratched. These findings of the transport measurements strengthen our hypothesis that hydrogenated graphene is transformed towards pristine graphene when scratching it in contact mode AFM.

While the experimental evidence is given that scratching hydrogenated graphene transforms the hydrogenated crystal partially back into its pristine state, the mechanism responsible for this behavior is still unknown. Furthermore, it is unclear whether the hydrogenated graphene can be fully converted back to pristine graphene. With knowledge of these two quantities, AFM-scratching would offer a simple and straight-forward method to fabricate nanoelectronic devices consisting of areas showing insulating behavior and semimetallic behavior.

Chapter 8

Summary and directions for future work

This thesis was mainly concerned with scanning probe investigations on graphene. Both, atomic force microscopy (AFM) and scanning tunnelling microscopy (STM), have been used to characterize and manipulate graphene and hydrogenated graphene crystals. In order to allow for STM experiments, a low-noise, vibration-isolation measurement setup has been designed and built up. Additionally, Raman spectroscopy experiments are reported, which were used for characterization of the samples studied, as well as for obtaining complementary information regarding the scanning probe experiments.

The first original result that has been obtained in the framework of this thesis is the local electrochemical modification of graphene, using scanning probe lithography (SPL). While it soon became clear that with confining graphene to nanometre sizes a band gap is opened, at the time of our experiments the only feasible approach was based on electron beam lithography with subsequent plasma etching. The work presented showed for the first time that the same geometric confinement can be achieved by applying a voltage between a conductive AFM tip and a grounded graphene sample in a humid atmosphere. This approach has the advantage of achieving the same feature sizes, but without inducing possible contamination of the sample by using resists. After establishing the working principle, the characterization of this new lithographic approach in terms of resolution and dependence on the process parameters, such as the applied bias voltage, has been performed. Furthermore, examples of graphene nanostructures fabricated using this technique were given. However, it remains for future work to specify

the exact chemical nature of the areas on graphene that were oxidized. Sometimes these areas appear as depressions, indicating that graphene was etched away completely, which is expected in the case of the oxidation of graphene. But the oxidized areas can also show as protrusions. These protrusions are up to 1-2 nm high above the graphene surface, but their chemical nature is still unclear.

The next major finding achieved in this work was the successful observation of quantum Coulomb blockade behavior in a quantum dot structure fabricated in graphene using scanning probe lithography. Electronic transport measurements carried out at low temperatures clearly revealed that quantum Coulomb blockade occurs in these devices. It is shown that from the temperature dependence of the conductance minima between the conductance peaks and from the charge stability diagram, the so-called Coulomb diamonds, an energy gap for our devices of about 10 meV can be extracted. This was the first demonstration of a working graphene quantum dot device fabricated by AFM-based lithography.

A further proof of the insulating behavior of the regions in graphene that were being oxidized using SPL was then given by conducting scanning gate microscopy experiments on a graphene quantum point contact. A graphene quantum point contact (QPC) was defined using our SPL technique. When scanning a biased conductive AFM tip across the sample, the electric field at the AFM tip changes the charge carrier concentration underneath the tip in the sample, and hence the conductance through the sample. In the scanning gate experiments performed, a clear change in the sample conductance was observed only at the tip position where the quantum point contact was formed. At all other tip positions across the sample, no significant change in the sample conductance was observed. This clearly demonstrates that the lines oxidized in graphene are insulating and efficiently confined the graphene flake to a region resembling a quantum point contact. If the oxidized lines were not insulating, no change in the conductance through the sample at the position of the quantum point contact would have been observed at all. Additionally, this experiment successfully demonstrates that local electrostatic gating of graphene nanostructures can be achieved under ambient conditions using a biased AFM tip. Further studies can be conducted, examining either the influence of the geometry of the graphene nanostructure on the observed changes in conductance, and/or investigating the response of the nanostructure as a function of the applied tip bias voltage.

The edges terminating graphene crystals are of crucial importance for fundamental and application oriented research. The idea has been put forward that these edges might follow crystallographic orientations of the underlying honeycomb crystal lattice, namely being either of armchair or of zigzag orientation. Although Raman spectroscopy can be used to distinguish one crystallographic edge type from another, it requires modelling to be applied. In the work presented here, it was shown how atomically resolved real space images of the graphene honeycomb lattice, obtained by scanning tunnelling microscopy (STM), could be used to prove the hypothesis that the terminating edges follow a crystallographic orientation. Furthermore, the results obtained by STM validate the interpretation of the Raman spectroscopy experiments, as was shown by Raman spectra taken on edges of the same graphene crystal being imaged in high resolution STM.

While so far scanning probe microscopy experiments have been carried out on pristine graphene crystals, in the last part of the work presented investigations on a chemically modified graphene crystal were shown. The exposure of pristine graphene to atomic hydrogen leads to the formation of so-called hydrogenated graphene, in which portions of the Carbon atoms present in the pristine crystal form sp^3-bonds with hydrogen. While this material has been studied initially with Raman spectroscopy, low temperature electronic transport measurements and transmission electron microscopy (TEM), no information on the real-space topographic structure of hydrogenated graphene was available. Hence, Tapping Mode AFM investigations were performed, which showed that a characteristic structure had been formed after treatment of the graphene crystals with atomic hydrogen. By investigating the same sample with contact mode AFM, it was found that this surface structure appears to be an adsorbed layer on top of the hydrogenated graphene crystal, rather than being the intrinsic structure of hydrogenated graphene. The latter conclusion could be drawn from performing Raman spectroscopy on the same samples, which have been imaged in both Tapping Mode AFM and contact mode AFM. While the characteristic signature for hydrogenated graphene, the so-called D-peak, was reduced after scanning the samples in contact mode AFM, it was still present, and much larger than in the pristine graphene sample.

This reduction of the intensity of the D-peak (when compared to the intensity of the G-peak) upon scanning the sample in contact mode AFM was then

further investigated. The interest in the observed behavior lies in the fact, that contact mode AFM might offer a versatile way of transforming hydrogenated graphene back towards its pristine state, and thus engineer the resistance of graphene/hydrogenated graphene. To this end it was found and established that an increasing force, with which the hydrogenated graphene is being scanned in contact mode AFM, leads to an increased reduction in the ratio of D-peak intensity over G-peak intensity. The origin of this phenomena is not clear, and further experiments have to be conducted in order to clarify the mechanism responsible for the hydrogen removal.

Further research directions are suggested by the work presented in Chapters 3, 4 and 5. The local anodic oxidation of graphene has enabled us to fabricate nanoelectronic devices. A next step would be the replacement of water by a different electrolyte. The goal of this experiment would be the local functionalization of graphene, i.e. covalently attaching molecular species to the graphene scaffold. Since covalent bonded species, such as chemisorbed hydrogen, are effectively a defect in the sp^2-bonded graphene lattice, we should be able to detect the functionalization by using Raman spectroscopy. After establishing the chemical modification of the graphene lattice, the task would be to attach these molecules in a way resulting in an ordered structure. Afterwards, the electronic transport properties of the resulting structure have to be investigated.

Building on the work presented in the last chapter of this thesis, one could think of using scanning tunnelling microscopy to achieve atomically resolved images of chemically functionalized graphene. This might allow for an atomically resolved determination of how the atoms or molecules attach to graphene. The first candidate for these investigations would be hydrogenated graphene. Having established the possibility of removing hydrogen with contact mode AFM, it would be interesting to see, how atomically resolved images differ regarding the amount of hydrogen that was removed. As shown, the degree of hydrogen removal can be monitored using Raman spectroscopy. Atomically resolved images showing a variation of the hydrogen coverage could be very useful in establishing a quantitative relationship between the intensity of the defect-related Raman signal to the actual amount of defects being present.

Bibliography

[1] K. S. Novoselov, A. K. Geim, S. V. Morozov, D. Jiang, Y. Zhang, S. V. Dubonos, I. V. Grigorieva and A. A. Firsov. *Science*, 306:666, 2004.

[2] K. S. Novoselov, D. Jiang, F. Schedin, T. J. Booth, V. V. Khotkevich, S. V. Morozov and A. K. Geim. *PNAS*, 102:10451, 2005.

[3] A. K. Geim and K. S. Novoselov. *Nature Mat.*, 6:183, 2007.

[4] K. S. Novoselov, A. K. Geim, S. V. Morozov, D. Jiang, M. I. Katsnelson, I. V. Grigorieva, S. V. Dubonos and A. A. Firsov. *Nature*, 438:197, 2005.

[5] A. K. Geim. *Science*, 324:1530, 2009.

[6] C. Lee, X. Wei, J. W. Kysar, and J. Hone. *Science*, 321:385, 2008.

[7] A. A. Balandin, S. Ghosh, W. Bao, I. Calizo, D. Teweldebrhan, F. Miao, and C. N. Lau. *Nano Lett.*, 8:902, 2008.

[8] V. M. Pereira, A. H. Castro Neto, and N. M. R. Peres. *Phys. Rev. B*, 80:045401, 2009.

[9] F. Xia, T. Mueller, Y.-M. Lin, A. Valdes-Garcia, and P. Avouris. *Nature Nano*, 4:839, 2009.

[10] S. Bae, H. Kim, Y. Lee, X. Xu, J.-S. Park, Y. Zheng, J. Balakrishnan, T. Lei, H. R. Kim, Y. I. Song, Y.-J. Kim, K. S. Kim, B. Özyilmaz, J.-H. Ahn, B. H. Hong, and S. Iijima. *Nature Nano*, nnano.2010.132:10.1038, 2010.

[11] D. C. Elias, R. R. Nair, T. M. G. Mohiuddin, S. V. Morozov, P. Blake, M. P. Halsall, A. C. Ferrari, D. W. Boukhvalov, M. I. Katsnelson, A. K. Geim and K. S. Novoselov. *Science*, 323:610, 2009.

[12] G. Binnig, H. Rohrer, Ch. Gerber, E. Weibel. *Phys. Rev. Lett.*, 49:57, 1982.

[13] G. Binnig, C. F. Quate, Ch. Gerber. *Phys. Rev. Lett.*, 56:930, 1986.

[14] E. Meyer, H. J. Hug and R. Bennewitz. *Scanning Probe Microscopy - The Lab on a Tip.* Springer-Verlag Berlin Heidelberg New York, 2004.

[15] P. Dietl. Master's thesis, Universität Karlsruhe, 2009.

[16] R. Saito, G. Dresselhaus and M. S. Dresselhaus. *Physical Properties of Carbon Nanotubes.* Imperial College Press, London, 1998.

[17] U. D. Schwarz, P. Köster and R. Wiesendanger. *Rev. Sci. Instr.*, 67:2560, 1996.

[18] A. Opitz. PhD thesis, TU Ilmenau, 2003.

[19] Ch. Loppacher. PhD thesis, Universität Basel, 2000.

[20] G. Binnig, H. Rohrer, Ch. Gerber and E. Weibel. *Phys. Rev. Lett.*, 49:57, 1982.

[21] R. H. Fowler and L. Nordheim. *Proc. Roy. Soc. A*, 119:173, 1928.

[22] C. Julian Chen. *Introduction to Scanning Tunneling Microscopy.* Oxford University Press Inc., New York, 2008.

[23] R. H. Fowler and L. Nordheim. *Phys. Rev. Lett.*, 6:57, 1961.

[24] J. Tersoff and D. R. Hamann. *Phys. Rev. Lett.*, 50:1998, 1983.

[25] J. Tersoff and D. R. Hamann. *Phys. Rev. B*, 31:805, 1985.

[26] D. W. Pohl. *IBM J. Res. Dev.*, 30:417, 1986.

[27] Digital Instruments. *Scanning Probe Microscopy Training Notebook Version 3.0*, 2000.

[28] P. Blake, K. S. Novoselov, A. H. Castro Neto, D. Jiang, R. Yang, T. J. Booth, A. K. Geim, E. W. Hill. *Appl. Phys. Lett.*, 91:063124, 2007.

[29] M. Ishigami, J. H. Chen, W. G. Cullen, M. S. Fuhrer, E. D. Williams. *Nano Lett.*, 7:1643, 2007.

[30] Frank Freitag. *private communication*, 2009.

[31] S. M. Song and B. J. Cho. *Nanotechnology*, 21:335706, 2010.

[32] A. C. Ferrari, J. C. Meyer, V. Scardaci, C. Casiraghi, M. Lazzeri, F. Mauri, S. Piscanec, D. Jiang, K. S. Novoselov, S. Roth and A. K. Geim. *Phys. Rev. Lett.*, 97:187401, 2006.

[33] M. Y. Han, B. Özyilmaz, Y. Zhang, and P. Kim. *Phys. Rev. Lett.*, 98:206805, 2007.

[34] L. A. Ponomarenko, F. Schedin, M. I. Katsnelson, R. Yang, E. W. Hill, K. S. Novoselov, A. K. Geim. *Science*, 320:356, 2008.

[35] C. Stampfer, J. Güttinger, F. Molitor, D. Graf, T. Ihn, K. Ensslin. *Appl. Phys. Lett.*, 92:012102, 2008.

[36] B. Özyilmaz, P. Jarillo-Herrero, D. Efetov, and P. Kim. *Appl. Phys. Lett.*, 91:192107, 2007.

[37] E. Snow and P. M. Campbell. *Appl. Phys. Lett.*, 64:1932, 1994.

[38] E. Snow, D. Park, and P. M. Campbell. *Appl. Phys. Lett.*, 69:269, 1996.

[39] T. R. Albrecht, M. M. Dovek, M. D. Kirk, C. A. Lang, C. F. Quate, and D. P. E. Smith. *Appl. Phys. Lett.*, 55:1727, 1989.

[40] M. Ishii and K. Matsumoto. *Jpn. J. Appl. Phys.*, 34:1329, 1995.

[41] R. Held, T. Vancura, T. Heinzel, K. Ensslin, M. Holland, and W. Wegscheider. *Appl. Phys. Lett.*, 73:262, 1998.

[42] A. J. M. Giesbers, U. Zeitler, S. Neubeck, F. Freitag, K. S. Novoselov, and J. C. Maan. *Solid State Comm.*, 147:366, 2008.

[43] S. Masubuchi, M. Ono, K. Yoshida, K. Hirakawa, and T. Machida. *Appl. Phys. Lett.*, 94:082107, 2009.

[44] L. Weng, L. Zhang, Y. P. Chen, and L. P. Rokhinson. *Appl. Phys. Lett.*, 93:093107, 2008.

[45] S. Neubeck, L. A. Ponomarenko, F. Freitag, A. J. M. Giesbers, U. Zeitler, S. V. Morozov, P. Blake, A. K. Geim, and K. S. Novoselov. *Small*, 6:1469, 2010.

[46] J. A. Dagata. *Fundamental science and lithographic applications of scanning probe oxidation In S. Kalinin A. Gruverman, editor, Scanning Probe Microscopy, volume II.* Springer New York, 2007.

[47] H. Seidel, L. Csepregi, A. Heuberger, and H. Baumgärtel. *Journ. Electrochem. Soc.*, 137:3612, 1990.

[48] H.-S. Choo, T. Kinumoto, S.-K. Jeong, Y. Iriyama, T. Abe, and Z. Ogumia. *J. Electrochem. Soc.*, 154:B1017, 2007.

[49] L. P. Kouwenhoven, C. M. Marcus, P. L. McEuen, S. Tarucha, R. M. Westervelt, N. S. Wingreen. *Electron Transport in Quantum Dots, In L. L. Sohn, L. P. Kouwenhoven and G. Schön, Eds., Mesoscopic Electron Transport.* Kluwer Academic Publishers, NATO Series E345, Dordrecht, 1997.

[50] L. P. Kouwenhoven, N. C. van der Vaart, A. T. Johnson, W. Kool, C. J. P. M. Harmans, J. G. Williamson, A. A. M. Staring, C. T. Foxon. *Z. Phys. B*, 85:367, 1991.

[51] U. Meirav, M. A. Kastner, S. J. Wind. *Phys. Rev. Lett.*, 65:771, 1990.

[52] Y. Meir, N. S. Wingreen, P. A. Lee. *Phys. Rev. Lett.*, 66:3048, 1991.

[53] C. W. J. Beenakker. *Phys. Rev. B*, 44:1646, 1991.

[54] www.grafite.com.

[55] Y. Zhang, J. W. Tan, H. L. Stormer, P. Kim. *Nature*, 438:201, 2005.

[56] I. M. Ruzin, V. Chandrasekhar, E. I. Levin, L. I. Glazman. *Phys. Rev. B*, 45:13469, 1992.

[57] L. Yang, C. H. Park, Y. W. Son, M. L. Cohen, S. G. Louie. *Phys. Rev. Lett.*, 99:186801, 2007.

[58] N. M. R. Peres, A. H. Castro Neto, F. Guinea. *Phys. Rev. B*, 73:195411, 2006.

[59] Z. H. Chen, Y. M. Lin, M. J. Rooks, and P. Avouris. *Physica E*, 40:228, 2007.

[60] F. Molitor, A. Jacobsen, C. Stampfer, J. Güttinger, T. Ihn, and K. Ensslin. *Phys. Rev. B*, 79:075426, 2009.

[61] C. Stampfer, J. Güttinger, S. Hellmüller, F. Molitor, K. Ensslin, and T. Ihn. *Phys. Rev. Lett.*, 102:056403, 2009.

[62] X. Liu, J. B. Oostinga, A. F. Morpurgo, and L. M. K. Vandersypen. *Phys. Rev. B*, 80:121407, 2009.

[63] K. Todd, H.-T. Chou, S. Amasha, and D. Goldhaber-Gordon. *Nano Lett.*, 9:416, 2009.

[64] S. Schnez, J. Güttinger, M. Hüfner, C. Stampfer, K. Ensslin, and T. Ihn. *arXiv*, page 1005.2024v1, 2010.

[65] R. Jalilian, L. A. Jauregui, G. Lopez, J. Tian, C. Roecker, M. M. Yazdan-panah, R. W. Cohn, I. Jovanovic, and Y. P. Chen. *arXiv*, page 1003.5404, 2010.

[66] M. R. Connolly, K. L. Chiou, C. G. Smith, D. Anderson, G. A. C. Jones, A. Lombardo, A. Fasoli, and A. C. Ferrari. *Appl. Phys. Lett.*, 96:113501, 2010.

[67] J. Berezovsky, M. F. Borunda, E. J. Heller, and R. M. Westervelt. *Nanotechnology*, 21:274013, 2010.

[68] S. J. Tans and C. Dekker. *Nature*, 404:834, 2000.

[69] A. Bachtold, M. S. Fuhrer, S. Plyasunov, M. Forero, E. H. Anderson, A. Zettl and P. L. McEuen. *Phys. Rev. Lett.*, 84:6082, 2000.

[70] M. Freitag, A. T. Johnson, S. V. Kalinin and D. A. Bonnell. *Phys. Rev. Lett.*, 89:286801, 2002.

[71] M. Bockrath, W. Liang, D. Bozovich, J. H. Hafner, C. M. Lieber, M. Tinkham and H. Park. *Science*, 291:283, 2001.

[72] S. Stankovich, D. A. Dikin, G. H. B. Dommett, K. M. Kohlhaas, E. J. Zimney, E. A. Stach, R. D. Piner, S. T. Nguyen and R. S. Ruoff. *Nature*, 442:282, 2006.

[73] A. J. van Bommel, J. E. Crombeen and A. van Tooren. *Surface Science*, 48:463, 1975.

[74] C. Berger, Z. Song, T. Li, A. Y. Ogbazghi, R. Feng, Z. Dai, A. N. Marchenkov, E. H. Conrad, P. N. First and W. A. de Heer. *J. Phys. Chem. B*, 108:19912, 2004.

[75] C. Oshima and A. Nagashima. *J. Phys.: Condens. Matter*, 9:1, 1997.

[76] A. Reina, X. Jia, J. Ho, D. Nezich, H. Son, V. Bulovic, M. S. Dresselhaus and J. Kong. *Nano Lett.*, 9:30, 2009.

[77] K. S. Kim, Y. Zhao, H. Jang, S. Y. Lee, J. M. Kim, K. S. Kim, J.-H. Ahn, P. Kim, J.-Y. Choi and B. H. Hong. *Nature*, 457:706, 2009.

[78] R. Piner, A. Velamakanni, I. Jung, E. Tutuc, S. K. Banerjee, L. Colombo and R. S. Ruoff. *Science*, 324:1312, 2009.

[79] P. Blake, P. D. Brimicombe, R. R. Nair, T. J. Booth, D. Jiang, F. Schedin, L. A. Ponomarenko, S. V. Morozov, H. F. Gleeson, E. W. Hill, A. K. Geim and K. S. Novoselov. *Nano Lett.*, 8:1704, 2008.

[80] Y. Hernandez, V. Nicolosi, M. A. Lotya, F. M. Blighe, Z. Sun, S. Dei, I. T. McGovern, B. Holland, M. Byrne, Y. K. Gunko, J. J. Boland P. Niraj, G. Duesberg, S. Krishnamurthy, R. Goodhue, J. Hutchison, V. Scardaci, A. C. Ferrari and J. N. Coleman. *Nature Nano*, 3:563, 2008.

[81] D. Sen, K. S. Novoselov, P. Reis and M. J. Buehler. *Small*, 6:1108, 2010.

[82] Y.-W. Son, M. L. Cohen and S. G. Louie. *Nature*, 444:347, 2006.

[83] K. A. Ritter and J. W. Lyding. *Nature Mat.*, 8:235, 2009.

[84] C. Ö. Girit, J. C. Meyer, R. Erni, M. D. Rossell, C. Kisielowski, L. Yang, C.-H. Park, M. F. Crommie, M. L. Cohen, S. G. Louie and A. Zettl. *Science*, 323:1705, 2009.

[85] Y. M. You, Z. H. Ni, T. Yu and Z. X. Shen. 93:163112, 2008.

[86] C. Casiraghi, A. Hartschuh, H. Quian, S. Piscanec, C. Georgi, A. Fasoli, K. S. Novoselov, D. M. Basko and A. C. Ferrari. *Nano Lett.*, 9:1433, 2009.

[87] T. M. G. Mohiuddin, A. Lombardo, R. R. Nair, A. Bonetti, G. Savini, R. Jalil, N. Bonini, D. M. Basko, C. Galiotis, N. Marzari, K. S. Novoselov, A. K. Geim and A. C. Ferrari. *Phys. Rev. B*, 79:205433, 2009.

[88] S. Neubeck, Y. M. You, Z. H. Ni, P. Blake, Z. X. Shen, A. K. Geim, and K. S. Novoselov. *Appl. Phys. Lett.*, 97:053110, 2010.

[89] E. Stolyarova, K. T. Rim, S. Ryu, J. Maultzsch, P. Kim, L. E. Brus, T. F. Heinz, M. S. Hybertsen and G. W. Flynn. *PNAS*, 104:9209, 2007.

[90] D. Tomanek, S. G. Louie, H. J. Mamin, D. W. Abraham, R. E. Thomson, E. Ganz, J. Clarke. *Phys. Rev. B*, 35:7790, 1987.

[91] S. Gwo and C. K. Shih. *Phys. Rev. B*, 47:13059, 1993.

[92] C. Thomsen and S. Reich. *Phys. Rev. Lett.*, 85:5214, 2000.

[93] L. G. Cancado, M. A. Pimenta, B. R. A. Neves, M. S. S. Dantas and A. Jorio. *Phys. Rev. Lett.*, 93:247401, 2004.

[94] Q. Yu, J. Lian, S. Siriponglert, H. Li, Y. P. Chen and S.-S. Pei. *Appl. Phys. Lett.*, 93:113103, 2008.

[95] Y. Niimi, T. Matsui, H. Kambara, K. Tagami, M. Tsukuda and H. Fukuyama. *Phys. Rev. B*, 73:085421, 2006.

[96] A. C. Ferrari and J. Robertson. *Phys. Rev. B*, 61:14095, 2000.

[97] A. Das, S. Pisana, B. Chakraborty, S. Piscanec, S. K. Saha, U. V. Waghmare, K. S. Novoselov, H. R. Krishnamurthy, A. K. Geim, A. C. Ferrari, and A. K. Sood. *Nature Nano*, 3:210, 2008.

[98] Digital Instruments. *Veeco Command Reference Manual*, 2003.

[99] C. Lee, Q. Li, W. Kalb, X.-Z. Liu, H. Berger, R. W. Carpick, and James Hone1. *Science*, 328:76, 2010.

[100] J. C. Meyer, A. K. Geim, M. I. Katsnelson, K. S. Novoselov, T. J. Booth, and S. Roth. *Nature*, 446:60, 2007.

[101] J. O. Sofo, A. S. Chaudhari, and G. D. Barber. *Phys. Rev. B*, 75:153401, 2007.

[102] D. W. Boukhvalov, M. I. Katsnelson, and A. I. Lichtenstein. *Phys. Rev. B*, 77:035427, 2008.

Publications

1. A. J. M. Giesbers, U. Zeitler, S. Neubeck, F. Freitag, K. S. Novoselov, J. C. Maan, *Nanolithography and Manipulation of graphene using an atomic force microscope,* Solid State Commun., Vol. **147**, p. 366 (2008)

2. V. G. Kravets, S. Neubeck, A. N. Grigorenko, A. F. Kravets, *Plasmonic blackbody: Strong absorption of light by metal nanoparticles embedded in a dielectric matrix,* Physical Review B, Vol. **81**, p. 165401 (2010)

3. S. Neubeck, L. A. Ponomarenko, F. Freitag, A. J. M. Giesbers, U. Zeitler, S. V. Morozov, P. Blake, A. K. Geim, K. S. Novoselov, *From One Electron to One Hole: Quasiparticle Counting in Graphene Quantum Dots Determined by Electrochemical and Plasma Etching,* Small, Vol. **6**, p. 1469 (2010)

4. S. Neubeck, Y. M. You, Z. H. Ni, P. Blake, Z. X. Shen, A. K. Geim, K. S. Novoselov, *Direct determination of the crystallographic orientation of graphene edges by atomic resolution imaging,* Applied Physics Letters, Vol. **97**, p. 053110 (2010)

5. S. Neubeck, F. Freitag, R. Yang, K. S. Novoselov, *Scanning probe lithography on graphene,* Physica Status Solidi B, Vol. **247**, p. 2904 (2010)

6. S. Neubeck; L. A. Ponomarenko, A. S. Mayorov, S. V. Morozov, R. Yang, K. S. Novoselov, *Scanning gate microscopy on a graphene quantum point contact,* Physica E, accepted (2010)

Nanolithography and manipulation of graphene using an atomic force microscope

A.J.M. Giesbers [a,*], U. Zeitler [a], S. Neubeck [b], F. Freitag [b], K.S. Novoselov [b], J.C. Maan [a]

[a] High Field Magnet Laboratory, Institute for Molecules and Materials, Radboud University Nijmegen, Toernooiveld 7, 6525 ED Nijmegen, The Netherlands
[b] Department of Physics, University of Manchester, M13 9PL, Manchester, UK

ARTICLE INFO

ABSTRACT

We use an atomic force microscope (AFM) to manipulate graphene films on a nanoscopic length scale. By means of local anodic oxidation with an AFM we are able to structure isolating trenches into single-layer and few-layer graphene flakes, opening the possibility of tabletop graphene based device fabrication. Trench sizes of less than 30 nm in width are attainable with this technique. Besides oxidation we also show the influence of mechanical peeling and scratching with an AFM of few layer graphene sheets placed on different substrates.

© 2008 Elsevier Ltd. All rights reserved.

1. Introduction

Carbon is one of the most intensively studied materials in solid state physics. Starting with research activities on graphite six decades ago [1] research on carbon continued to be attractive by the discovery of new carbon allotropes such as Buckminster fullerenes [2], carbon nanotubes [3] and the recent fabrication of isolated single-layers of carbon atoms, graphene [4,5]. Due to the unique electronic properties and high crystal quality of graphene this discovery triggered a great deal of attention in the following years [6]. Besides its fundamental physical properties, the large charge carrier mobilities of up to 200,000 cm^2/Vs [7, 8] (two orders of magnitude larger than silicon MOSFETs) also make graphene a promising candidate for integrated electronic circuitries. Due to its planar geometry it can be integrated rather straightforwardly into the current silicon technology and pave the way for interesting novel nano-electronic devices based on e.g. relativistic p-n junctions [9,10], size-quantized nano ribbons [11–13] or quantum dots [14,15].

Currently, most graphene devices are fabricated using state-of-the-art nanofabrication techniques based on electron beam lithography and subsequent reactive plasma edging. A promising alternative method for the fabrication of proof-of-principle devices may be provided by scanning probe techniques, and, more specifically by AFM-lithography. For traditional semiconductors it was indeed already shown successfully that an atomic force microscope (AFM) can be used to create electronic nanostructures by means of mechanical ploughing [16,17] or local anodic oxidation [21,22] providing a table-top method for the fabrication of e.g. quantum point contacts [17,19], quantum dots [17,20,21] and phase coherent quantum rings [22].

In this work we will demonstrate how an AFM can be used to locate and nano-manipulate single and few-layer graphene sheets. We will show that the way in which a graphene sheet can be manipulated depends strongly on the substrate it is placed on. Second, we will demonstrate how graphene sheets can be shaped by means of electrochemical oxidation, an extremely promising technique for desktop proof-of-principle device fabrication.

2. Experimental techniques, results and discussion

In the past SPM manipulation techniques have already been shown effective to tear, to fold and unfold, and to oxidize graphitic sheets on highly oriented pyrolytic graphite (HOPG) surfaces [23–28]. These experiments already led to speculations towards its use as a tool for nanofabrication of graphitic devices in general and carbon nanotubes, in particular [29]. An interesting question
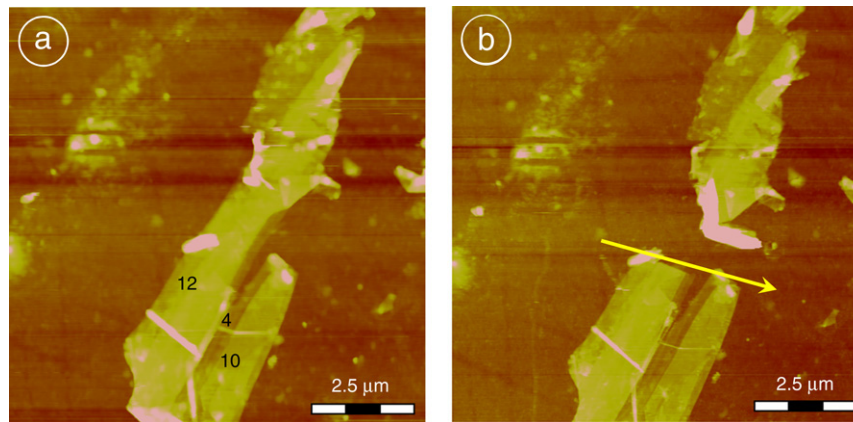

Fig. 1. (Color online) Brute-force mechanical manipulation of few-layer graphene flakes on GaAs ((a) and (b)). The number of layers is depicted in the figure. The flake in (a) is approached from the left with the AFM tip. The flake rips apart and rolls up to the top. Due to the strong van-der-Waals interaction between the graphene and the GaAs substrate, the remainder of the flake remains sticking to the GaAs.
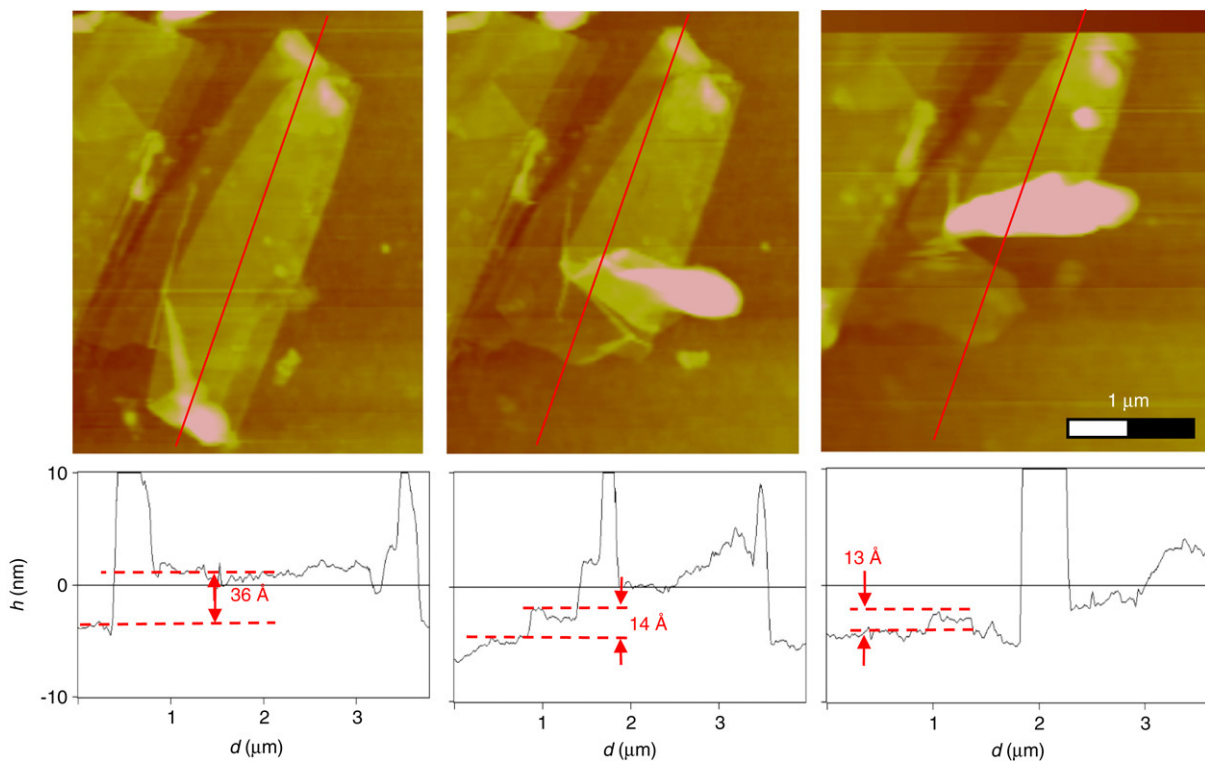

Fig. 2. (Color online) AFM micrographs after three subsequent nano-peeling steps (left to right) of a few layer graphene flake. The pictures on the bottom show the height profiles of each successive step along the lines indicated in the micrographs. The number of layers in the indicated area is reduced from eight to two, leaving an electronically much more interesting graphene bilayer.

to address is whether such an approach can also be applied on few-layer graphene placed on a SiO_2 substrate. For this means we have deposited graphene flakes on a SIMOX wafer using micromechanical exfoliated natural graphite [4,5]. Their position and thickness was subsequently determined under an optical microscope and confirmed by AFM imaging. Trying to scratch through or to peel-off single graphene layers from these few-layer flakes was unsuccessful; due to the relatively low sticking force of the graphene to the rather rough surface of SiO_2 it was only possible to move or crumble entire flakes in a rather uncontrolled fashion.

To make the graphene stick better to the substrate we placed it on a flat, epi-ready GaAs substrate using the same exfoliation technique. Due to the interaction between the graphene flake and

the atomically flat GaAs surface, the graphene is well attached to the substrate and can be structured mechanically. Scanning the tip of an AFM in contact mode with a high contact force across the surface results in a part being torn out of the flake. The tip hooks behind the flake and pulls it into the direction in which the tip is moving (see Fig. 1a and b) because the flake adheres strongly to the surface, it will start to tear along the tip's path. The place where it starts to tear mainly depends on the weakest point near the path of the tip, resulting in rather wide pieces of graphene (up to 1 μm) being torn away. These experiments show that it is indeed possible to displace and even tear apart a graphene flake mechanically; however they also show that controlled nano-machining remains rather difficult. The use of sharp diamond-coated tips [30,31] may improve these, as yet rather crude, scratching techniques considerably.
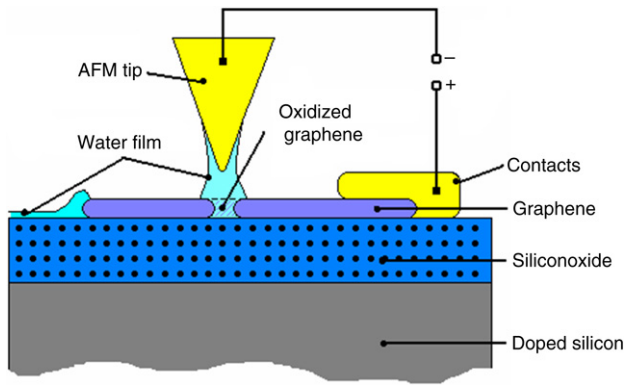
Fig. 3. (Color online) Schematic setup for the local anodic oxidation of graphene. A graphene sheet lies on a SIMOX-substrate and is electrically connected by Au electrodes. A positive bias voltage is applied to the graphene sheet (anode) with the tip of the AFM (cathode) grounded. In a humid environment a water meniscus forms between the AFM and the graphene flake which acts as an electrolyte.

Nevertheless, it is still possible to peel off individual graphene layers from a flake positioned on GaAs (see Fig. 2); the AFM tip hooks behind the upper layers and peels them off the lower layer(s). Although a very delicate process, it opens the possibility of creating single layers on GaAs by AFM rather than going through the tiresome procedure of locating one.

An alternative and indeed most promising technique to manipulate a surface with the AFM is local anodic oxidation [18] (LAO). By applying a bias voltage between the AFM tip and the substrate in a humid environment, the substrate directly beneath the tip is oxidized. Controlling the applied voltage and the position of the tip provides ample control to create any desired surface morphology and structure.

For an application of this technique we used fully contacted single-layer and double layer graphene devices deposited on a 300 nm thick SiO_2 layer on top of heavily doped Si substrate. These contacts might later be used as device contacts when deposited

at suitable positions. We placed the devices under an AFM in an environment with a controlled humidity (55%–60%) which allows the formation of a water meniscus between the AFM-tip and the device surface; a schematic setup is shown in Fig. 3. By applying a positive voltage between the graphene sheet and the tip, the graphene can be locally oxidized below the tip following the concept of electrochemical oxidation. At the cathode the current-induced oxidation of carbon leads to the formation of a variety of carbon-based oxides and acids that will escape from the surface and a groove forms in the graphene sheet directly underneath the AFM tip.

Fig. 4 shows the experimental realization of this principle: The (doped) silicon tip of the AFM is moved in contact mode slowly ($v_{tip} = 0.05 \ \mu m/s$) across a contacted few-layer graphene flake with a constant voltage ($V_{ox} = 25$ V) applied between the tip and the graphene sheet. During this process the environment is kept at a constant humidity of 55% at a temperature of 27 °C. As the graphene flake is oxidized in half, the resistance measured across the flake drastically increases (Fig. 4c). Fig. 4a shows an AFM micrograph of the resulting groove with a width of less than 30 nm, as can be seen in the cross section of Fig. 4b along the indicated line in Fig. 4a. The remaining graphene on both sides of the groove stays intact, making them ideal for graphene in-plane gates [15,32] in more complicated structures. The width of the oxidized grooves typically varies between 30 and 100 nm, mainly depending on the apex of the used AFM-tip, and thereby defines the limit on the resolution possible with this technique.

Although the principle of local anodic oxidation sounds rather straightforward, it is important to remark that this technique only works if the line is started at the edge of a graphene sheet. Oxidizing bulk graphite or starting the oxidation in the middle of a graphene sheet turned out to be practically impossible even with voltages up to 40 V. Most likely the carbon–carbon bonds in the center of a graphene sheet are too strong to be broken directly. In contrast, the edge-termination of graphene [33] by, for example, hydrogen atoms can substantially facilitate the initial oxidation process. Additionally, the hydrophobic character
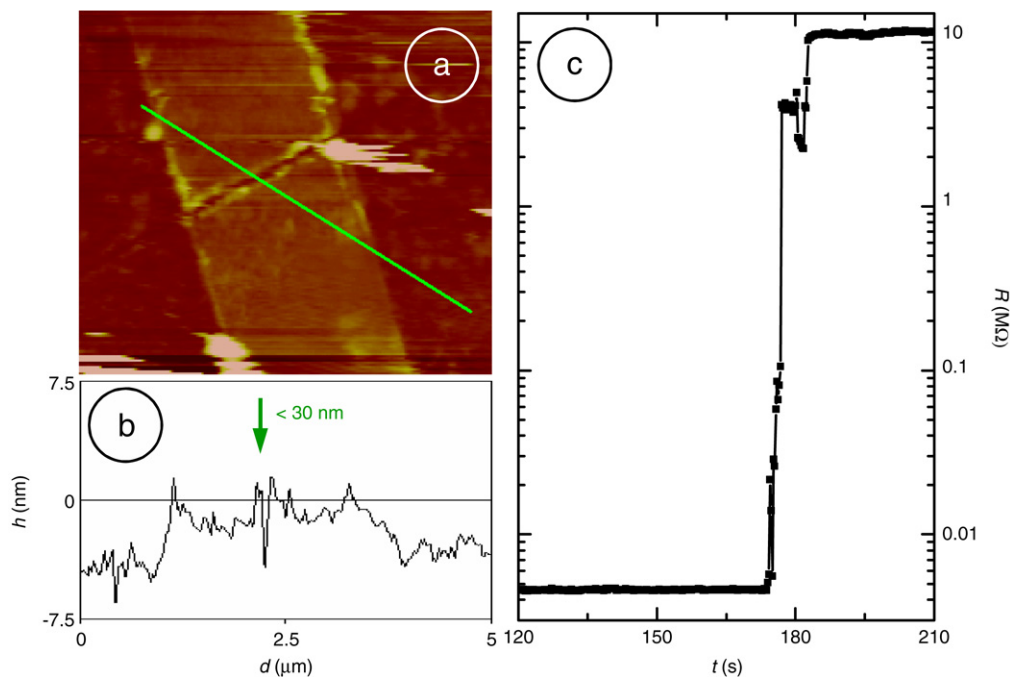
Fig. 4. (Color online) Resistance measurement during the oxidation of a six-layer graphene ribbon. (a) AFM-micrograph taken directly after the oxidation with an unbiased tip. It nicely shows the groove with a line-width of less than 30 nm, where the carbon atoms are removed. (b) Depicts a cross-section of the few-layer graphene ribbon along the line as indicated in (a) showing that the ribbon is clearly oxidized in half. (c) The resistance measured across the ribbon during oxidation increases dramatically as the ribbon is oxidized into two separate parts.
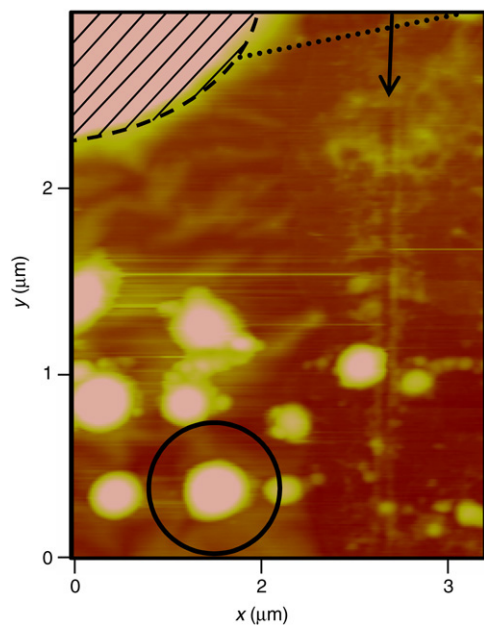
Fig. 5. (Color online) Atomic force micrograph of an oxidized line in a single layer graphene flake. The vertically oxidized line (see arrow) is started at the edge of the flake indicated by the dotted line. Clearly visible are the water droplets (one is encircled) formed on the graphene surface due to the high humidity and hydrophobic character of the graphene. The dashed region is one of the gold contacts to the graphene sheet that serves as cathode during the oxidation procedure.

of graphite will repel water necessary to from a meniscus between tip and substrate during the oxidation procedure. This hydrophobic behavior of a graphene surface is clearly visible in Fig. 5, where the high environmental humidity (58%) leads to the formation of water droplets, (indicated by the circle) on top of a single layer graphene sheet [34]. These droplets only form on the hydrophobic graphene, but not on the more hydrophilic SiO_2 substrate where rather a homogeneous wetting by a water film takes place. As a consequence, we can observe a stripe of water along the edges of the graphene sheet (dotted line in Fig. 5, see also Fig. 4) which will substantially ease oxidation from the edges.

3. Conclusions

In summary, we have shown that it is possible to use an AFM to nano-manipulate individual layers of graphene either by means of mechanical peeling or by electrochemical oxidation. Local anodic oxidation proved to be an extremely useful manner to manipulate graphene. By oxidizing grooves of less than 30 nm wide in a graphene sheet it is in principle possible to cut out every structure imaginable (e.g. quantum point contacts or quantum dots), thus making this technique very promising for table top graphene based device fabrication.

References

[1] P.R. Wallace, Phys. Rev. 71 (1947) 622.
[2] H.W. Kroto, et al., Nature 318 (1985) 162.
[3] S. Iijima, Nature 354 (1991) 56.
[4] K.S. Novoselov, et al., Science 306 (2004) 666.
[5] K.S. Novoselov, et al., Proc. Natl. Acad. Sci. USA 102 (2005) 10451.
[6] A.K. Geim, K.S. Novoselov, Nature Mater. 6 (2006) 183.
[7] S.V. Morozov, et al., Phys. Rev. Lett. 100 (2008) 016602.
[8] K.I. Bolotin, et al., Solid State Commun. 146 (2008) 351.
[9] J.R. Williams, L. DiCarlo, C.M. Marcus, Science 317 (2007) 638.
[10] B. Huard, et al., Phys. Rev. Lett. 98 (2007) 236803.
[11] A. Rycerz, J. Tworzydlo, C.W.J. Beenakker, Nature Phys. 3 (2007) 172.
[12] M.I. Katsnelson, K.S. Novoselov, A.K. Geim, Nature Phys. 2 (2006) 620.
[13] M.Y. Han, B. Özyilmaz, Y. Zhang, P. Kim, Phys. Rev. Lett. 98 (2007) 206805.
[14] B. Trauzettel, D.V. Bulgev, D. Loss, G. Burkard, Nature Phys. 3 (2007) 192.
[15] C. Stampfer, et al., Appl. Phys. Lett. 92 (2008) 012102.
[16] M. Wendel, Appl. Phys. Lett. 65 (1994) 1775.
[17] H.W. Schumacher, et al., Appl. Phys. Lett. 75 (1999) 1107.
[18] M. Ishii, K. Matsumoto, Japan J. Appl. Phys. Part 1 34 (2B) (1995) 1329.
[19] R. Held, et al., Appl. Phys. Lett. 71 (1997) 2689.
[20] S. Lüscher, et al., Appl. Phys. Lett. 75 (1999) 2452.
[21] U.F. Keyser, et al., Appl. Phys. Lett. 76 (1999) 457.
[22] A. Fuhrer, et al., Nature 413 (2001) 822.
[23] H.-V. Roy, C. Kallinger, B. Marsen, K Sattler, J. Appl. Phys. 83 (1998) 4695.
[24] H.-V. Roy, C. Kallinger, K. Sattler, Surf. Sci. 407 (1998) 1.
[25] L.X. Li, et al., Carbon 44 (2006) 1544.
[26] H. Hiura, T.W. Ebbesen, J. Fujita, K. Tanigaki, T. Takada, Nature 367 (1994) 148.
[27] X. Lu, et al., Nanotechnology 10 (1999) 269.
[28] H. Hiura, Appl. Surf. Sci. 222 (2004) 374.
[29] T.W. Ebbesen, H. Hiura, Adv. Mater. 7 (6) (1995) 582.
[30] J. Regul, et al., Appl. Phys. Lett. 81 (2002) 2023.
[31] P. Barthold, T. Lüdtke, R.J. Haug, arXiv:0803.2470(2007).
[32] F. Molitor, et al., Phys. Rev. B 76 (2007) 245426.
[33] Y. Kobayashi, K. Fukui, T. Enoki, K. Kusakabe, Phys. Rev. B 73 (2006) 125415.
[34] M. Luna, J. Colchero, A.M. Baro, J. Phys. Chem. B 103 (1999) 9576.

☙

Plasmonic blackbody: Strong absorption of light by metal nanoparticles embedded in a dielectric matrix

V. G. Kravets, S. Neubeck, and A. N. Grigorenko

School of Physics and Astronomy, University of Manchester, Manchester M13 9PL, United Kingdom

A. F. Kravets

Institute of Magnetism, National Academy of Sciences of Ukraine, 36-b Vernadsky Boulevard, Kiev 03142, Ukraine

We have experimentally and theoretically demonstrated strong absorption of visible light in a thin nanostructured layer consisting of silver nanoparticles embedded in a dielectric matrix. Light absorption at the level of above 90% is recorded over a wide optical wavelength range (240–850 nm) and for a broad range of angles of light incidence (0°–70°) in extremely thin films (160 nm). We suggest a generic principle for enhancement of light absorption in thin layers of artificial metamaterials and show that effective refractive indices of our samples measured with the help of ellipsometry can be adequately described by an effective-medium theory. We demonstrate that a substantial fraction of light can be trapped in the nanostructured film due to scattering by noble metal nanoparticles and total internal reflection.

I. INTRODUCTION

An ideal blackbody is an object that absorbs all light that falls on it. Being a perfect absorber, a blackbody could be valuable for many important applications, e.g., photodetection or collection of solar energy (photovoltaic cells). Of particular interest are thin black body films which could efficiently trap photons and transfer their energy into electric or thermal energy. Such thin films are extremely difficult to find because there do not exist many natural materials that could absorb light over a wide optical wavelength range and for a broad range of angles of incidence and be integrated with silicon technology. A possible route to produce thin film absorbing coatings is to use plasmonic photonic crystal structures,[1,2] periodic metallic structures,[3–7] in which desired absorption is achieved via collective electronic excitations called plasmons, both propagating and localized. However, the resonant nature of these effects implies that absorption can only be large over a relatively narrow range of wavelengths. For example, Popov *et al.*[8] presented two-dimensional crossed gratings for total absorption of unpolarized light where high absorption was limited to small ranges of angles of incidence due to the sharply resonant nature of plasmon-polariton wave excitation. A strong absorption in a wide angular interval but in a small spectral interval has been demonstrated in shallow lamellar metallic gratings.[9]

In our recent work[10] we suggested a generic design for blackbodylike thin coatings and demonstrated its validity by producing nanostructured gold films about 100 nm thick that absorb visible light in a wide spectral range over a large range of incident angles. By analyzing Fresnel coefficients we showed that for any fixed thickness of a film, h, there exists a range of complex indices of refraction, n, of the layer placed on top of a substrate which would guarantee maximal light absorption.[10] The values of the refractive indices that would yield the strongest absorption for the nanofilms are not readily available in natural materials. We have shown, however, that suitably nanostructured metal-dielectric composites could possess the desired effective refractive indices. To describe optical behavior of our structures we used the Maxwell-Garnett effective approach[11,12] and showed that the gold stripes can be considered as a homogeneous layer with an effective refractive index that would guarantee very strong absorption of visible light in the system. Our experimental structures[10] were made by electron beam lithography which is expensive. A development of thin inexpensive absorbing coatings would greatly increase their area of applications. Feasible low-cost techniques could be based on silicon nanostructures which can be grown from the gas phases (physical-vapor deposition methods) or chemical catalyzing methods. The absorbing layer for solar cells should ideally be thin (∼100 nm) with the absorption above 90% in the range of wavelengths 400–900 nm where the sun spectral intensities achieve maximal values.

The main aim of this paper is to demonstrate blackbodylike coatings working in wide spectral region [visible-near infrared (IR)] and broad angles interval (up to 70°) produced by an inexpensive evaporation technique. In this paper we present results for nanostructured films made of a mixture of Ag particles in Al_2O_3 matrix. Silver has a very small imaginary part of the dielectric constant and very high electrical conductivity, which leads to the excellent optical and electronic properties of silver nanostructures. These excellent properties have motivated us to study silver nanoparticles embedded in a dielectric matrix with the aim to achieve strong light absorption in a broad spectral region. In addition to it, Ag, due to its lower absorption and lower cost is thus better choice than Au, although it should be well encapsulated to avoid oxidation effects that are not present for Au. We chose Al_2O_3 as a dielectric layer because of its very stable chemical behavior and high refractive index ∼1.7. We demonstrate that extremely high absorption (∼95%) could be achieved with 100–120 nm Ag particles randomly distributed in Al_2O_3 with volume concentration about 15%. It should be stressed that manufacturing of such type of high absorber devices does not require expensive lithographic

(optical or electron beam) techniques and can be optimized for production of large sizes of low-cost solar cells. These structures permit a high level of absorption (more than 90%) of unpolarized light in a wide range of incident angles $(-45°, +45°)$. Absorption higher than 95% for *p*-polarized light is revealed over a range of angles of incidence $(-70°, +70°)$.

The paper is organized as follows. Section I provides the description of experimental methods and procedures. We discuss the results obtained on the fabricated samples in Sec. II. In Sec. III we discuss the theory of a plasmonic blackbody based on artificial films produced by inclusion of metallic nanoparticles into a dielectric host. We provide the analytical formula for the silver dielectric constants derived from the spectroscopic ellipsometry measurements and present the results of the calculations based on the Maxwell-Garnett theory. We compare the experimental results with theory in Sec. IV. Finally, the conclusion is given.

II. EXPERIMENTAL PROCEDURES

The $Ag_x(Al_2O_3)_{1-x}$ nanostructured films (where x $=0.07-0.9$ is the atomic fraction of Ag) of large areas $(2.5 \times 2.5$ cm^2) of thickness $\sim 150-160$ nm were deposited using e-beam evaporation from Ag and Al_2O_3 independent sources onto glass substrates. The pressure was less than 10^{-4} Pa during the film deposition. The composition of the films was determined using energy-dispersive x-ray analysis. The crystalline structure was investigated by x-ray diffraction and scanning electron microscopy (SEM). The fabrication conditions were adjusted to achieve an average particle diameter $D \sim 100-120$ nm with an average interparticle separation distance larger than the particle diameters $(0.08 < f < 0.3$, f is the volume fraction of Ag particles). The thickness of deposited films has been chosen slightly higher than the average diameter of the silver spheres.

The ellipsometric measurements were performed with a Woollam VASE variable angle ellipsometer of rotating-analyzer type in the wavelengths range of 240–1000 nm. The complex dielectric function $\varepsilon(\lambda)=\varepsilon_1(\lambda)+i\varepsilon_2(\lambda)$ was directly determined from ellipsometric parameters $\psi(\lambda)$ and $\Delta(\lambda)$.[13] The inversion of ellipsometric data was performed within the framework of film-substrate model (pure substrate was also measured). We take into account possible perturbations of the ellipsometric data due to surface roughness or grain texturing. Our measurements at multiple angles of incidence from 45° to 80° confirm that the surface roughness effect on $\varepsilon(\lambda)$ is less than 2–5 % over the measured spectral range and therefore does not significantly influence relative changes in $\varepsilon(\lambda)$. From atomic force microscopy images the rms value of the surface roughness was found to be less than ~ 10 nm.

We have also measured reflection and transmission for *p*- and *s*-polarized light for angles of incidence of light $0°-80°$ using Ocean Optics USB2000 spectrometer. The spectrometer is equipped with a xenon light source. The light passed through a polarizer and then was focused by objective on the surface of the sample to a spot of approximately 200 μm. The sample was mounted on a rotation stage. The transmitted
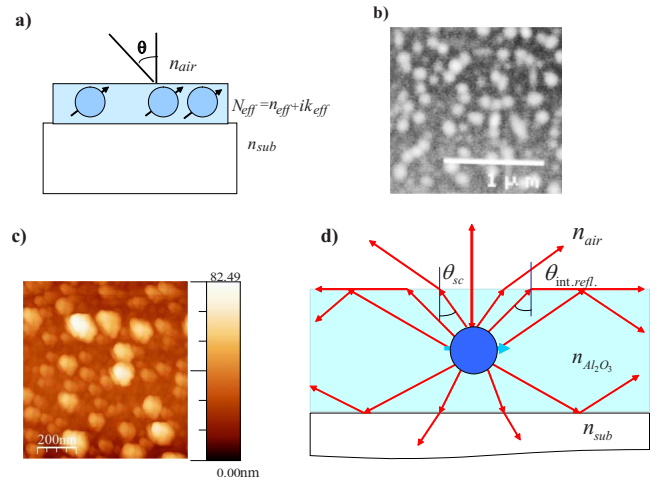

FIG. 1. (Color online) Schematics of perfect absorber blackbody. (a) Schematic view of the nanostructured layer on a substrate. (b) A SEM image of one of the studied silver nanostructures. (c) AFM image of silver nanostructures with volume filling factor of Ag, $f=0.15$. (d) Schematic illustration of the light trapping in nanostructured film due to dipole scattering on a nanoparticle.

light was collected using an optical fiber coupled to the spectrometer (200 μm core). The transmission spectra were found by normalizing spectra measured through the sample with respect to the spectra measured through the air.

III. EXPERIMENTAL RESULTS

Metal films are usually highly reflective in the visible and infrared regions even at small thicknesses. Indeed, light waves are evanescent inside metals and penetrated at small distance in metallic films (the skin depth). Using the measured refractive index for pure Ag film[14] we can estimate skin depth as $\lambda/(4\pi k)$, which is about 13 nm in the visible and near IR region. If the thickness of an Ag film is much larger than the skin depth, transmission can be neglected and most of light is reflected. The reflectivity of bulk silver is almost independent of wavelength and close to 100% over the entire visible region.[14] Consequently, the absorption of plain Ag layers is usually small. For example, 100-nm-thick plain Ag film absorbs only about 3–4 % in the visible region and about 2–3 % in the near IR region. It comes, therefore, as a nice surprise that a composite material made from Ag nanoparticles embedded into a dielectric layer can demonstrate extremely high level of absorption as described in the experiments and theory below.

Silver nanoparticles of varying volume filling fractions, f, were deposited into Al_2O_3 amorphous matrix. SEM image, Fig. 1(b), shows a typical morphology of these films. Particle sizes and the filling fraction were controlled by the deposition ratio of Ag and Al_2O_3. Film thickness was determined from ellipsometry and profilometry and ranged from 150 to 160 nm. The structural characterization was also done by atomic force microscopy (AFM). AFM analysis is performed in the tapping mode on the sample to examine the surface morphology in a scan area of 1.0×1.0 μm^2. AFM image of the Ag-Al_2O_3 nanostructure is shown in Fig. 1(c). AFM im-
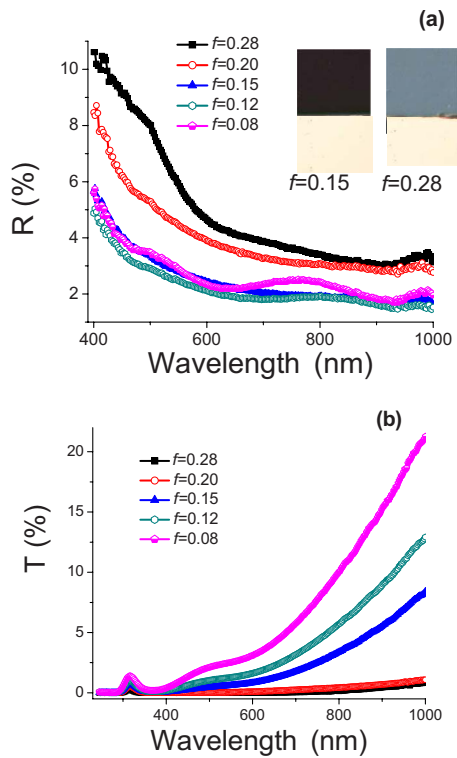
FIG. 2. (Color online) Optical properties of the Ag-Al$_2$O$_3$ nanostructures for different filling factor of Ag, $0.08 \leq f \leq 0.28$. (a) The reflection spectra for the light of p polarization at normal incidence and (b) the transmission spectra for p-polarized light at normal incidence. Insets show the polarization-contrast optical microscopy images for reflected light for two samples: $f=0.15$ and $f=0.28$.

age demonstrates the presence of a large number of Ag nanoparticles in films. The average particle diameter was between 80 and 120 nm (about 100 nm in the composite with $f \approx 15\%$).

We measured reflection and transmission coefficients for Ag-Al$_2$O$_3$ nanostructures with different volume concentration of Ag. Figure 2 shows the corresponding reflectance and transmittance spectra of nanocrystalline Ag-Al$_2$O$_3$ films at normal incidence. The reflected intensity (Fig. 2) is expectedly high ($\sim 5-10\%$) at $\lambda \sim 400$ nm; it then falls monotonously below $\lambda \sim 450$ nm and reaches approximately constant values $\sim 2-3\%$ for wide spectral range 500–1000 nm. Note that with a decrease in the volume concentration of Ag nanoparticles the reflectance decreases at all wavelengths. As we can see from Fig. 2, the fabricated nanocomposite layer behaves like bulk silver for large volume concentration of Ag ($f \sim 0.3$) resulting in no transmission. The transmission peaks at around 320 nm are connected to plasmon resonances of silver nanoparticles. The transmission of less than 3% is observed for wide spectral region 250–800 nm for concentration of Ag nanoparticles of about 15 vol %. It is worth noting that with increasing of volume concentration of Ag the particle size slightly increases.

Our measurements reveal that the smallest value of $R(\lambda)$ and $T(\lambda)$ is very sensitive to the volume concentration of Ag nanoparticles. Thus we conclude that the changes in concentration of Ag particles embedded in Al$_2$O$_3$ matrix (and their

sizes) strongly affect the enhancement of absorption. We found that the optimal geometrical parameters for the design of blackbodylike nanostructures are as follows: volume filling factor $f \approx 0.15$, diameter of silver particular $D \approx 100-120$ nm, and thickness of layer $h \approx 160$ nm. More importantly, it was found that the reflection and transmission can show low values in a large wavelength range ($\leq 2\%$ for some angles of incidence). Note that the absorption can be approximately enhanced by 2 orders of magnitude over bulk Ag.

To further investigate enhancement of absorption for the studied metamaterials, we recorded the reflection and transmission at different angles of light incidence. Measurements of optical transmittance, $T(\lambda)$, and reflectance, $R(\lambda)$, were made over the spectral range 250–1000 nm at angles of incidence, θ, from $0°$ to $70°$ for both incident p- and s-polarized radiations. The results are shown in Figs. 3(a) and 3(b) and the most important features of these curves are as follows. For incident angles up to $65°$ the reflectivity is close to 2% for p-polarized light at the wavelength range of 240–1000 nm. For these angles of incidence we observed pronounced reflectivity plateau with values of $R_p(\lambda)$ as low as 2% in the spectral range 400–1000 nm. More detailed analysis shows that for p-polarized light angular dependence of spectra $R_p(\lambda)$ exhibits maximum in the range $\lambda \sim 350-370$ nm for $\theta \geq 60°$ and then decrease with increasing the incident wavelength. This peak becomes increasingly prominent with increasing incident angle.

Figure 3(b) shows the transmission spectra of the studied nanostructures for p-polarized light, for the incident angles $\theta = 0°-70°$. They show an increase in the intensity of transmitted light with increasing wavelength. The spectra for different angles of incidence, θ, are similar. The optical transmission for p-polarized light leads to a low value less than 3% for a wavelength range of 240–850 nm. For angles of incidence $\theta \geq 60°$ the level of intensity for the transmitted light in the whole spectral range of 240–1000 nm is close to $1-2\%$. We see that the changes in the intensity of transmitted light for investigated spectral region are negligible. Note that the value of transmitted intensity for low wavelengths is close to zero, except near $\lambda \sim 320$ nm where it is about 1%. In Fig. 3(c) we see that the absorption rises to the relatively large value more than 95% for wide spectral region 400–850 nm and angles of incidence from $0°$ to $70°$. This result confirms that the absorption of light is very high and is rather insensitive to angles of incidence due to spherical symmetry of the silver nanoparticles. This enhanced absorption occurs for p-polarized light in a range of angle of incidence equal $(-70° : 70°)$.

In contrast to the p-polarization results, the s-polarization reflectivity shows an increase in intensity from 7% to 47% [Fig. 4(a)] with increasing incident angle. At low angles, $\theta \leq 45°$, the reflectivity spectra for both polarizations are similar. This is due to the fact that the absorption for both polarizations at low incidence angles is generated by the electric-field component parallel to the film plane. At high incidence angles, the perpendicular to plane of incidence electrical-field component becomes much larger than the parallel one which affects reflection of p-polarization. Figure 4(b) shows the optical transmission spectra for the light of s-polarization
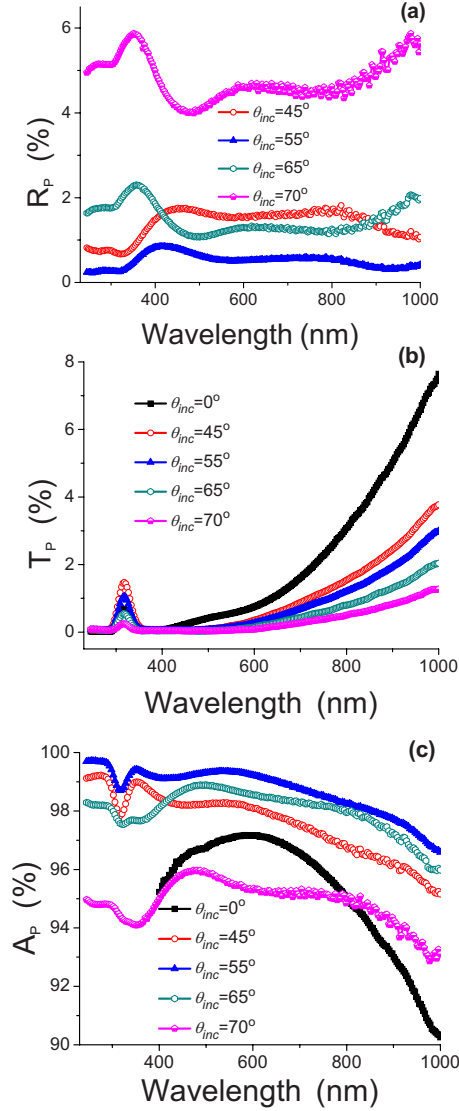
FIG. 3. (Color online) Optical properties of the Ag-Al$_2$O$_3$ nanostructures with $f=0.15$ and $D\approx120$ nm. (a) The reflection spectra for the light of p polarization and $45°\leq\theta\leq70°$. (b) The transmission spectra for the light of p polarization and $0°\leq\theta\leq70°$. (c) The absorption spectra for the light of p polarization.

FIG. 4. (Color online) Optical properties of the Ag-Al$_2$O$_3$ nanostructures with $f=0.15$ and $D\approx120$ nm. (a) The reflection spectra for the light of s polarization and $45°\leq\theta\leq70°$. (b) The transmission spectra for the light of s polarization and $0°\leq\theta\leq70°$.

and $0°\leq\theta\leq70°$. We can see that the transmission spectra for both p- and s-polarizations [Figs. 3(b) and 4(b)] are similar only values of T_S are slightly higher than T_P for long wavelengths. Combining data shown in Figs. 3 and 4 we conclude that such metal nanostructures can strongly absorb light (more than 90%) of both p- and s-polarizations (or unpolarized light) in a wide range of incidence ($0°\leq\theta\leq45°$).

As the average particle size of the embedded nanocrystalline silver into Al$_2$O$_3$ matrix is changed, we observe by eyes a marked change in its color, from white (in the bulk) to black for particles with sizes of 100–120 nm. Inset of Fig. 2(a) shows the polarization-contrast optical microscopy images for reflected light for two samples: $f=0.15$ and $f=0.28$. We see that the reflection from our sample ($f=0.15$) is very small for the p-polarized light. This picture confirms the blackness of our nanostructured film.
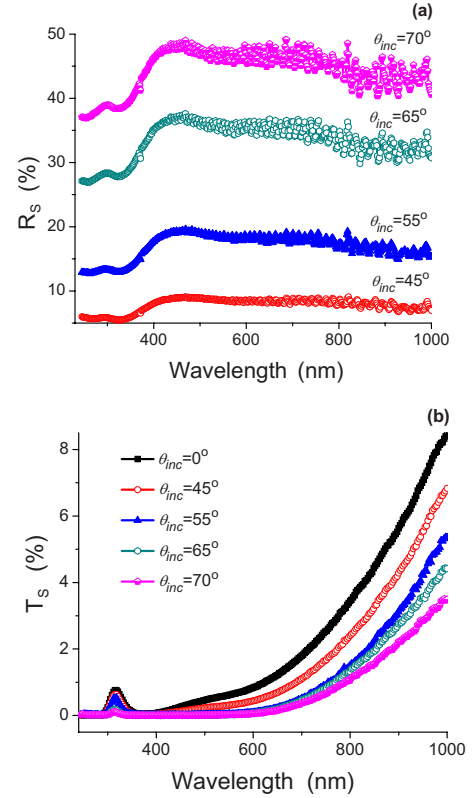
IV. THEORY

Let us consider a monolayer of metal nanoparticles embedded in oxide matrix and deposited onto a dielectric substrate as shown in Fig. 1(a). It is supposed that the spatial distribution of nanoparticles in the oxide matrix is random and the distances between particles are comparable with the wavelength of light. We are looking for a structure that could strongly increase light absorption (and hence improve efficiency of a solar cell or a photodetector). There are two basic ways how an enhancement of photocurrents due to the presence of covering layers can be achieved: (i) concentration of a scattered (diffracted) light into an absorbing (e.g., photoactive) region or (ii) near-field light concentration into an absorbing region. According to the Mie theory for a single spherical particle,[15] the relative strengths of light absorption and scattering can be determined from the absorption and scattering cross sections σ_{abs} and σ_{sca} of the individual particles,[15]

$$\sigma_{abs}=\frac{2\pi}{\lambda}\mathrm{Im}(\alpha),\tag{1a}$$

$$\sigma_{sca}=\frac{1}{6\pi}\left(\frac{2\pi}{\lambda}\right)^4|\alpha|^2.\tag{1b}$$

Here, α is the polarizability of the particle and λ is the wavelength. We define the scattering efficiency Q_{rad} of the par-
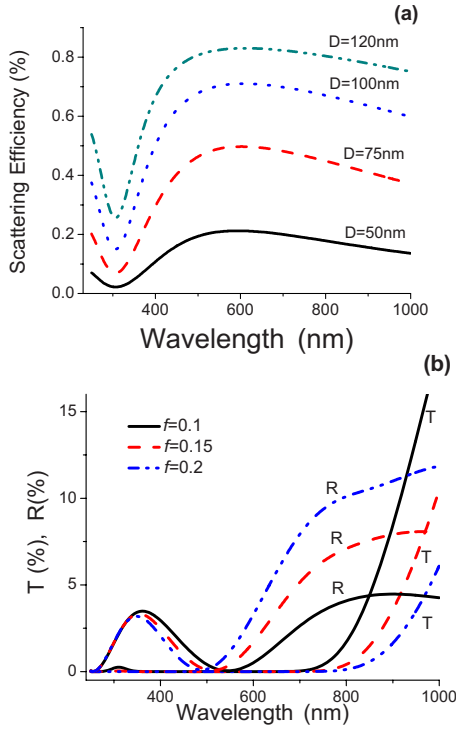
FIG. 5. (Color online) (a) Scattering efficiency for the Ag-Al$_2$O$_3$ nanostructures as a function of particle diameter, D; (b) the numerical results for transmission and reflection spectra at normal incidence for the Ag-Al$_2$O$_3$ nanostructures with different volume fraction of Ag: $f = 0.1, 0.15, 0.2$.

ticles as $Q_{rad} = \sigma_{sca}/(\sigma_{sca} + \sigma_{abs})$. Note that Q_{rad} represents the fraction of the extinction energy that is reradiated.

Figure 5(a) shows a plot of Q_{rad} as a function of the particle diameter, D. The scattering efficiency Q_{rad} increases as the particle size is increased. This occurs because larger particles have higher polarizabilities, resulting in larger radiative losses. The sharp drop in Q_{rad} at short wavelengths is due to interband transitions in silver particles. Note that the size of particles cannot be increased indefinitely because the particles should be much smaller than the wavelength of light. Figure 5(a) demonstrates that scattering efficiency more than 80% can be achieved for Ag nanoparticles embedded into Al$_2$O$_3$ with diameters about 120 nm. For dense particle arrays, the light scattered by nanoparticles is responsible for reflected or refracted rays due to light interference. However, in our case of a sparse array of nanoparticles embedded into a dielectric matrix (with particle separation comparable with the light wavelength) the light scattered by nanoparticles could be effectively trapped in the dielectric layer due to the total internal reflection, see Fig. 1(d), and be eventually absorbed. It is easy to evaluate the trapping angle of light as $\arcsin(1/n) = 35°$ for the normal light incidence at the air-film interface. This implies that only radiation going into the top 1.2 sr [which is about $1.2/(4\pi) \approx 9\%$ of the total solid angle] will partially escape the film into the air. There exists an optimum combination of the particle diameter, D, and their filling fraction, f, in dielectric matrix (with high real refractive index, n) that maximizes the light trapping and optical absorption based on such structures.

We can therefore associate attenuation of a light coming through our samples with scattering and absorption. The extinction cross section is therefore the sum of the scattering and absorption cross sections: $\sigma_{ext} = \sigma_{sca} + \sigma_{abs}$. Applying Lambert-Beer's law the resulting intensity transmitted through a monolayer of the noninteracting metal particles is: $T \propto \exp(-N\sigma_{ext}h_{eff})$ (where the particle number density, $N = \frac{3f}{4\pi a^3}$, is related to the filling factor f and the particle radius a; h_{eff} is the effective thickness of particle layer and its magnitude is larger than geometrical thickness of layer, h). In our simulation we set $h_{eff} \approx 10\lambda$ (λ is the wavelength). This value is consistent with the average path length of a trapped beam for Lambertian surfaces estimated by Yablonovitch (Ref. 16). Figure 5(b) shows the calculated transmission spectra versus wavelength for silver particles in Al$_2$O$_3$ matrix for low filling factor, f, ranging from 0.1 to 0.2. It can be seen that the decrease in the filling factor f gives rise to the transmission T for the large wavelengths. Note that the intensity of transmission spectra drops below 5% in the spectral region $\lambda = 800–900$ nm, which is important due to light trapping at wavelength near the band gap of Si, commonly used in solar cells.

It is necessary to stress that a studied metamaterial is in the borderline between the effective medium and a random array of individual scatters. This leads to interesting and rich physics that includes light localization, random hot spots of absorptions, etc. At the same time, it makes extremely difficult for one to model all properties of the material with just one model. As an alternative to the theoretical model described above, we consider an effective medium approach to fabricated samples modified by the presence of trapped light modes. In our previous work (Ref. 10), using Fresnel coefficients for transmission and reflection coefficients we have shown that a thin film (of thickness ~ 100 nm) with the effective refractive index $n_{eff} \approx 1.2–1.7$ and $k_{eff} \approx 0.3–0.6$ in the visible and near IR region guarantees the maximal absorption of incident light. We show here that the studied arrays of Ag particles in the dielectric matrix also possess analogous optical constants.

To calculate the effective refractive index of the studied nanocomposites we use the Maxwell-Garnet effective-medium approximation (EMA).[11,12] EMA describes the interaction between the incident light and nanostructured materials and assigns a complex effective index of refraction to such structures. This approach worked surprisingly well being applied to plasmonic blackbody nanostructures based on gold nanostripes.[10] Here, the size of Ag particles is not small as compared to the wavelength of ultraviolet and visible light, and it becomes important to take into account the effects of multiple scattering in the optical response of the film structures. In this range of particle sizes the scattering effects are described with the help of the Mie theory of scattering.[15] In the dipole approximation of Mie's theory each nanoparticle can be represented by an electric dipole, $\boldsymbol{p}$, with the dipole polarizability α. For particles sizes $D \approx 100$ nm with non-negligible absorption loss in the approximation introduced by Doyle,[17] a dynamic polarizability can be written as,[15,17]

$$\alpha = i\frac{3a^3}{2x^3}a_1, \tag{2}$$

where $x = 2\pi n_d a/\lambda$ is the size parameter ($n_d = \sqrt{\varepsilon_d}$ is the refractive index of Al_2O_3, $a = D/2$ is the radius of the particle). The Mie coefficient a_1 is given by[15,17,18]

$$a_1 = \frac{m\psi_1(mx)\psi_1'(x) - \psi_1(x)\psi_1'(mx)}{m\psi_1(mx)\xi_1'(x) - \xi_1(x)\psi_1'(mx)}, \tag{3}$$

where $\psi_1(x)$ and $\xi_1(x)$ are the Riccati-Bessel functions, $m = \sqrt{\varepsilon/\varepsilon_d}$ is the ratio of the index refraction of the silver spheres, ε, to that of the host dielectric (Al_2O_3).

This dipole approximation was shown to be adequate when distances between particles are on the order of or larger than their diameter D, i.e., for small volume fractions f ($f < 0.5$). To calculate effective optical constants of a mixture, we follow the Maxwell-Garnet approach[11,12] and assume that the effective dielectric function of nanocomposite material is related to the dipole polarizability of nanoparticles by the Clausius-Mossoti equation,

$$\frac{\varepsilon_{eff} - \varepsilon_d}{\varepsilon_{eff} + 2\varepsilon_d} = \frac{f}{a^3}\alpha. \tag{4}$$

This yields the following extended Maxwell-Garnett formula,[19]

$$\varepsilon_{eff} = \frac{a^3 + 2f\alpha}{a^3 - f\alpha}\varepsilon_d. \tag{5}$$

To take into account the dispersion of the particle sizes (naturally arising during the deposition process), we introduce a size distribution function as a log-normal distribution,[17]

$$f_{LN}(D) = \frac{1}{(2\pi)^{1/2}\ln\sigma}\exp\left[-\frac{(\ln D/D_{av})^2}{2\ln^2\sigma}\right], \tag{6}$$

where D_{av} is the average diameter of the nanoparticles and σ is the standard deviation ($\sigma = 1.5$, in our calculation). Then, the complex effective dielectric function, ε_{eff}, can be written as

$$\varepsilon_{eff} = \int_0^\infty \varepsilon_{eff}(D)f_{LN}(D)dD. \tag{7}$$

It is easy to see that the effective dielectric function, ε_{eff}, strongly depends on dielectric function of silver nanoparticles [see Eqs. (2)–(5)]. Permittivity of silver is the sum of the interband and intraband components and often depends on the way how silver was fabricated. In our calculations we assume that the permittivity of Ag nanoparticles of size ~ 100 nm is the same as that of a silver film of thickness ~ 100 nm. To find the optical constants, we have evaporated a thin silver film under the same conditions that were used in technology processes for preparing of Ag-Al_2O_3 mixtures. We have extracted the spectral dependences of the complex refractive index $n + ik = \sqrt{\varepsilon(\omega)}$ for the fabricated silver films using spectroscopic ellipsometry (performed with a Woollam spectroscopic ellipsometer). The extracted dielectric function, ε, was then modeled by fitting with two Lorentz functions and the Drude term,[10]
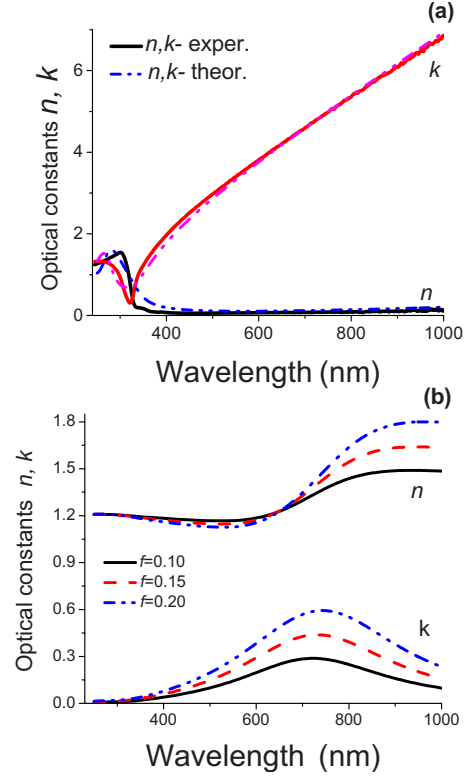

FIG. 6. (Color online) (a) The complex refractive index for a dense 100 nm silver film as a function of wavelength extracted with ellipsometry, solid line, Drude-Lorentz fit, dash-dotted line; (b) the real and imaginary parts of the effective refractive index for the Ag-Al_2O_3 nanostructures with different volume fraction of Ag: $f = 0.1, 0.15, 0.2$.

$$\varepsilon(\omega) = \varepsilon_0 - \frac{\omega_p^2}{\omega^2 + i\omega\gamma} - \sum_{j=1}^3 \frac{\Delta\varepsilon_j\Omega_j^2}{\omega^2 - \Omega_j^2 + i\omega\Gamma_j}. \tag{8}$$

A very good agreement between the extracted experimental dependence of $n_{exp} = n + ik$ and the analytical formula (8) was obtained for the following parameters: $\varepsilon_0 = 4.5$; $\Delta\varepsilon_j = (1.0, 1.1)$; $\hbar\omega_p = 9.0$ eV $\hbar\gamma = 0.07$ eV; $\hbar\Omega_j = (4.5, 5.7)$ eV; $\hbar\Gamma_j = (1.2, 2.7)$ eV, where $j = 1, 2$. Figure 6(a) shows the real and imaginary part of the refractive index of Ag particles used in our calculation as a function of wavelength. The optical constants of an Al_2O_3 film have been parameterized by the Cauchy function. To find Cauchy coefficients we again carried out spectroscopic ellipsometry measurements of pure Al_2O_3 film. The refractive index of Al_2O_3 films shows low dispersion with values of $n_d = 1.725 - 0.02$ throughout the visible and near IR spectral range.

Using Eqs. (2)–(8), we simultaneously calculated the effective refractive index (see Fig. 6), optical transmission and reflection spectra [Fig. 5(b)]. The reflectance spectra at normal incidence were calculated with the help of the Fresnel equations for a two layer system: a uniform layer of silver nanospheres in Al_2O_3 matrix (effective medium) and a thick glass substrate (1 mm). The thickness of the effective layer has been chosen to be higher than diameter of silver nanoparticles ($h \sim 160$ nm). The main goal of the calculations

was to find conditions at which the reflectance R and transmittance T are minimal. Figure 5(b) shows the calculated reflection and transmission spectra of the Ag-Al$_2$O$_3$ nanostructures for small filling factor, f, ranging from 0.1 to 0.2 and average diameter of particles about $D \approx 120$ nm. The reflectance at normal incidence was calculated using the effective index of refraction and including log-normal particle-size distributions. Using the Kirchhoff's rule (the sum of the transmittance $T(\lambda)$, reflectance $R(\lambda)$, and absorbance $A(\lambda)$ should equal 1 in the absence of diffuse scattering), we concluded that the coefficient of absorption for the studied nanostructure can be higher 95% in the wavelength range of 240–800 nm, see Fig. 5(b). Thus the light absorption was optimized for normal light incidence with respect to three parameters, f, D, and h. Numerical optimizations for $h = 150–160$ nm suggested that the lowest reflected and transmitted intensities (of about 2–5 %) are achieved for the values of the $f = 0.1–0.2$, $D = 100–120$ nm. The calculated dependences demonstrate that the studied composites can be optimized to yield absorption of light at the level above 95% for unpolarized light in spectral region 240–850 nm.

The calculated complex refractive index of Ag-Al$_2$O$_3$ composite films using the EMA approach is shown in Fig. 6(b). We compared the values of $n_{eff} + ik_{eff}$ for the Ag-Al$_2$O$_3$ nanostructures of different volume fraction f. Figure 6(b) shows that $n_{eff} + ik_{eff}$ depends more strongly on f at the wavelength region 600–1000 nm. We also see that the real part of the refractive index n_{eff} increases with the increase in wavelength. The values of n_{eff} ranged from 1.2 to 1.7; they are much higher than that of bulk Ag [e.g., $n = 0.04$, $\lambda = 825$ nm (Ref. 14)]. The imaginary part of refractive index, k_{eff}, increases with increasing volume concentration of Ag particles, f. One pronounced extinction peak appeared in all k_{eff} curves, see Fig. 6(b). This peak can be associated with excitation of localized surface plasmons in silver particles. This absorption peak is redshifted when the volume concentration of silver particles is increased. The values of k_{eff} are small, except for those in the surface plasmon resonance extinction region, indicating that these nanostructures selectively absorbed and scattered incident light at specific wavelength bands. The silver nanoparticles embedded in Al$_2$O$_3$ matrix exhibit a spectrally broad dipolar resonance due to distribution particles in sizes. Note that the n_{eff} curves are highly affected by the k_{eff} dependences. In the weakly absorbing region (values of k_{eff} are small for $\lambda < 500$ nm) the refractive index n_{eff} remained constant ($1.2 < n_{eff} < 1.3$) for the various samples. In the absorbing region ($k_{eff} > 0.2$) the refractive index curves exhibited abnormal dispersion behaviors. We can conclude that spectral region between 600 and 1000 nm is highly sensitive to the extremely small changes in the effective optical constants for plasmonlike nanostructures.

Effective-medium calculations suggest that a high level of light absorption can be realized in thin artificial layers made of metal nanoparticles embedded in dielectric matrix. The size of the metal nanoparticles plays an important role in the observed effects. Larger nanoparticles have larger polarizabilities and provide higher absorption efficiencies. It is worth noting that suggested nanostructured films are relatively simple and cheap to fabricate over large areas. Below
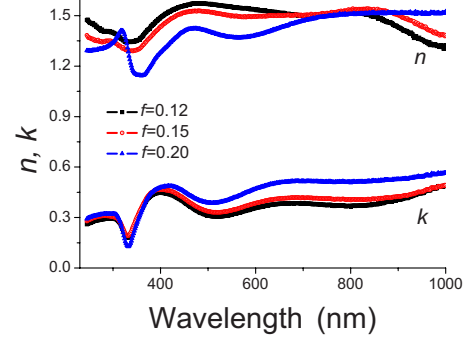

FIG. 7. (Color online) Experimental approbation of the effective-medium theory. The complex refractive index for the Ag-Al$_2$O$_3$ nanostructures as a function of wavelength extracted with ellipsometric measurements based on model of effective layer for different volume fraction of Ag: $f = 0.12, 0.15, 0.2$.

we compare our experimental results with these theoretical predictions.

V. DISCUSSION

Measured wavelength dependences of the $R_P(\lambda)$ and $T_P(\lambda)$ coefficients [Figs. 3(a) and 3(b)] are in good agreement with the theoretical data [Figs. 5(a) and 5(b)]. In particular, the position of the maxima ($\lambda \sim 350$ nm) in $R_P(\lambda)$ spectral dependences is nicely reproduced, and the reflection and transmission spectra show small variations with wavelengths and incident angles and keep the level at 2–5 %. Broad peaks in transmission occur at $\lambda \sim 320$ nm for all angles of incidence (Fig. 2). An absorption peak at $\lambda \sim 320$ nm can be assigned to the interband transitions of d electrons in silver particles modified by the presence of dielectric host {i.e., at the plasmon resonance condition Re$[\varepsilon(\text{Ag})] = -2\varepsilon_d(\text{Al}_2\text{O}_3)$}. The real part of the silver dielectric constant significantly increases at these wavelengths (Fig. 6).

In order to understand the role of silver nanoparticles in the enhancement of light absorption we have compared the experimental and theoretical effective dielectric functions. The effective complex index of refraction $n_{eff} + ik_{eff}$ was directly extracted from the measured ellipsometric parameters $\psi(\lambda)$ and $\Delta(\lambda)$. The result is shown in Fig. 7 as a function of filling factor, f. It is easy to see that k_{eff} increases with increasing filling factor f while the n_{eff} decreases in the region 400–800 nm. We notice that n_{eff} is ranged between 1.2 and 1.7 over the entire visible and near IR region, implying mostly dielectric response. The dependences of n_{eff} and k_{eff} display three broad peaks. The extinction peaks, k_{eff}, are blueshifted in comparison to those in the n_{eff} curves. Additionally, the effective refractive index $n_{eff} + ik_{eff}$ inverts the main tendency of the refractive index of noble metal, Ag. The values of the complex refractive index of Ag, which are typical for all noble metals, are next: smallness of the real part n (less than 1) and a large of the imaginary part $k \geq 1$ in visible and near-IR spectral regions. Obtained values n_{eff} and k_{eff} are in good agreement with values of $n_{eff}^{\perp} \approx 1.6$ and $k_{eff}^{\perp} \approx 0.3$ for the effective EMA constants obtained for gold

nanostripe structures in our recent work (Ref. 10) that described the plasmonic blackbody in the wavelength range 240–520 nm. There are some difference between extracted and calculated values of k_{eff} which arises due to the presence of trapped light modes. These modes effectively increase the path of light propagation in the metamaterial and therefore increase the sample thickness in the EMA approach. It is also worth noting that the effective optical constants extracted for Ag-Al$_2$O$_3$ structures in the wavelength range of "blackbody" behavior (400–850 nm), are close to the values of the effective constants which would guarantee the maximal absorption in accordance with the Fresnel coefficients shown in Figs. 5 and 6.

The experimental results (Fig. 7) are in a good agreement with the simulated functions of $n_{eff}+ik_{eff}$ (Fig. 6) for wavelengths 500–850 nm. A poorer agreement between experimental and modeled refractive index was obtained at longer and shorter wavelengths. We explain this by the presence of the guided light modes propagating along the film and arising due to total internal reflection [Fig. 1(d)]. The deviation of the theory and experiment at short wavelengths can be due to the interband transitions in silver nanoparticles. Introduced Drude-Lorentz approximation is not ideal for description of optical properties of silver nanoparticles. In bulk silver the interband transition from occupied *d* states to unoccupied *p* and *s* states above Fermi level appear at 4 eV (310 nm) and 3.5 eV (350 nm),[14] respectively. For silver nanostructures such electron transitions from *d* states to *p* and *s* states become allowed at frequencies below 3.5 eV (350 nm) and depend on nanostructure geometry. Additionally, the quantitative differences between experimental (Fig. 7) and theoretical (Fig. 6) data at short wavelengths could arise because of the presence of nonstoichiometric AgO$_x$ oxides and nonspherical Ag nanoparticles. We found that the Fresnel model with an additional roughness layer with voids (~3–5 nm thick) on top of Ag-Al$_2$O$_3$ film resulted in a better fit to experimental ellipsometric functions $\psi(\lambda)$ and $\Delta(\lambda)$. This agrees with the conclusion of Aspnes *et al.*[20] who stressed that noble film grown at slightly different conditions could have considerably different optical constants n_{eff} and k_{eff} above the interband transitions due to contribution of small defects such as voids.

It is worth noting that the spectral behavior of the calculated effective refractive index reflects the main features in $R_p(\lambda)$ and $T_p(\lambda)$. The occurrence of broad peaks in the $R_p(\lambda)$ and $R_s(\lambda)$ spectra (Figs. 3 and 4) is correlated with main features of effective refractive index $n_{eff}+ik_{eff}$ which describes the collective optical properties of the nanostructures. First, the energy position of broad peak at 300–500 nm in $R_p(\lambda)$, $R_s(\lambda)$, and $A_p(\lambda)$ spectra (Figs. 3 and 4) correlates with appearance of the maxima in n_{eff}. Second, the broad maxima in the region of 650–800 nm in the n_{eff} and k_{eff} spectra look like as the features in $R_p(\lambda)$ and $A_p(\lambda)$ dependences for large angles of incidence. These features in $R_p(\lambda)$ and $A_p(\lambda)$ are shifted toward the larger wavelengths in comparison to ones in the n_{eff} and k_{eff}. Physically, the origin of these broad maxima can come from excitation of localized plasmons in isolated silver particles. Due to the negative real part of the dielectric constant of silver, Re[$\varepsilon(\omega)$], incident light excites localized plasmon resonances, which shift in

near IR region (700–800 nm) for particles of large sizes ($D \geq 100$ nm).[21–23] These resonances can occur at discrete frequencies and are strongly localized in skin surface layer of large particles. Due to dipole-dipole interaction between ensemble of particles and strong coupling between localized plasmon these resonances tend to broadening and producing tight bound bands. Existence of such plasmon bands is a good condition for creating plasmonic structures with blackbody behaviors.[10] An important part of the interaction of light with plasmon-active nanostructures is the trapping and conversion of the incident radiation which can be used to enhance the efficiency of solar cells and photodetectors.[24,25] In this research it was also experimentally shown the strong correlation between macroscopic optical characteristics as a reflection and transmission and spectral dependencies of the effective optical constants. Due to this connection it is possible to determine the effective complex refractive index $n_{eff}+ik_{eff}$ *in situ* using ellipsometry and obtain desire values of absorption spectra. Such control of the optical properties can be very important during performance of large area of high-efficiency solar cells.

VI. CONCLUSIONS

We showed that the optical properties of Ag-Al$_2$O$_3$ nanostructures can be tuned by adjusting the size and concentration of silver nanoparticles in Al$_2$O$_3$ matrix and thickness of layer. The main properties of these systems are studied within the frame of the Mie theory of particle dipole polarizability and macroscopic behaviors described by the Maxwell-Garnett-type effective-medium theory. We demonstrated that for such structures the level of light absorption more than 95% can be achieved in a wavelength range of 240–850 nm for the large range of the incident angles $(0°–70°)$ and for the light with electric-field vector parallel to incident plane (*p*-polarized light). Absorption higher than 90% for both polarizations (*p*- and *s*-polarized or unpolarized light) in a range of angle of incidence equal to $(0°–45°)$ was revealed. It was shown that experimentally observed dependence of the absorption in nanostructure thin film can be explained on the basis of EMA theory with introduction of effective complex refractive index and using Fresnel reflection and transmission coefficients for thin film on top of glass substrate. We found that the effective optical constants $n_{eff}+ik_{eff}$ of silver nanostructures determined through spectroscopic ellipsometry are highly sensitive to changes in the particle sizes, particle covering, and thickness of layer. It is therefore important to monitor the refractive index of fabricated plasmonic metamaterial *in situ* with the aim to achieve desired absorption characteristics.

The proposed method for fabrication of thin-film blackbody inexpensive metamaterials (which strongly absorb light in broad spectral range as well as a wide interval of angles of incidence) could be applied to other metallic nanoparticles (Cu, Au, and Pd) that have a large reflectivity for bulklike states and for Si nanostructures or Si nanoparticles covered by Ag shell. The light incident on these structures can excite localized plasmon resonances, inducing polarization currents in the individual particles and transfer a significant portion of

energy into surface modes. Metal nanostructured thin-film metamaterials can find application for subwavelength energy accumulation in photodetectors, photoconverters, and a new generation of low-cost high-efficiency solar cells.

[1] F. Z. Yang, J. R. Sambles, and G. W. Bradberry, Phys. Rev. B **44**, 5855 (1991).

[2] K. R. Catchpole and A. Polman, Opt. Express **16**, 21793 (2008).

[3] H. R. Stuart and D. G. Hall, Appl. Phys. Lett. **73**, 3815 (1998).

[4] K. R. Catchpole and A. Polman, Appl. Phys. Lett. **93**, 191113 (2008).

[5] A. N. Grigorenko, A. K. Geim, H. F. Gleeson, Y. Zhang, A. A. Firsov, I. Y. Khrushchev, and J. Petrovic, Nature (London) **438**, 335 (2005).

[6] W.-C. Tan, J. R. Sambles, and T. W. Preist, Phys. Rev. B **61**, 13177 (2000).

[7] M. Kreiter, J. Oster, R. Sambles, S. Herminghaus, S. Mittler-Neher, and W. Knoll, Opt. Commun. **168**, 117 (1999).

[8] E. Popov, D. Maystre, R. C. McPhedran, M. Neviere, M. C. Hutley, and G. H. Derrick, Opt. Express **16**, 6146 (2008).

[9] E. Popov, S. Enoch, and N. Bonod, Opt. Express **17**, 6770 (2009).

[10] V. G. Kravets, F. Schedin, and A. N. Grigorenko, Phys. Rev. B **78**, 205405 (2008).

[11] J. C. Maxwell-Garnett, Philos. Trans. R. Soc. London, Ser. A **203**, 385 (1904).

[12] F. J. García-Vidal, J. M. Pitarke, and J. B. Pendry, Phys. Rev. Lett. **78**, 4289 (1997).

[13] R. M. A. Azzam and N. M. Bashara, *Ellipsometry and Polarized Light* (North-Holland Press, Amsterdam, 1987).

[14] E. D. Palik, *Handbook of Optical Constants of Solids* (Academic, San Diego, 1998).

[15] C. F. Bohren and D. R. Huffman, *Absorption and Scattering of Light by Small Particles* (Wiley, New York, 1983).

[16] E. Yablonovitch, J. Opt. Soc. Am. **72**, 899 (1982); E. Yablonovitch and G. D. Cody, IEEE Trans. Electron Devices **ED–29**, 300 (1982).

[17] W. T. Doyle, Phys. Rev. B **39**, 9852 (1989).

[18] V. A. Markel, J. Phys. B **38**, L115 (2005).

[19] R. Ruppin, Opt. Commun. **182**, 273 (2000).

[20] D. E. Aspnes, E. Kinsbron, and D. D. Bacon, Phys. Rev. B **21**, 3290 (1980).

[21] A. V. Zayats and I. I. Smolyaninov, J. Opt. A, Pure Appl. Opt. **5**, S16 (2003).

[22] F. J. García de Abajo, Rev. Mod. Phys. **79**, 1267 (2007).

[23] V. G. Kravets, F. Schedin, and A. N. Grigorenko, Phys. Rev. Lett. **101**, 087403 (2008).

[24] L. Eurenius, C. Hagglund, E. Olsson, B. Kasemo, and D. Chakarov, Nat. Photonics **2**, 360 (2008).

[25] H. R. Stuart and D. G. Hall, Phys. Rev. Lett. **80**, 5663 (1998).

From One Electron to One Hole: Quasiparticle Counting in Graphene Quantum Dots Determined by Electrochemical and Plasma Etching**

*Soeren Neubeck, Leonid A. Ponomarenko, Frank Freitag, A. J. M. Giesbers, Ulrich Zeitler, Sergey V. Morozov, Peter Blake, Andre K. Geim, and Kostya S. Novoselov**

Graphene – a monolayer of carbon atoms packed into a hexagonal lattice – is widely considered to be a promising material for future electronics.[1] Many unusual properties of this two-dimensional crystal originate from the linear, gapless spectrum of its quasiparticles.[1–4] At the same time, many electronics applications require the presence of an energy gap. To this end, considerable efforts have been applied to create nanostructured devices out of graphene sheets (such as nanoribbons,[5,6] quantum point contacts (QPC),[7] single electron transistors,[1,8] and quantum dots (QD)[7]), in which a gap can be opened due to quantum confinement of the charge carriers. In most cases the formation of such graphene nanostructures relies on the removal of unwanted areas of graphene by reactive plasma etching (usually in oxygen plasma).[5–9] The performance of such nanostructured devices is expected to depend strongly on the quality[9,10] and chemical nature of the sample edges.[10] Therefore, it is crucially

important to develop other methods of creating graphene nanostructures and control the edge orientation.

One of the possible alternatives for reactive plasma etching is local electrochemical etching. Initially demonstrated for the case of graphite,[11–13] local cutting by a biased conductive tip of an atomic force microscopy (AFM) system has been applied to graphene recently.[14] The technique is based on the dissociation of water molecules with subsequent chemical reaction of the radicals with the graphene carbon atoms. This opens up the possibility of local chemical modification of the graphene scaffolding, as well as for chemical modification of the edges. In this Communication, we describe the fabrication of graphene QPCs and QDs by the AFM etching technique and measurements of their properties. This technique has allowed us to produce graphene structures with a resolution and quality similar to those previously achieved by using high-resolution electron-beam lithography and subsequent plasma etching.[7] The operation of these devices is demonstrated by studying their behavior in a magnetic field.

We used a Veeco Multimode scanning probe microscope with a NanoScope IIIa controller, which was operated in contact mode for AFM measurements and oxidation. The samples were mounted on a custom-made sample holder to allow for in situ monitoring of their electronic properties. Topography scans revealed the height of our graphene samples (exfoliated from natural graphite[15]) to be typically about 0.8 nm above the SiO_2 surface, which is the standard value for monolayer graphene in AFM measurements.[16] An air-tight enclosure was used during our experiments on local oxidation, which allowed us to maintain a constant temperature ($22\,°C$) and humidity (70%). Conductive silicon tips were biased with respect to the graphene samples (the bias was controlled by a Keithley source meter) and scanned along chosen lines with a speed of around $200\,nm\,s^{-1}$ (higher speeds resulted in irregularly shaped etched structures or could even lead to the complete suppression of etching). We chose to work in the regime of "zero force" between the tip and the sample, which proved to produce the most reproducible results and thinnest cutting lines.

The direct current (DC) through the tip, as well as the resistance of the graphene devices (measured by the standard alternating-current lock-in technique), were monitored during the AFM oxidation. Typically, a tip bias of about $-7V$ was

[*] S. Neubeck, Dr. L. A. Ponomarenko, F. Freitag, Dr. K. S. Novoselov
School of Physics & Astronomy
University of Manchester
Manchester, M13 9PL (UK)
E-mail: kostya@manchester.ac.uk

A. J. M. Giesbers, Dr. U. Zeitler
High Field Magnet Laboratory
Institute for Molecules, Materials
Radboud University Nijmegen
Toernooiveld 7, 6525 ED Nijmegen (The Netherlands)

Dr. S. V. Morozov
Institute for Microelectronics Technology
Chernogolovka, 142432 (Russia)

Dr. P. Blake, Prof. A. K. Geim
Centre for Mesoscience and Nanotechnology
University of Manchester
Manchester, M13 9PL (UK)

required to initiate oxidation, which resulted in DC currents in the range of 10–100 nA. It should be noted that the threshold voltage was found to depend crucially on the humidity and biases in excess of −20 V were required when the humidity dropped below 60%.

Figure 1 shows an example of the QD structure etched by this technique (the parameters used here were: bias −7 V; humidity 70%; scanning speed 200 nm s^{-1}). Bright (dark) lines
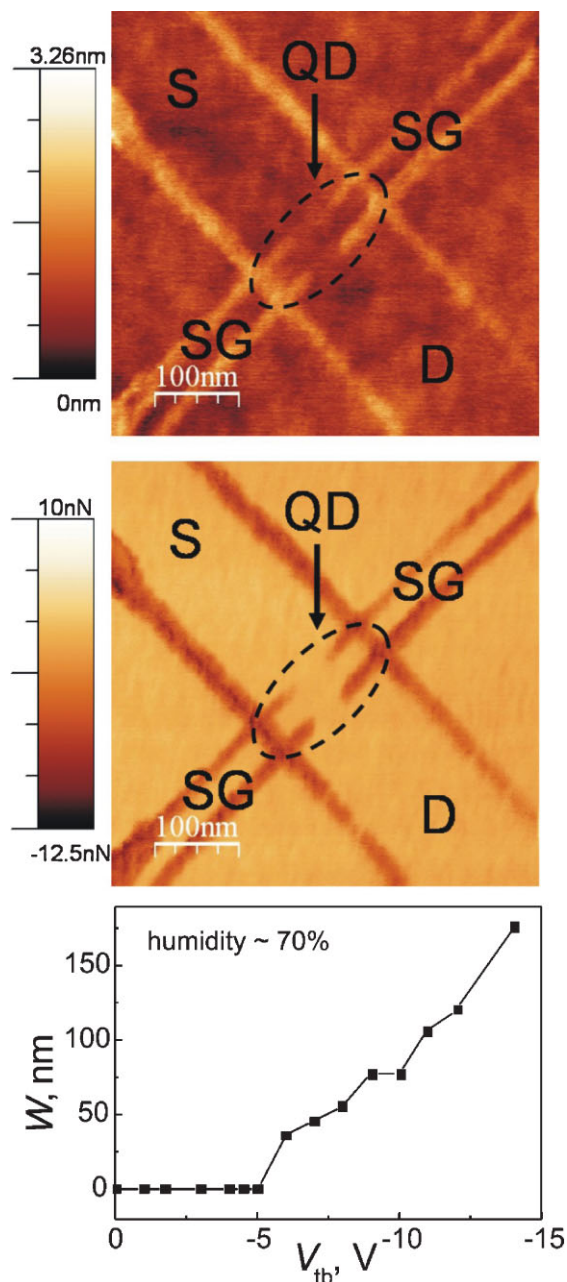

Figure 1. Top and middle: Example of a graphene QD structure created by local anodic oxidation. Top: Contact-AFM height image of a QD. Middle: The corresponding friction image. The bright regions in the friction image are intact graphene and the dark lines are the areas where graphene was etched away. The central island (marked as QD) is connected to the source (S) and drain (D) electrodes via narrow constrictions. Side gates (SG) are also formed from graphene. Bottom: The dependence of the width of the etched lines on the applied AFM-tip bias voltage.

on the top (middle) panel of Figure 1 are the nonconductive oxidized areas. Generally, applying a more negative bias to the tip for prolonged time (slower scanning) would result in complete etching away of graphene, rather than in oxidation. The central island of the QD (defined by the oxidized lines) is weakly connected by the narrow constrictions to the source and drain contacts. Using fresh tips and keeping the humidity relatively low, we managed to obtain oxidized lines with widths of down to 15 nm, which is comparable to the best QPC and QD graphene structures obtained with electron-beam lithography.[7] The widths of the lines increased with increasing humidity (although the range of humidity where the technique works reliably is rather narrow at 60–80%) or if the bias voltage was significantly above its threshold value. The dependence of the line width on the applied AFM-tip bias voltage is shown in the bottom panel of Figure 1. Above the threshold (which depends on the humidity) the width of the etched lines increases approximately linearly with more negative bias voltages. This is in line with general expectations coming from a simple model of a water meniscus built up around the tip apex.[14]

An example of the typical behavior of the conductivity through one of our QDs (similar to the one shown on Figure 1) at various temperatures is presented in Figure 2. The conductivity shows a strongly distorted V-shape[7] behavior and its value drops well below one conductivity quantum (e^2/h) in the voltage range between 33 and 41 V. In this range, several sharp conductivity peaks are observed. Outside this region, the conductivity grows above $0.5e^2/h$ (which we attribute to increased transparency of the constrictions (QPCs) between the QD and the source and drain contacts) and the QD levels could not be resolved. The nonmonotonic behavior of G in the region below 33 V and above 41 V is probably due to changes in the transmission through the QPCs.[8]
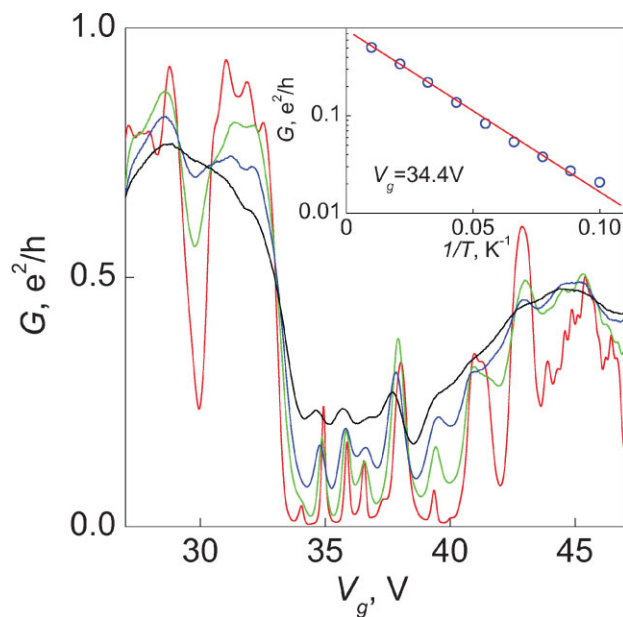

Figure 2. Conductivity through one of our QD devices (size ≈100 nm) as a function of backgate voltage for different temperatures. Red curve: 2.5 K; green curve: 10 K; blue curve: 20 K; black curve: 30 K. Inset: Temperature dependence of the conductivity at a minimum between peaks ($V_g = 34.4$ V).

The resonances in the voltage range between 33 and 41 V are associated with the energy levels in the QD. The peaks are strongly aperiodic, which suggests that both the Coulomb energy and the size-quantization energies contribute to the splitting between energy levels.[17] The number of peaks stays constant for temperatures below 20 K. Also, the relatively weak temperature dependence in the resonances (that can be as high as $\approx 0.5 e^2/h$) indicates that only one QD is present.[18] Peak height increases at the lowest temperatures, as expected for a Coulomb blockade in the quantum case.[18] The temperature dependence of the minimum conductivity (Figure 2, inset) corresponds to an energy gap of 6.5 meV, in agreement with the typical level spacing expected for a 100-nm QD ($\delta E = \alpha/D$, where α varies around a value of 1 eV nm^{-1} by a factor of 2 in different models[19,20]).

Similar values of the gap are obtained from the stability diagrams (conductivity versus gate voltage and source–drain bias), such as the one presented in Figure 3, which shows the standard Coulomb diamonds.[21] The height of the diamonds directly yields the distance between adjacent energy levels and, for this particular sample, varies from 5 to 10 mV. Such strong variation shows that the size quantization contributes significantly to the formation of energy levels in our small quantum dots.[17]

In the remaining part of this paper, we demonstrate that our QDs can be set into the state with no charge (zero electrons and zero holes present). This also means that QDs (prepared by either AFM or electron-beam lithography) can be tuned into a state with any chosen number of electrons or holes. It has been proven previously[7,22] that graphene quantum dots allow for the observation of both electronic and hole states, although no method for determining the exact crossover point has been demonstrated. In particular, the behavior of the energy levels in a magnetic field was used[22] in order to determine the approximate position of the electron/hole crossover in
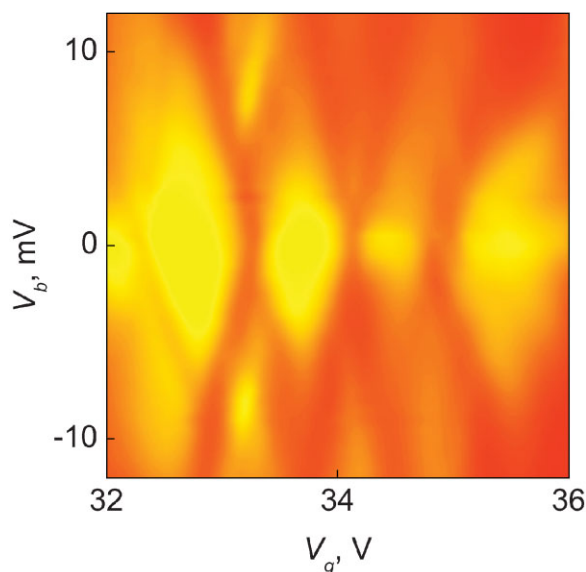
relatively large (80 nm) QDs. Here, we will show that the same method, when applied to smaller QDs, gains enough resolution and allows for exact pin pointing of the crossover state with zero quasiparticles in a QD. The ability to set up a quantum dot in a state with a predetermined number of only a few electrons or holes might be extremely important for the realization of a particular spin state and thus for the implementation of qubits.[23]

The stability diagram for one of our devices is presented in Figure 4. Measurements at elevated temperatures indicate that the compensation point for this QD lies between −1 and 4 V (for comparison, see Figure 2, in which the compensation point for that QD is expected between 34 and 39 V). Accordingly, in our detailed experiments, we concentrated on the compensation region and followed the behavior of the conductivity peaks in a perpendicular magnetic field. The magnetic field causes a shift in the peak's positions as a function of gate voltage. Such behavior is presented in Figure 4. Importantly, there is a certain symmetry in the behavior of some peaks. For example, peak H0 shifts symmetrically with respect to E0, as with H1 to E1, H2 to E2, and so on. Furthermore, the behavior of E0 and H0 is notably different from all the others, including those that are not presented in Figure 4 (in total, we measured the behavior of about 20 peaks). Both E0 and H0 show monotonic and the largest shifts, whereas all the other peaks demonstrate weak nonmonotonic behavior.

Such magnetic response is well known for conventional quantum dots based on semiconducting heterostructures and can be explained in terms of the energy levels shifting in the magnetic field.[23] Depending on the orbital quantum number, up or down shifts in the energy position can be observed. The lowest level with zero orbital number always exhibits diamagnetic behavior (i.e., its energy increases with increasing magnetic field).[24] The nonmonotonic behavior of higher energy levels is normally explained in terms of crossing between levels in a magnetic field and many-body effects.[24] Following the same analysis, we attribute peaks E0 and H0 to the lowest levels for electrons and holes, respectively. This implies that, in the range of gate voltages between 0.62 and 1.25 V, the quantum dot is not charged, and for 0.25–0.62 V (1.25–2.3 V), the QD contains one hole (electron). The other conductivity peaks correspond to two (H1, E1), three (H2, E2), electrons or holes in the dot, and so on. The oscillatory behavior of the peak positions can be attributed to level crossing in the magnetic field.

It has been predicted[25] that, for quasiparticles with a Dirac-like spectrum in graphene, the first energy level for electrons (holes) should shift down (up) towards zero energy and eventually form a zero Landau level in quantizing magnetic fields. However, this simple behavior is expected only in the absence of strong intervalley scattering, so that the Dirac cones are preserved, and in sufficiently high fields such that $l_b << R$ (where $l_b = (\hbar/eB)^{1/2}$ is the magnetic length and R the radius of a QD). The QDs presented in this work do not satisfy these criteria: the intervalley scattering is expected to be very efficient at the rough QD edges and the highest magnetic field we used ($B = 14$T) yields $l_b = 7$ nm, which is comparable with the QD's $R = 10$ nm. Lifting of the valley and spin degeneracies in graphene QDs and nanoribbons has also been experimentally

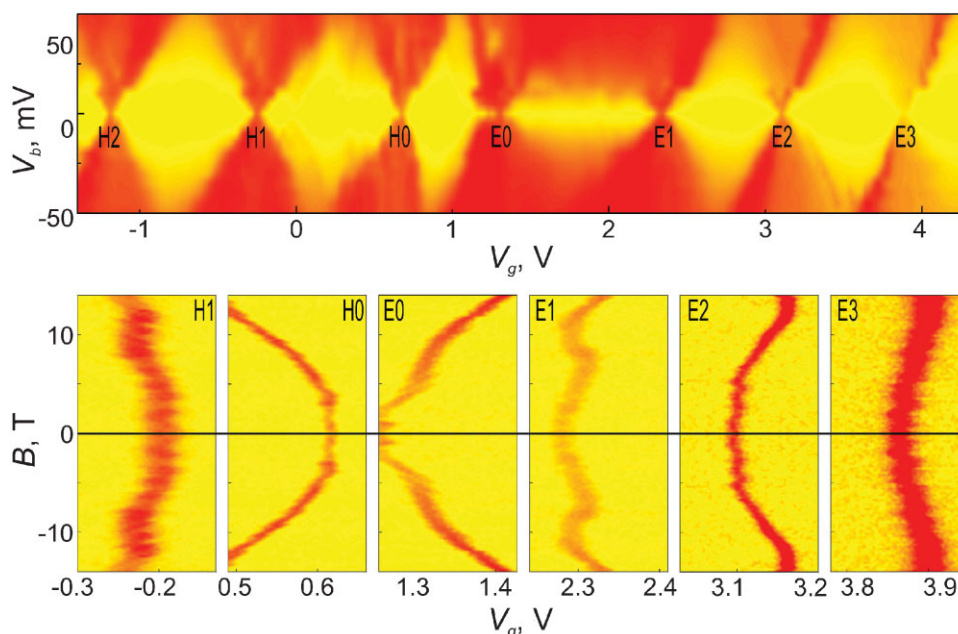**Figure 3.** Coulomb diamonds for the QD in Figure 2 as a function of the gate voltage (the horizontal axis) and the source–drain bias voltage (V_b, vertical axis). $T = 2.5$K. The conductivity varies from 0.002 e^2/h (yellow) up to 0.2 e^2/h (red).

Figure 4. Top: Coulomb diamonds in another QD ($\approx$20 nm in size). $T = 0.3$K; $B = 0$T. Bottom: Evolution of the resonant-peak positions in a magnetic field. $T = 0.3$K, $V_b = 0$V. The peaks are marked on the stability diagram in zero B (top panel). The conductivity varies from practically zero (yellow) up to $0.05e^2/h$ (red).

demonstrated in previous experiments.[7,26] Under these conditions, it is reasonable to expect that the spatial quantization and strong intervalley scattering make quasiparticles "forget" about their initial Dirac-like spectrum and follow the standard behavior for massive electrons and holes. The diamagnetic shift of the first energy levels would then be described by the theory[24] developed for semiconducting quantum dots. At the moment, there is no theory developed for graphene with dominant intervalley scattering in order to compare our results.

In conclusion, AFM lithography can be used to make graphene nanostructures with sizes below 15 nm. Furthermore, choosing the etching agent, one can control the functionalization of the edges of such structures. The resolution achieved by this technique is controlled by the humidity and the applied bias voltage. The behavior of our smallest quantum dots is strongly influenced by intervalley scattering at the sample edges, the regime that has not been discussed theoretically until recently.[27] Shifting of the peak position in a magnetic field allowed us to identify the empty state of the QD with no quasiparticles present and count the number of electrons and holes as the QD levels are filled in sequence. This is the first example of quantum dots in which a controllable ambipolar transition from a single hole, through an empty QD, to a state with a single electron has been achieved.

Experimental Section

Graphene crystallites were prepared from natural graphite[15] on an oxidized Si substrate (300 nm of SiO$_2$) by micromechanical cleavage.[1,2,16] Standard electron-beam lithography, thin-film deposition, and reactive plasma etching techniques were then used to produce graphene Hall bars with a typical width of 1 μm,

having Ti/Au contacts.[2,3] Our samples were annealed for 4 h at $T = 250\,^\circ$C in a hydrogen/argon atmosphere (10% hydrogen) to remove resist residues. Electrical measurements revealed an electron mobility of $\approx$13 000 cm^2 (V s)$^{-1}$ (measured at typical carrier concentrations of $n = 10^{12}$ cm^{-2}). The single-layer nature of the device used was confirmed by Raman spectroscopy and the observation of the half-integer quantum Hall effect that is a characteristic signature for graphene.[3,4]

[1] A. K. Geim, K. S. Novoselov, *Nat. Mater.* **2007**, *6*, 183.
[2] K. S. Novoselov, A. K. Geim, S. V. Morozov, D. Jiang, Y. Zhang, S. V. Dubonos, I. V. Grigorieva, A. A. Firsov, *Science* **2004**, *306*, 666.
[3] K. S. Novoselov, A. K. Geim, S. V. Morozov, D. Jiang, M. I. Katsnelson, I. V. Grigorieva, S. V. Dubonos, A. A. Firsov, *Nature* **2005**, *438*, 197.
[4] Y. Zhang, J. W. Tan, H. L. Stormer, P. Kim, *Nature* **2005**, *438*, 201.
[5] M. Y. Han, B. Ozyilmaz, Y. B. Zhang, P. Kim, *Phys. Rev. Lett.* **2007**, *98*, 206805.
[6] Z. H. Chen, Y. M. Lin, M. J. Rooks, P. Avouris, *Physica E* **2007**, *40*, 228.
[7] L. A. Ponomarenko, F. Schedin, M. I. Katsnelson, R. Yang, E. W. Hill, K. S. Novoselov, A. K. Geim, *Science* **2008**, *320*, 356.
[8] C. Stampfer, J. Guttinger, F. Molitor, D. Graf, T. Ihn, K. Ensslin, *Appl. Phys. Lett.* **2008**, *92*, 012102.
[9] B. Oezyilmaz, P. Jarillo-Herrero, D. Efetov, P. Kim, *Appl. Phys. Lett.* **2007**, *91*, 192107.
[10] X. L. Li, X. R. Wang, L. Zhang, S. W. Lee, H. J. Dai, *Science* **2008**, *319*, 1229.
[11] T. R. Albrecht, M. M. Dovek, M. D. Kirk, C. A. Lang, C. F. Quate, D. P. E. Smith, *Appl. Phys. Lett.* **1989**, *55*, 1727.

[12] R. L. McCarley, S. A. Hendricks, A. J. Bard, *J. Phys. Chem.* **1992**, *96*, 10089.

[13] L. Tapaszto, G. Dobrik, P. Lambin, L. P. Biro, *Nat. Nanotechnol.* **2008**, *3*, 397.

[14] A. J. M. Giesbers, U. Zeitler, S. Neubeck, F. Freitag, K. S. Novoselov, J. C. Maan, *Solid State Commun.* **2008**, *147*, 366.

[15] http://www.grafite.com/, last accessed June 2010.

[16] K. S. Novoselov, D. Jiang, F. Schedin, T. J. Booth, V. V. Khotkevich, S. V. Morozov, A. K. Geim, *Proc. Natl. Acad. Sci. USA* **2005**, *102*, 10451.

[17] L. P. Kouwenhoven, C. M. Marcus, P. L. McEuen, S. Tarucha, R. M. Westervelt, N. S. Wingreen, in *Mesoscopic Electron Transport* (Eds: L. L. Sohn, L. P. Kouwenhoven, G. Schön), Kluwer Academic Publishers, Dordrecht, The Netherlands **1997**, pp. 105–214.

[18] Y. Meir, N. S. Wingreen, P. A. Lee, *Phys. Rev. Lett.* **1991**, *66*, 3048.

[19] L. Yang, C. H. Park, Y. W. Son, M. L. Cohen, S. G. Louie, *Phys. Rev. Lett.* **2007**, *99*, 186801.

[20] N. M. R. Peres, A. H. Castro Neto, F. Guinea, *Phys. Rev. B* **2006**, *73*, 195411.

[21] L. P. Kouwenhoven, D. G. Austing, S. Tarucha, *Rep. Prog. Phys.* **2001**, *64*, 701.

[22] J. Guttinger, C. Stampfer, F. Libisch, T. Frey, J. Burgdoerfer, T. Ihn, K. Ensslin, *Phys. Rev. Lett.* **2009**, *103*, 046810.

[23] R. Hanson, L. P. Kouwenhoven, J. R. Petta, S. Tarucha, L. M. K. Vandersypen, *Rev. Mod. Phys.* **2007**, *79*, 1217.

[24] S. Tarucha, D. G. Austing, T. Honda, R. J. van der Hage, L. P. Kouwenhoven, *Phys. Rev. Lett.* **1996**, *77*, 3613.

[25] P. Recher, J. Nilsson, G. Burkard, B. Trauzettel, *Phys. Rev. B* **2009**, *79*, 085407.

[26] C. L. Tan, Z. B. Tan, K. Wang, L. Ma, F. Yang, F. M. Qu, J. Chen, C. L. Yang, L. Lu, *Observations of two-fold shell filling and Kondo effect in a graphene nano-ribbon quantum dot device*, 2009, http://arxiv.org/abs/0910.5777.

[27] A. L. C. Pereira, *New J. Phys.* **2009**, *11*, 095019.

Direct determination of the crystallographic orientation of graphene edges by atomic resolution imaging

S. Neubeck,[1] Y. M. You,[2] Z. H. Ni,[1,2] P. Blake,[3] Z. X. Shen,[2] A. K. Geim,[3] and K. S. Novoselov[1,a)]

[1]*School of Physics and Astronomy, University of Manchester, Manchester M13 9PL, United Kingdom*
[2]*Division of Physics and Applied Physics School of Physical and Mathematical Sciences, Nanyang Technological University, Singapore 637371*
[3]*Centre for Mesoscience and Nanotechnology, University of Manchester, Manchester M13 9PL, United Kingdom*

In this letter, we show how high-resolution scanning tunneling microscopy (STM) imaging can be used to reveal that certain edges of micromechanically exfoliated single layer graphene crystals on silicon oxide follow either zigzag or armchair orientation. Using the cleavage technique, graphene flakes are obtained that very often show terminating edges seemingly following the crystallographic directions of the underlying honeycomb lattice. Performing atomic resolution STM-imaging on such flakes, we were able to directly prove this assumption. Raman imaging carried out on the same flakes further validated our findings. © *2010 American Institute of Physics.*
[doi:10.1063/1.3467468]

Graphene, the monolayer of carbon atoms arranged into a hexagonal lattice, was first isolated in 2004 by using the micromechanical cleavage technique.[1,2] Although a number of other methods for graphene synthesis have been proposed since then (including the reduction in graphene oxide,[3] decomposition of silicon carbide,[4,5] epitaxial growth on nickel and other substrates,[6–9] or direct chemical exfoliation[10,11]) the micromechanical technique (also known as the "Scotch-tape method") is still the procedure of choice for many researchers. Furthermore, the uniqueness of this procedure is that it reveals the peculiar micromechanical properties of this material, which might be used in obtaining crystallographically oriented graphene samples.

The choice of crystallographic orientation of the graphene flakes might be of crucial importance for the electronic properties of resulting devices.[12–14] Two following problems generally arise: (i) how to determine the crystallographic orientation of a particular graphene crystallite and (ii) how to prepare a device which is oriented exactly along one of those directions. Whenever there are quite a few ways for determination of the orientation,[15–19] preparation of well oriented edges is a tantalizing task.[20]

It has been noted[21] that flakes obtained by the "Scotch-tape method" often exhibit straight edges with the angle between the adjacent ones being a multiple of 30°. An example of such a flake is shown in Fig. 1(a).

Considering the hexagonal symmetry of graphene crystals, it has been suggested that the breaking occurs along the principal crystallographic directions, yielding flakes terminated with either armchair or zigzag edges.[21,22] Previously, Raman measurements have been employed to verify this idea,[17,18] demonstrating a clear difference in the amplitude of the D peak for edges oriented along zigzag and armchair directions. However, Raman measurements require elaborative modeling to explain the finding.

In this letter, we will use high-resolution scanning tunneling microscopy (STM) to prove beyond doubt that edges of graphene crystals are predominantly oriented along crystallographic directions. The main advantage of high-resolution STM compared to the aforementioned techniques is its ability to provide direct real-space images of the graphene crystal lattice with atomic resolution. Additionally, there is no need for having suspended samples in order to carry out STM investigations. Thus, it ultimately enables one to directly determine the crystallographic orientation of a given graphene flake, and hence the orientation of the edges terminating that sample. We also compare the results of the STM study to the Raman measurements.

Single layer graphene flakes were obtained by micromechanical cleavage of natural graphite. Exfoliated graphite flakes were deposited on top of an oxidized silicon wafer (300 nm of SiO_2), and crystallites of single layer thickness were identified using optical microscopy.[23] For our studies, we used flakes with a significant percentage of edges forming angles which are integer multiples of 30°. Examples of such flakes are shown in Figs. 1(a) and 2(a). Upon selection
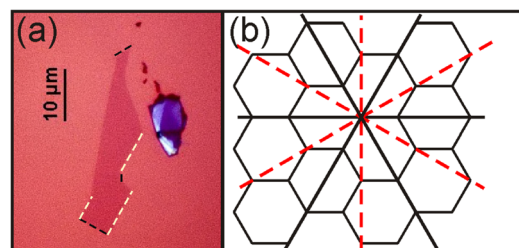

FIG. 1. (Color online) (a) Optical image of a single layer graphene flake prepared by micromechanical cleavage. It can be clearly seen that the edges terminating the graphene crystal follow straight lines up to lengths of several micrometers. Certain edges of this particular flake, oriented relative to each other in integer multiples of 30°, have been highlighted by a dashed line (black and white, for the respective type of edge). (b) Sketch of the honeycomb crystal lattice of graphene. Two distinct crystallographic orientations of a graphene crystal are possible: armchair (solid lines), and zigzag (dashed lines).

a)Author to whom correspondence should be addressed. Electronic mail: konstantin.novoselov@manchester.ac.uk.
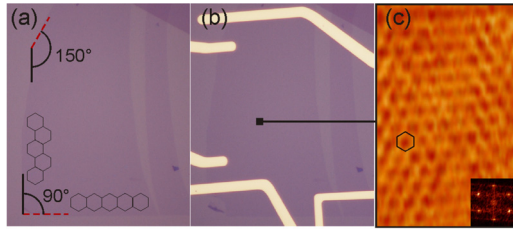
97, 053110-1

FIG. 2. (Color online) (a) Typical graphene flake obtained by microme-chanical cleavage. Two distinct types of edges, rotated against each other in multiples of 30°, are indicated as armchair type (solid lines) and zigzag type (dashed lines). (b) To carry out STM imaging, the flake in (a) was equipped with electrical contacts, and oriented carefully along the scanning direction of the STM-tip. (c) STM constant-height image [+0.223 V and (2.8 ± 0.3) nA], showing atomic resolution of the graphene hexagonal lattice. The inset on the lower right shows the Fourier transform of that image, where six well resolved diffraction spots are clearly visible. A single black hexagon is drawn as guide to the eye. Superimposing that hexagon onto the optical image proves the crystallographic orientation of the two indicated edge types.

of appropriate flakes, we used e-beam lithography to define electrical contacts on the flakes (Ti, 5 nm+Au, 40 nm) [Fig. 2(b)].

In order to find out whether the edges of, e.g., the graphene flake shown in Fig. 2(a) follow crystallographic orientations, we carried out high-resolution STM investigations. A Multimode scanning probe microscope with a Nanoscope IIIa controller was employed for conducting the STM experiments. All STM experiments were carried out under ambient conditions. Tunneling tips were made out of mechanically cut Pt_{80}/Ir_{20}-wire. The samples were precisely positioned in our STM, and the scanning direction was carefully aligned with one of the edges. Prior to imaging, the flakes were annealed at 250 °C in a hydrogen/argon-atmosphere,[24] in order to remove resist residuals due to the lithography treatment. After that, the flakes were found to be clean enough to achieve atomic resolution. Figure 2(c) shows an STM image of the graphene flake shown in Fig. 2(a), taken in constant-height mode at a sample bias of 223 mV and a set-point tunneling current of 2.8 nA (the tunneling current varied by a maximum of ±0.3 nA between positions on the atoms and interatomic positions). The atomically resolved hexagonal graphene lattice can be clearly seen, which is a clear proof of the monolayer character of this particular sample.[25] The Fourier transform of that image, shown in the inset on the lower right of Fig. 2(c), accordingly shows six well-resolved diffraction peaks. Both the atomically resolved image of the lattice and the Fourier transform image allow us to determine the orientation of the edges of a given graphene flake. This is done by virtually tiling the entire graphene flake under question with the experimentally observed hexagonal unit cell (or equivalently the corresponding Fourier transform). Following this approach for the flake shown in Fig. 2(a), we can identify the vertical edge as being armchair and the horizontal edge as being zigzag.

Additional information about the edges can be obtained from the Raman measurements. Recent results show that it is possible to distinguish between armchair and zigzag orientation by Raman spectroscopy.[17] The disorder-induced Raman feature of graphene (D peak at ~1350 cm⁻¹) is activated through a double resonance process[26] and is often observed at the edges. This is because the edges act as defects, allow-
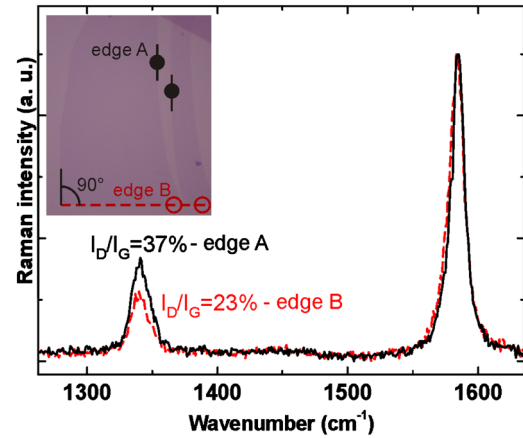

FIG. 3. (Color online) Raman spectra taken from two different edges (optical image shown in the inset on the upper left), labeled edge A (vertical solid line, solid spots) and edge B (horizontal dashed line, open spots), forming an angle of 90°. As graphene has a hexagonal crystal lattice, the two edges are believed to have different chirality. During the measurement, the laser polarization (linear) is oriented parallel to the graphene edge being measured, to maximize the D peak signal (Refs. 17 and 27). The Raman spectra at edge A (solid curve) shows a D-peak intensity of ~37% compared to the G-peak intensity, while it is only ~23% for the spectra taken at edge B (dashed curve). Raman spectra from different spots of the two edges gave similar results. This confirms our finding that edge A is armchair, whereas edge B is zigzag.

ing elastic backscattering of electrons to fulfill the double resonance condition.[27] The D peak was reported to be stronger at the armchair edge and weaker at the zigzag edge, due to the momentum conservation (armchair edges can scatter electrons between two nonequivalent Dirac cones, while zigzag edges cannot).[17,27] Raman measurements were carried out using a WITec CRM200 confocal microscopy Raman system with a 100× objective lens (numerical aperture =0.95). The excitation laser wavelength is 532 nm. We measured Raman spectra from points A and B, which are two edges forming an angle of 90°, as labeled in the inset (optical image) of Fig. 3.

During the measurement, the laser polarization (linear) is oriented parallel to the graphene edge under investigation, in order to maximize the D peak signal.[17,27] To determine the exact position of the graphene edge, Raman spectra were taken at different positions while scanning the laser spot perpendicularly across the particular edge under question (with a step size of 50 nm). The maximum intensity of the D-band measured under these conditions was taken in order to compare the two different edges. As shown in Fig. 3, at point A, the D peak intensity is ~37% of that of the G peak, while it is only ~23% at point B. This suggests that the edge containing point A is armchair while the other edge is zigzag. Raman spectra from different points of the two edges were checked and similar results were obtained. The Raman results confirm the STM results of the graphene crystallographic orientation. Here, we have to clarify that the edges mentioned above are predominantly crystallographic, as perfect zigzag and armchair edges are extremely rare. There are small amounts of armchair sections even on zigzag edges, both on exfoliated single layer graphene[13,28,29] and terraces on bulk graphite,[30] which contribute to the observed D peak at point B.

In conclusion, we have demonstrated the direct determination of the crystallographic orientation of graphene edges

by using high-resolution STM. The obtained atomic resolution images of the graphene crystal lattice have allowed us to unambiguously identify both armchair and zigzag edges of a given graphene flake prepared by mechanical exfoliation. Complementary information has been obtained by Raman spectroscopy, fully justifying our assumption that certain edges on micromechanically exfoliated samples predominantly follow crystallographic orientations of the underlying graphene crystal lattice.

[1] K. S. Novoselov, A. K. Geim, S. V. Morozov, D. Jiang, Y. Zhang, S. V. Dubonos, I. V. Grigorieva, and A. A. Firsov, Science **306**, 666 (2004).

[2] K. S. Novoselov, D. Jiang, F. Schedin, T. J. Booth, V. V. Khotkevich, S. V. Morozov, and A. K. Geim, Proc. Natl. Acad. Sci. U.S.A. **102**, 10451 (2005).

[3] S. Stankovich, D. A. Dikin, G. H. B. Dommett, K. M. Kohlhaas, E. J. Zimney, E. A. Stach, R. D. Piner, S. T. Nguyen, and R. S. Ruoff, Nature (London) **442**, 282 (2006).

[4] A. J. Van Bommel, J. E. Crombeen, and A. van Tooren, Surf. Sci. **48**, 463 (1975).

[5] C. Berger, Z. Song, T. Li, X. Li, A. Y. Ogbazghi, R. Feng, Z. Dai, A. N. Marchenkov, E. H. Conrad, P. N. First, and W. A. de Heer, J. Phys. Chem. B **108**, 19912 (2004).

[6] C. Oshima and A. Nagashima, J. Phys.: Condens. Matter **9**, 1 (1997).

[7] A. Reina, X. Jia, J. Ho, D. Nezich, H. Son, V. Bulovic, M. S. Dresselhaus, and J. Kong, Nano Lett. **9**, 30 (2009).

[8] K. S. Kim, Y. Zhao, H. Jang, S. Y. Lee, J. M. Kim, K. S. Kim J.-H. Ahn, P. Kim, J.-Y. Choi, and B. H. Hong, Nature (London) **457**, 706 (2009).

[9] X. Li, W. Cai, J. An, S. Kim, J. Nah, D. Yang, R. Piner, A. Velamakanni, I. Jung, E. Tutuc, S. K. Banerjee, L. Colombo, and R. S. Ruoff, Science **324**, 1312 (2009).

[10] P. Blake, P. D. Brimicombe, R. R. Nair, T. J. Booth, D. Jiang, F. Schedin, L. A. Ponomarenko, S. V. Morozov, H. F. Gleeson, E. W. Hill, A. K. Geim, and K. S. Novoselov, Nano Lett. **8**, 1704 (2008).

[11] Y. Hernandez, V. Nicolosi, M. A. Lotya, F. M. Blighe, Z. Sun, S. Dei, I. T. McGovern, B. Holland, M. Byrne, Y. K. Gun'ko, J. J. Boland, P. Niraj, G. Duesberg, S. Krishnamurthy, R. Goodhue, J. Hutchison, V. Scardaci, A. C. Ferrari, and J. N. Coleman, Nat. Nanotechnol. **3**, 563 (2008).

[12] N. M. R. Peres, A. H. Castro Neto, and F. Guinea, Phys. Rev. B **73**, 195411 (2006).

[13] L. Yang, C. H. Park, Y. W. Son, M. L. Cohen, and S. G. Louie, Phys. Rev. Lett. **99**, 186801 (2007).

[14] Y.-W. Son, M. L. Cohen, and S. G. Louie, Nature (London) **444**, 347 (2006).

[15] K. A. Ritter and J. W. Lyding, Nature Mater. **8**, 235 (2009).

[16] Ç. Ö. Girit, J. C. Meyer, R. Erni, M. D. Rossell, C. Kisielowski, L. Yang, C.-H. Park, M. F. Crommie, M. L. Cohen, S. G. Louie, and A. Zettl, Science **323**, 1705 (2009).

[17] Y. M. You, Z. H. Ni, T. Yu, and Z. X. Shen, Appl. Phys. Lett. **93**, 163112 (2008).

[18] C. Casiraghi, A. Hartschuh, H. Quian, S. Piscanec, C. Georgi, A. Fasoli, K. S. Novoselov, D. M. Basko, and A. C. Ferrari, Nano Lett. **9**, 1433 (2009).

[19] T. M. G. Mohiuddin, A. Lombardo, R. R. Nair, A. Bonetti, G. Savini, R. Jalil, N. Bonini, D. M. Basko, C. Galiotis, N. Marzari, K. S. Novoselov, A. K. Geim, and A. C. Ferrari, Phys. Rev. B **79**, 205433 (2009).

[20] X. Jia, M. Hofmann, V. Meunier, B. G. Sumpter, J. Campos-Delgado, J. M. Romo-Herrera, H. Son, Y.-P. Hsieh, A. Reina, J. Kong, M. Terrones, and M. S. Dresselhaus, Science **323**, 1701 (2009).

[21] A. K. Geim and K. S. Novoselov, Nature Mater. **6**, 183 (2007).

[22] D. Sen, K. S. Novoselov, P. Reis, and M. J. Buehler, Small **6**, 1108 (2010).

[23] P. Blake, E. W. Hill, A. H. Castro Neto, K. S. Novoselov, D. Jiang, R. Yang, T. J. Booth, and A. K. Geim, Appl. Phys. Lett. **91**, 063124 (2007).

[24] M. Ishigami, J. H. Chen, W. G. Cullen, M. S. Fuhrer, and E. D. Williams, Nano Lett. **7**, 1643 (2007).

[25] E. Stolyarova, K. T. Rim, S. Ryu, J. Maultzsch, P. Kim, L. E. Brus, T. F. Heinz, M. S. Hybertsen, and G. W. Flynn, Proc. Natl. Acad. Sci. U.S.A. **104**, 9209 (2007).

[26] C. Thomsen and S. Reich, Phys. Rev. Lett. **85**, 5214 (2000).

[27] L. G. Cançado, M. A. Pimenta, B. R. A. Neves, M. S. S. Dantas, and A. Jorio, Phys. Rev. Lett. **93**, 247401 (2004).

[28] Z. Liu, K. Suenaga, P. J. F. Harris, and S. Ijima, Phys. Rev. Lett. **102**, 015501 (2009).

[29] Q. Yu, J. Lian, S. Siriponglert, H. Li, Y. P. Chen, and S.-S. Pei, Appl. Phys. Lett. **93**, 113103 (2008).

[30] Y. Niimi, T. Matsui, H. Kambara, K. Tagami, M. Tsukuda, and H. Fukuyama, Phys. Rev. B **73**, 085421 (2006).

Scanning probe lithography on graphene

Soeren Neubeck, Frank Freitag, Rui Yang, and Kostya S. Novoselov*

School of Physics and Astronomy, University of Manchester, Manchester M13 9PL, UK

* Corresponding author: e-mail kostya@manchester.ac.uk, Phone: +44 161 275 4119, Fax: +44 161 275 4056

In this paper, we want to outline the principles of how scanning probe lithography on graphene is performed. We will show several examples of structures etched in graphene using this technique, including an example of a nanoelectronic device. In the last part, we present data regarding the oxidation kinetics when performing scanning probe lithography on graphite (HOPG).
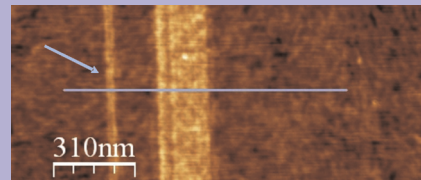
Two lines oxidized in graphene using scanning probe lithography. The left line (indicated by the arrow) is only 30 nm wide, indicating that this technique has good enough resolution to create nanoelectronic device structures.

1 Introduction Graphene, since its first experimental observation in 2004 [1], attracted great attention due to the intriguing electronic properties. Extremely high mobilities and charge carriers behaving as massless Dirac fermions open bright prospects both in the field of future integrated device electronics, as well as in the field of more fundamental studies aiming at exploring the properties of Dirac fermions in solid-state structures [2]. Confining the macroscopically sized graphene flakes down to nanometre sizes [3–6] combines these properties with quantum phenomena arising from confinement. To carve nanostructures out of graphene, most commonly electron beam lithography with subsequent etching in reactive ion plasmas is carried out [3–7].

A promising alternative is given by AFM-based local anodic oxidation (LAO), also referred to as scanning probe lithography, since it offers resist-free structuring and thus avoids contaminating the graphene flake with resist residues. First being applied to silicon [8] and metal surfaces [9], scanning probe lithography was also used to manipulate the surface of graphite (HOPG) [10] and to create nanoelectronic devices by patterning two-dimensional electron gases [11, 12]. In Ref. [13], it was first shown how this technique can be applied to perform nanolithography on graphene. Subsequently, first examples of graphene-based nanoelectronic devices created by scanning probe lithography were given [14–16].

2 Setup for scanning probe lithography Our scanning probe lithography experiments were carried out using a Digital Instruments MultiMode scanning probe microscope with a Nanoscope IIIa controller, equipped with Nanosensors PPP-CONTR highly doped contact mode silicon cantilevers. The entire scanning probe microscope was operated inside air-tight enclosure, allowing for control of the relative humidity between tip and sample. The electrical connections used for LAO on graphene are sketched in Fig. 1.

In order to apply a voltage to the AFM tip, a Keithley 2410 sourcemeter is connected via the Nanoscope Signal Access Module to the SPM. The graphene samples (see an optical image in the right part of Fig. 1) are mounted on custom-made sample holders to contact them electrically via a breakout box. For *in situ* resistance measurements, a SR830 lock-in amplifier is connected to the breakout-box in either a 2-probe or a 4-probe setup. Before performing scanning probe lithography in the setup explained, the graphene samples were annealed in a hydrogen/argon atmosphere at 250 °C for about 2 h.

Original

Paper

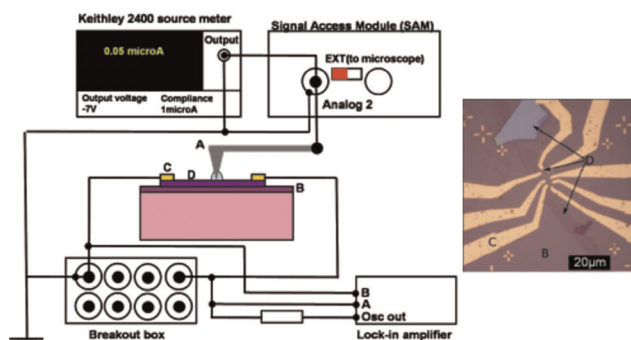Phys. Status Solidi B **247**, Nos. 11–12 (2010)

2905

Figure 1 (online colour at: www.pss-b.com) Left: Electrical setup for scanning probe lithography. The tip voltage is applied through a Signal Access Module using a sourcemeter. The oxidation current flowing between tip (A) and the grounded graphene flake (D), is limited to 1 μA in order to avoid accidental damage to the flake. The resistance of the graphene flake can be monitored *in situ* through a breakout-box by connecting a lock-in amplifier to the sample contacts (C). Right: Optical image of a graphene device used for scanning probe lithography. Several thinner and thicker graphene flakes are placed on top of an oxidized silicon wafer (B) (oxide thickness typically 300 nm). The flakes are connected through Ti/Au contacts, allowing the flakes to be set to ground with respect to the AFM tip.

3 Fabrication of nanometre-sized structures on graphene Operating the AFM in contact mode, we achieved successful LAO when a tip voltage of −7 V was applied at a relative humidity of 70% and the probe was scanned along the preferred directions with a probe velocity ranging from 200 nm/s up to 1 μm/s. Higher scanning speeds led to irregular line shapes or even complete suppression of oxidation. The spring force acting on the tip was set close to zero. This condition was found to yield the most reliable oxidation while achieving the thinnest line widths. Under these conditions, an oxidation current flowing between the AFM tip and the grounded graphene flake of 10–100 nA could be measured at the sourcemeter.

For a relative humidity of 70%, we found that for the given probe velocity, the line widths increased approximately linearly with applying a more negative potential to the AFM tip. For tip voltages less negative than −5 V, no oxidation was observed at all. Typically, tip voltages of −7 V were found to yield the best results in terms of reliability and achieving narrow line widths. With the relative humidity being lower than 60%, more negative tip voltages, often in excess of −20 V, were needed to start oxidation. On the other hand, for a relative humidity higher than 80%, no oxidation was found to occur. In this case, the oxidation current flowing between tip and sample reached the set current limit of 1 μA. An example of a narrow line oxidized in graphene by using scanning probe lithography is shown in Fig. 2.

On the left, several lines can be seen, which were oxidized by applying a voltage of −7 V to the silicon tip with respect to the grounded graphene flake in an atmosphere with the relative humidity between 65 and 80% and a probe
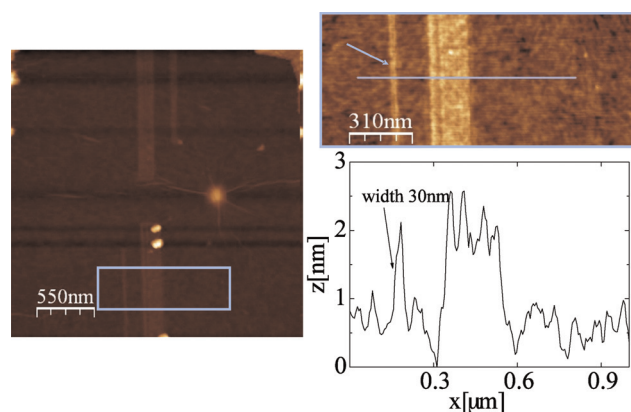

Figure 2 (online colour at: www.pss-b.com) Left: Several lines oxidized in graphene (tip bias −7 V, relative humidity 65–80%, tip velocity 1 μm/s). Note that all lines appear as protrusions. Right: In the upper part, a magnified image of the region on the left indicated by the box is displayed, showing two straight lines oxidized in graphene. The bottom part shows an AFM line profile taken perpendicular to the oxidized lines (solid horizontal line in the upper image), indicating that the thinnest line (left) only has a width of 30 nm.

velocity of 1 μm/s. The upper image on the right shows a magnified view of two of the lines, as indicated by the box on the left. The thinnest line (left) is only 30 nm wide, as shown by the line profile (corresponding to the solid horizontal line in the upper image) below this image. It is worth mentioning that this particular line appears as a protrusion. In general, we have found that the oxidized areas, when imaged in contact mode AFM, sometimes appeared as protrusions and sometimes as depressions, depending on the scan direction. This observation can be related to the influence of frictional forces on the contact AFM imaging process. Hence the question whether we created a stable graphitic oxide, or whether we etched away the graphene completely cannot be answered from contact AFM images alone. However, performing LAO under identical conditions (same humidity, bias voltage, tip velocity and exposure time) results in a similar height (within experimental error) of the measured protrusions or depressions found for the respective oxidation conditions.

To further investigate this question, we have imaged lines oxidized in graphene (oxidation conditions: tip bias −7 to −9 V, relative humidity 60–80% and tip velocities 200 nm/s to 1.2 μm/s) by both contact mode AFM and Tapping mode AFM. The results are shown in Fig. 3.

While in contact AFM imaging (top panel, image on the left, indicated line profile on the right) all four lines, labelled A–D, appear as protrusions, in Tapping Mode AFM imaging the broadest line (A) appears as depression containing some debris, while the lines labelled B–D still appear as protrusions. The different behaviour for line A is due to the different oxidation conditions, under which this line was oxidized. Whereas the lines B–D are only 80 nm wide (equal to a single scan of the AFM tip), for line A an area of about 450 nm (equal to multiple scans) was oxidized. Apparently, the time for which the area corresponding to line A was
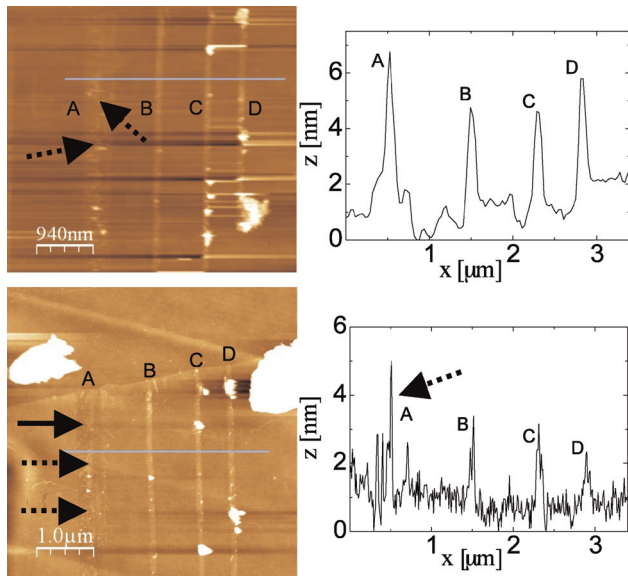
Figure 3 (online colour at: www.pss-b.com) Top: On the left, a contact mode AFM image showing four different lines (labelled A–D) oxidized on graphene is displayed. The dashed arrows indicate inhomogeneous areas on line A, but which are not well resolved in contact mode AFM. The corresponding line profile (solid horizontal line in the image) on the right indicates all of the lines as being protrusions. Bottom: Tapping mode AFM image of the same four oxidized lines as shown in the top panel. The improved lateral resolution allows distinguishing areas for line A where graphene was etched away (solid arrow) and where residual pieces of oxidized graphene remained (dashed arrows). In the corresponding line profile on the right, the broadest line (A) appears as depression, but still shows spikes originating from residual oxidized graphene (dashed arrow). All other three lines (B–D) appear as protrusions.

exposed to the AFM tip voltage is much greater than that for lines B–D. The result of mostly etching away graphene (indicated by the solid arrow) for area A is in line with our observations that prolonged exposure to the tip voltage leads to the eventual removal of graphene. The debris in area A, which appears as protrusions, is formed from residual pieces of oxidized graphene (dashed arrows). Scanning area A in contact mode gives rise to the appearance of a protrusion, because of these residual oxidized graphene pieces. The lateral resolution in contact mode AFM is affected by lateral forces, and hence this area appears as protrusion. In Tapping Mode AFM, the lateral resolution is less affected by lateral forces, and so both the areas where graphene was etched away and the single residual oxidized graphene pieces are better resolved. In the corresponding line profile, the latter appear as spikes (dashed arrow), whereas the etched areas appear as depression.

Although these results clearly confirm the chemical alteration of graphene by LAO, they still do not allow for a clear assignment of the chemical composition of the oxidized areas.

Having established the working parameters for AFM-based lithography of graphene, we focus on oxidizing

nanometre-sized structures that could operate as nanoelectronic devices. An example of a quantum point contact with adjacent sidegate oxidized in graphene is given in Fig. 4.

The left part of the image shows a contact mode AFM overview image of the structure, fabricated with a tip bias of −7 V, relative humidity of 60–70% and probe velocities between 0.2 and 0.7 μm/s. In the top part of that image, a V-shaped line oxidized in graphene can be seen. This line is a cut in graphene and serves to electrically insulate a contact from the remaining part of the flake. The region separated by the oxidized line, which can be used as a sidegate, is indicated by 'SG'. Next to the sidegate, a narrow graphene constriction (60 nm × 60 nm in size) was fabricated that forms a graphene quantum point contact. A black arrow points to this constriction, which is also shown in larger magnification in the centre of the top image on the right part of Fig. 4. The line profile in the lower right part of Fig. 4 was taken perpendicular to the etched diagonal line, and clearly shows the stepheight of single layer graphene as measured by AFM, i.e. a stepheight of around 0.8 nm.

4 Oxidation kinetics on HOPG An interesting point to note is the fact that applying scanning probe lithography to graphene resulted in either etching lines (depressions as in
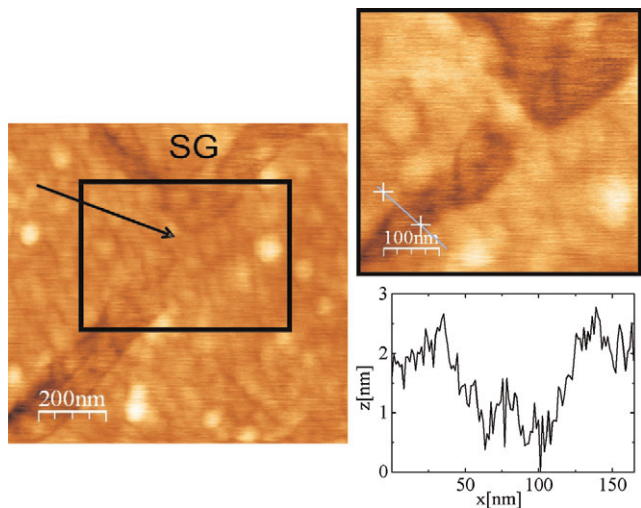

Figure 4 (online colour at: www.pss-b.com) Left: Contact mode AFM image showing a quantum point contact (black arrow) with adjacent sidegate (top part, labelled 'SG') formed in single layer graphene by scanning probe lithography. The sidegate consists of a contact that has been electrically isolated from the remaining graphene flake by etching a V-shaped line around it. Oxidation was carried out at −7 V tip bias, a relative humidity of 60–70% and probe velocities ranging from 0.2 to 0.7 μm/s. Right: On top, a magnified image of the quantum point contact, marked in the left image with a black box, is shown. The quantum point contact is a region of intact graphene with a size of about 60 nm × 60 nm. On the bottom, an AFM line profile perpendicular to the etched line that forms the quantum point contact is displayed, indicating a stepheight of the cut of around 0.8–1 nm, the stepheight of single layer graphene. This is an example of an area oxidized on graphene appearing as a depression, i.e. indicating that graphene got etched away completely.

Original
Paper

Phys. Status Solidi B **247**, Nos. 11–12 (2010)   2907

Fig. 4) or in creating a stable oxide (protrusions as in Fig. 2). To learn more about the oxide properties, we carried out LAO experiments on the surface of bulk graphite (HOPG). By measuring the height of the oxide grown as a function of the time the oxidation voltage was applied, we were able to determine the oxidation kinetics for LAO on graphite. We then compare these results to the kinetics reported for silicon, as silicon is one of the most extensively studied substrates for LAO [17, 18]. We have chosen HOPG because its surface shows the same chemical behaviour as single layer graphene. Furthermore, using HOPG as a substrate, we can obtain more general results describing the oxidation behaviour of sp²-hybridized carbon by taking the fact into account that HOPG is a three-dimensional material, thus not limiting the oxide growth to two dimensions. An important point here is that when measuring the height of the dots oxidized with scanning probe lithography, the dots appeared either as protrusion or as depression, depending on the scan direction chosen for contact mode AFM imaging. This phenomenon was already observed for other materials [19, 20] and it was attributed to the AFM tip experiencing areas of different friction when scanned over areas that differ from the surrounding in crystal structure or chemical composition. Grafstroem et al. [21] further claimed that the height of these different areas when measured in contact mode AFM might be affected by the frictional forces.

If the oxidation kinetics bears similarities between HOPG and silicon, it gives evidence that the observed protrusions on graphene and HOPG are indeed a stable oxide. For silicon oxide, a linear dependence of the oxide height on the applied voltage was observed. Hence, we oxidized dots with different tip voltages and exposure times (time, for which the voltage was applied to the AFM tip) of 5 and 10 s, respectively, at a relative humidity of 55–70%. Our data obtained on HOPG is shown in Fig. 5.

We found that the dot's height increases linearly with the applied voltage, as shown in Fig. 5. The same behaviour (linear increase in dot height as a function of applied voltage) was reported for LAO on silicon [18]. The increase in oxide height with applied voltage on HOPG gives values of −0.7 nm/V (5 s exposure, dots) and −0.4 nm/V (10 s exposure, squares). The faster growth of the dots with shorter exposure time is caused by using two different tips, oxidizing at different humidities and probably also by friction. While our curves and the one reported for silicon [18] differ in absolute values, they are qualitatively in agreement, thus indicating the growth of an oxide.

To further investigate the kinetics of HOPG oxidation, we measured the oxide height for different exposure times. In Fig. 6, the oxide height on HOPG as a function of the exposure time is shown.

Our experimental data points were fitted with a model suggested by Dagata et al. [17]. This model is based on the observation that oxide formation via LAO is a self-limited process, i.e. the height of oxide grown depends on the logarithm of the time during which the oxidation voltage is applied. In his treatment, Dagata extends this model,
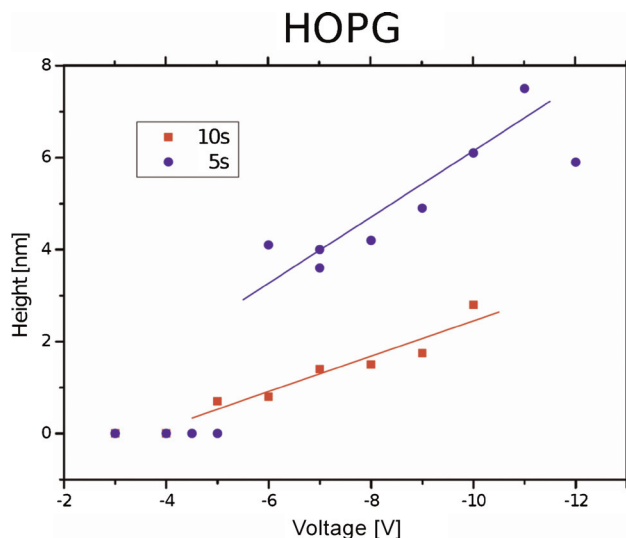
Figure 5 (online colour at: www.pss-b.com) Height of dots oxidized on the surface of HOPG using two different exposure times (5 s, dots; 10 s, squares) at a fixed tip position as a function of applied AFM tip voltage. The height of the dots increases linearly with the applied tip voltage becoming more negative. The difference in heights for the two exposure times is probably due to slightly different oxidation conditions (humidity, friction and tip geometry).

assuming a dual-reaction pathway for the build-up of oxide. Two competing processes are considered responsible for oxide formation, eventually leading to the self-limited growth behaviour of the oxide. The first process is direct oxidation (A → C), with rate constant k_1, describing the
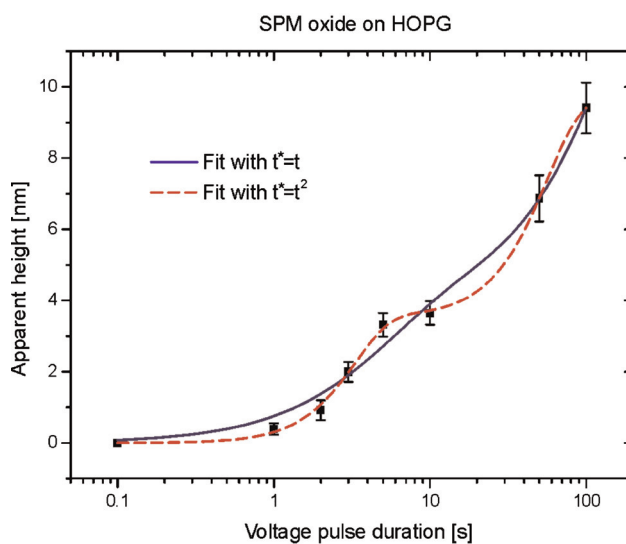
Figure 6 (online colour at: www.pss-b.com) Height of dots oxidized on HOPG as a function of the time the voltage (−7 V, applied at a relative humidity between 50 and 70%) was applied to the AFM tip (logarithmic scale). The solid curve corresponds to a fit to a model describing oxide growth proposed by Dagata et al. [17]. For the dashed curve, the exposure time has been replaced with its value squared.

direct formation of oxide (C) from oxyanions (A). The second, competing process, which eventually interferes with growth of oxide, is an indirect reaction. It is described as $(A \rightarrow B \rightarrow C)$. First, an intermediate product (B) is formed from the oxyanions (A), described by the rate constant k_2. In a second step $(B \rightarrow C)$, this intermediate product reacts to form oxide, described by the rate constant k_3.

We find that the dual-reaction pathway kinetics of this model gives accurate results, with the same ordering of the rates, $k_2 > k_1 > k_3$, as observed for Si/SiO_2 by Dagata. This ordering of the rate constants says that initially the direct $(A \rightarrow C)$ oxidation occurs. But over time space charge $(A \rightarrow B \rightarrow C)$ builds up, which interferes with growth and hence leads to the observed self-limited behaviour. In particular, our fit (solid curve in Fig. 6) to the expression given in [17] yields $k_1 = 0.03993$, $k_2 = 0.164$ and $k_3 = 0.0041$. However, the fit can be even further improved by replacing the exposure time t with $t = t^2$. For this case (dashed curve in Fig. 6), the rate constants obtained are $k_1 = 0.0331$, $k_2 = 0.0571$ and $k_3 = 0.00031$. A possible explanation is that the friction signal dominates the measured height, as suggested by Grafstroem et al. [21], and hence the apparent height is much bigger than the actual oxide height. But again, the curves reported for silicon in [17] show a similar qualitative behaviour. It might be worth noting that in fitting our experimental data using a time exponent of 0.4, as discussed in [17], we obtain a negative rate constant, which is in contradiction to the underlying model.

To sum up, we can observe similar kinetics for LAO on HOPG as were reported for LAO on silicon. This leads to the conclusion that we selectively create a stable oxide on HOPG. However, we are currently not able to assign definitive chemical reactions for the processes involved. The electrochemical oxidation of HOPG with respect to the formation of a stable oxide is yet not well understood [22]. For LAO on graphene, the results obtained on HOPG indicate that the oxidized areas consist of a graphitic oxide. But since graphene is only one atom thick, the possibility of a complete etch cannot be ruled out strictly.

5 Conclusions In conclusion, we have shown how to create graphene nanostructures using AFM-based LAO. It was shown that this approach yields a resolution better than 30 nm and is capable of producing structures that could be used as nanoelectronic devices. The chemical nature of the structures fabricated by this scanning probe lithography technique is still not well established. Experiments carried out on bulk graphite (HOPG) indicate the formation of a stable graphitic oxide, but further proof is needed.

References

[1] K. S. Novoselov, A. K. Geim, S. V. Morozov, D. Jiang, Y. Zhang, S. V. Dubonos, I. V. Grigorieva, and A. A. Firsov, Science **306**, 666 (2004).

[2] A. K. Geim and K. S. Novoselov, Nature Mater. **6**, 183 (2007).

[3] M. Y. Han, B. Ozyilmaz, Y. B. Zhang, and P. Kim, Phys. Rev. Lett. **98**, 206805 (2007).

[4] Z. H. Chen, Y. M. Lin, M. J. Rooks, and P. Avouris, Physica E **40**, 228 (2007).

[5] L. A. Ponomarenko, F. Schedin, M. I. Katsnelson, R. Yang, E. W. Hill, K. S. Novoselov, and A. K. Geim, Science **320**, 356 (2008).

[6] C. Stampfer, J. Guttinger, F. Molitor, D. Graf, T. Ihn, and K. Ensslin, Appl. Phys. Lett. **92**, 012102 (2008).

[7] B. Oezyilmaz, P. Jarillo-Herrero, D. Efetov, and P. Kim, Appl. Phys. Lett. **91**, 192107 (2007).

[8] E. S. Snow and P. M. Campbell, Appl. Phys. Lett. **64**, 1932 (1994).

[9] E. S. Snow, D. Park, and P. M. Campbell, Appl. Phys. Lett. **69**, 269 (1996).

[10] T. R. Albrecht, M. M. Dovek, M. D. Kirk, C. A. Lang, C. F. Quate, and D. P. E. Smith, Appl. Phys. Lett. **55**, 1727 (1989).

[11] M. Ishii and K. Matsumoto, Jpn. J. Appl. Phys. **34**, 1329 (1995).

[12] R. Held, T. Vancura, T. Heinzel, K. Ensslin, M. Holland, and W. Wegscheider, Appl. Phys. Lett. **73**, 262 (1998).

[13] A. J. M. Giesbers, U. Zeitler, S. Neubeck, F. Freitag, K. S. Novoselov, and J. C. Maan, Solid State Commun. **147**, 366 (2008).

[14] S. Masubuchi, M. Ono, K. Yoshida, K. Hirakawa, and T. Machida, Appl. Phys. Lett. **94**, 082107 (2009).

[15] L. Weng, L. Zhang, Y. P. Chen, and L. P. Rokhinson, Appl. Phys. Lett. **93**, 093107 (2008).

[16] S. Neubeck, L. A. Ponomarenko, F. Freitag, A. J. M. Giesbers, U. Zeitler, S. V. Morozov, P. Blake, A. K. Geim, and K. S. Novoselov, Small **6**, 1469 (2010).

[17] J. A. Dagata, F. Perez-Murano, G. Abadal, K. Morimoto, T. Inoue, J. Itoh, and H. Yokoyama, Appl. Phys. Lett. **76**, 2710 (2000).

[18] D. Stievenard, P. A. Fontaine, and E. Dubois, Appl. Phys. Lett. **70**, 3272 (1997).

[19] J. P. Singh, R. Singh, N. C. Mishra, V. Ganesan, and D. Kanjilal, Nucl. Instrum. Methods Phys. Res. B **179**, 37 (2001).

[20] S. Bouffard, J. Cousty, Y. Pennec, and F. Thibaudau, Radiat. Eff. Defect Solids **126**, 225 (1993).

[21] S. Grafstroem, J. Ackermann, T. Hagen, R. Neumann, and O. Probst, J. Vac. Sci. Technol. B **12**, 1559 (1994).

[22] H.-S. Choo, T. Kinumoto, S.-K. Jeong, Y. Iriyama, T. Abe, and Z. Ogumi, J. Electrochem. Soc. **154**, B1017 (2007).